Analysis and interpretation of Carbon ion fragmentation in the Bragg peak energy range.

Scuola Dottorale in Scienze Matematiche e Fisiche

Dottorato di Ricerca in Fisica – XXVII Ciclo

Candidate

Carlo Mancini Terracciano

ID number 15538/311

Director

Prof. Roberto Raimondi

Thesis Advisor

Prof. Filippo Ceradini

Co-Advisor

Prof. Alfredo Ferrari

A thesis submitted in partial fulfillment of the requirements
for the degree of Doctor of Philosophy in Physics

October 2014

Thesis not yet defended

Analysis and interpretation of Carbon ion fragmentation in the Bragg peak energy range.

Ph.D. thesis. Università degli Studi Roma Tre

Version: January 8, 2015

Author's email: carlo.mancini-terracciano@cern.ch

This work has been funded within the
ENTERVISION Initial Training Network
by the European Commission,
FP7 Grant Agreement N. 264552.

Abstract

Hadrontherapy is the treatment of tumours with Protons (p), or heavier ions like Carbon (C) and Oxygen (O). It is based on the fact that ionising radiation is used to kill tumour cells. One of the advantages of heavy ions compared to conventional radiotherapy is the characteristic behaviour of the energy deposition, which peaks only when the particles are very close to the stopping point, called Bragg peak. The Hadrontherapy is becoming one of the main therapies for the treatment of some malignant neoplasms. Compared to Proton therapy, C therapy has considerable advantages, even though C ions could fragment.

In this work the exclusive quasi-elastic fragmentation reaction $^{12}\mathrm{C} + x \rightarrow ^{8}\mathrm{Be} + \alpha$ is studied at the energy of $33\,\mathrm{MeV\,u^{-1}}$ of projectiles, which is the dominant reaction at this energy. The importance of this energy domain relies on the fact that it is the typical value where the fast rise of the energy deposition starts, just before the Bragg peak.

Different target materials, namely Carbon, Gold and Niobium, have been used in the present work. In all the cases a contamination of H in the targets has been found. This contamination observed explains the excess of high energy α in the data. The reaction responsible for such an excess, $^{12}\mathrm{C} + \mathrm{p} \rightarrow ^{9}\mathrm{B} + \alpha$, has been added to the FLUKA Monte Carlo simulation (MC) code as a pre-equilibrium stage channel of the (p,α) reaction.

The identification and the description of the pre-equilibrium reaction in the MC allowed a significant improvement in the comparison between data and MC. This allowed to identify and reduce the background due to the H contamination in the process under investigation and measure its cross section as a function of the fragments' energy and emission angles.

Contents

Introduction

This work presents the data analysis of an experiment carried out in the iThemba laboratories (Cape Town, South Africa). The experiment is intended to measure the exclusive fragmentation reaction of ^{12}C (Carbon) into ^{8}Be (Beryllium) and ^{4}He (Helium), with an energy of 33 MeV u^{-1}. This work includes the achievement of the Monte Carlo simulation of the experiment and the implementation, in the Monte Carlo code itself, of the relevant processes that were missing.

33 MeV u^{-1} is an energy region of particular interest because it is in the range of values of ^{12}C beams used in hadrontherapy when they get close to the Bragg peak, where there is the maximum energy deposition in the tissue and close to the maximum of biological effect. In this energy range, the fragmentation reaction addressed is not only one of the possible channels, but it is the most important case.

FLUKA is already very effective in calculating the dose deposition, also in proximity and after the Bragg peak. However, especially close to an organ at risk, it is important to predict the dose delivered and its lateral spread as accurately as possible. Furthermore, in particular in the case of Carbon ions therapy, the emitted secondary simulation is required to correctly perform not only physical but also biological based dose calculations, since they are also a function of the quality of the radiation. For these reasons, this experiment represents an important benchmark for FLUKA, a fully integrated particle transport and interaction MC code, already widely used in particle therapy. The data presented in this work are of utmost importance because they investigate selectively the quasi-elastic breakup of ^{12}C in ^{8}Be and α particles using the correlation between two sets of detectors.

The experiment ran with targets in different materials, namely Carbon, Niobium, Gold and Polyethylene. One of the two detectors has been placed at different angles for each target, to study the angular distribution of the reaction under investigation.

The analysis of the data revealed a surprising double peak structure and an excess of α fragments faster than the beam. This last feature was detected in previous correlation experiments with Oxygen beams, as reported in the review of H. Fuchs and K. Moehring [FM94].

We started from the supposition of a Hydrogen contamination in the target. This hypothesis has led to investigate the Carbon ions interaction with Hydrogen through the experimental run with a Polyethylene target. Thanks to such run, the production of ^{9}B (Boron) ground state as intermediate state has been identified as being responsible for the double peak structure and for the excess in the high energy α particles.

The direct reaction between ^{12}C and proton that produces ^{9}B has been implemented in FLUKA and the selection criteria has been modified to benchmark

the new channel with the data. Using the Monte Carlo simulation, the amount of contamination has been evaluated in the Carbon, Niobium and Gold targets and the Hydrogen contribution has been identified in each of them. Finally, the selection criterion for the quasi elastic break-up of the ^{12}C has been modified to reduce the impact of the H contamination and the cross section of the process under investigation, namely the quasi-elastic fragmentation reaction $^{12}\mathrm{C} + x \rightarrow^{8} \mathrm{Be} + \alpha$, has been measured as a function of the of the fragments' energy and emission angles.

Albeit I did not personally participated in the data taking, done in 2009, my contribution included realising the analysis starting from the raw data, importing them in ROOT and recalibrating also one of the detectors. Furthermore, I developed a full MC simulation of the experiment with the FLUKA MC framework permitting an event by event analysis, finally I contributed in the implementation of better reaction models in FLUKA itself.

Chapter 1

Project context

1.1 Cancer treatment with ion beams

The term *radiation therapy* indicates the medical use of ionising radiation which has become widely used in the treatment of cancer. Usually, conventional radiotherapy refers to the use of high energy photons and electrons, while hadrontherapy is used for the treatment of tumours with Protons, but also with heavier ions like Carbon or Oxygen.

The idea of using Protons for cancer treatment was first proposed in 1946 by the physicist Robert Wilson [Wil46], while he was investigating the depth-dose characteristics of Proton beams, primarily for shielding purposes. He recognised the potential benefits of Proton beams and predicted that "precision exposures of well-defined small volumes within the body will soon be feasible."

The first patients were treated in the 1950s in nuclear physics research facilities by means of non-dedicated accelerators. Initially, the clinical applications were limited to few parts of the body, as accelerators were not powerful enough to allow Protons to penetrate deep in the tissues. In the late 1970s, improvements in accelerator technology, coupled with progresses in medical imaging and computing, made Proton therapy a viable option for routine medical applications. However, it is only since the beginning of the 1990s that Proton facilities have been established in clinical settings, the first one being in Loma Linda, USA.

Nowadays, Protons are used in 45 facilities [Ptc]; besides Protons the use of Carbon ions is more and more wide spread. In fact, as we will see in detail in the next section, it is believed to have some advantages such as a sharper energy deposition, a smaller lateral spread and a higher biological effectiveness. These features provide a good local control of very aggressive tumours and a lower acute or late toxicity, thus could enhance the quality of life during and after cancer treatment. Since the birth of hadrontherapy, more than 60 000 patients have been treated globally with hadrons, including 5 500 with Carbon ions [Ptc], see Figure 1.1.

In Europe, the interest in hadrontherapy is growing and the first dual ion (Carbon and Protons) clinical facility in Germany, the Heidelberg Ion Beam Therapy Center (HIT), started treating patients at the end of 2009. A second one, the Centro Nazionale di Adroterapia Oncologica (CNAO) of Pavia started with Protons in September 2011 and with Carbon ions in November 2012 [Cna]. Another facility,

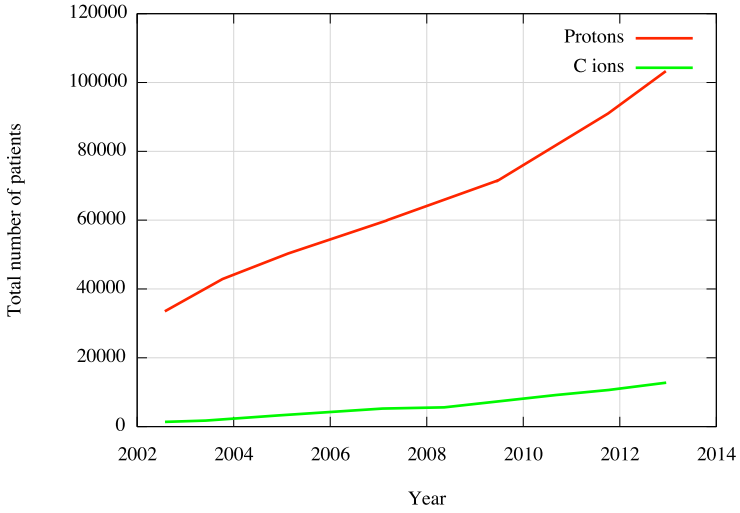

Figure 1.1. *Patients treated with Protons and Carbon ions worldwide. Data from [Ptc; Jer14].*

the Particle Therapy Center (PTC) of Marburg will be operating soon while other facilities, such as MedAustron in Wiener Neustadt, are in the commissioning phase.

1.2 Physical and Biological Aspects of Radiotherapy

The aim of a radiotherapy treatment is to deliver a planned dose to the tumour, while sparing the healthy tissue surrounding it. The dose deposition of photons and electrons is maximum at the entrance and decreases with depth, as can be seen in Figure 1.2. Therefore, to maximise the dose to the tumour and spread the unwanted entrance dose, the strategy used in conventional radiation therapy is to use crossing beams from many angles. On the contrary, the dose profile of ions peaks at the end of their range. Indeed the strength of hadrontherapy lies in the unique physical and radiobiological properties of these particles: they can penetrate the tissues with little diffusion and deposit most of the dose just before stopping. This could allow a precise definition of the specific region to be irradiated. The peaked shape of the hadron energy deposition is called Bragg peak, named after Sir William Henri Bragg who investigated the slowing down of α particles in air [BK05]. A comparison of depth-dose profiles for photons, electrons and ions is shown in Figure 1.2. The dose deposited by photons initially builds up, mainly because of electrons scattered via Compton effect. In contrast to photons, the dose profiles of Protons and heavier ions are characterised by the Bragg peak, as already mentioned, at the end of their path. The position of this peak can be precisely adjusted to the desired depth in tissue by changing the kinetic energy of the incident ions. The dose tail behind the Carbon ions Bragg peak is caused by secondary fragments produced in nuclear reactions along the path. As will be discussed in section 1.3

The damage caused by ionising radiation can be due to either direct or indirect ionisation of the atoms constituting the Deoxyribonucleic acid (DNA) chain. Indirect

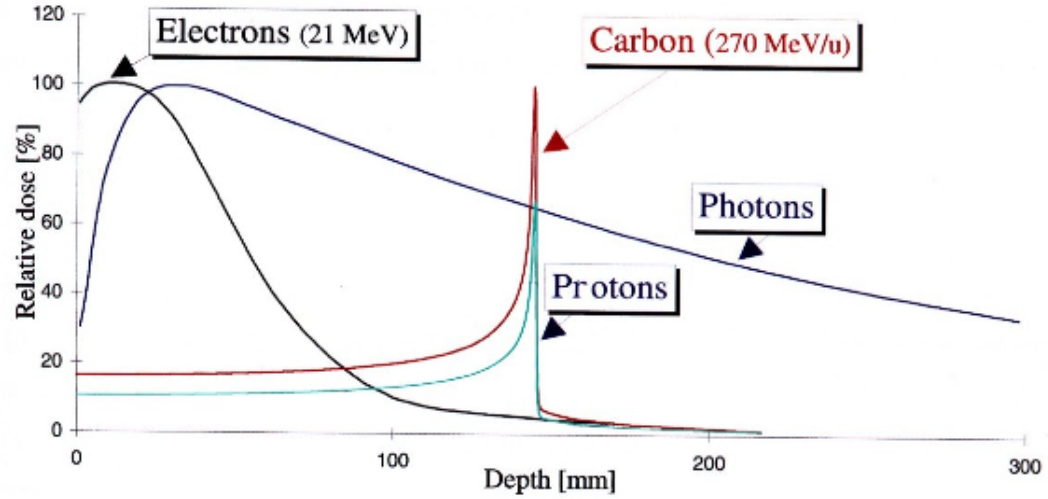

Figure 1.2. *The energy deposition of different particles in matter. For ions the Bragg peak appears clearly.*

damage happens as a result of the ionisation of water forming free radicals, notably hydroxyl radicals, which then damage the DNA.

One of the most important physical quantities in radiotherapy is the "absorbed dose", defined as the mean energy dE deposited by ionising radiation in a mass element dm:

$$D = \frac{dE}{dm}\,. \tag{1.1}$$

The absorbed dose is measured in Gray (Gy). 1 Gy is equivalent to $1\,\mathrm{J\,kg^{-1}}$.

It is believed that, in conventional radiotherapy, the damage is mainly caused by free radicals [BPS08].Oxygen is a potent radiosensitizer, increasing the effectiveness of a given dose by forming DNA-damaging free radicals [GCEHS53]. However, solid tumours can outgrow their blood supply, causing a low-oxygen state known as hypoxia. Tumour cells in a hypoxic environment may be as much as 2 to 3 times more resistant to radiation damage than those in a normal oxygen environment [Har02].

While Protons cause biological damage in a way similar to photons and electrons, heavier charged particles, such as Carbon ions, can cause direct damage to a cancer cell DNA through high Linear Energy Transfer (LET) [Kra00], equivalent to the energy loss dE/dx. Moreover, Carbon ions usually cause multiple-stranded DNA breaks [Kie08] that are much more difficult to repair for the cell, so the effectiveness of the dose is increased with respect to sparsely ionising radiation, furthermore it is independently of oxygen supply. To compare the effectiveness of different ionising particles, the Relative Biological Effectiveness (RBE) has been defined. It is the ratio between the dose absorbed from the γ decay of ^{60}Co needed to produce the wanted outcome and the dose of the radiation under study [IAEA], needed to produce the same consequence:

$$RBE = \left(\frac{D_{(\gamma\,^{60}\mathrm{Co})}}{D_{(\mathrm{test})}}\right)_{\mathrm{isoeffect}}\,. \tag{1.2}$$

RBE is a combination of a physical effect, namely the ionisation density, and of a biological phenomenon, that is the DNA repair capacity of the cell.

Radiotherapy of deep-seated tumours requires ion beam ranges in tissue of up to 30 cm, meaning energies up to 430 MeV u^{-1} for a therapy with Carbon ions. At these energies the energy loss rate is well described by the Bethe formula [Bet30; Fan63; Ahl80; PDG]:

$$\frac{dE}{dx} = -K\frac{Z_t}{A}\frac{Z_p^2}{\beta^2}\left[L_0(\beta) + Z_p L_1(\beta) + Z_p^2 L_2(\beta)\right] \tag{1.3}$$

where K includes all the constants:

$$K = 4\pi N_A r_e^2 m_e c^2 = 0.307\,075\,\text{MeV}\,\text{mol}^{-1}\,\text{cm}^2, \tag{1.4}$$

r_e is the classical electron radius:

$$r_e = e^2/4\pi\epsilon_0 m_e c^2 = 2.817\,940\,326\,7(27)\,\text{fm}, \tag{1.5}$$

Z_t and A are respectively the atomic number and atomic weight of the target and N_A is the Avogadro's number.

$L_0(\beta)$ is the Bethe term:

$$L_0(\beta) = \frac{1}{2}\ln\left(\frac{2m_e c^2\beta^2\gamma^2 W_{max}}{\langle I\rangle^2}\right) - \beta^2 - \frac{\delta(\beta\gamma)}{2} - \frac{C}{Z_t} \tag{1.6}$$

where W_{max} is the maximum energy transfer to an electron in a single collision for a particle with mass M and charge Z_p:

$$W_{max} = \frac{2m_e c^2\beta^2\gamma^2}{1 + 2\gamma m_e/M + (m_e/M)^2}, \tag{1.7}$$

$\delta(\beta\gamma)$ is a correction due to the density effect that limits the logarithmic rise for relativistic speed of the projectile, $\langle I\rangle$ is the mean excitation energy, and $\frac{C}{Z_t}$ is the shell correction.

The Equation 1.3 is based on the first order Born approximation. When the projectile velocity decreases or the charge of the projectile is large, there is a deviation from this prediction, and the next order of the perturbation theory gives corrections of higher orders in Z_p: $L_1(\beta)$ and $L_2(\beta)$. $L_2(\beta)$ is the Bloch correction [Blo33]. $L_1(\beta)$ takes into account the different stopping behaviours of positively and negatively charged particles discovered by Lassen in 1951 [Las51b; Las51a]. It is known as Barkas-Andersen effect and it is interpreted as being due to polarisation of the target material. More details about the Bloch and Barkas-Andersen corrections can be found in [Icr].

In the low energy region, it is also necessary to substitute the charge of the projectile (Z_p) with an effective charge ($Z_{eff.}$):

$$Z_{eff.} = Z_p\left(1 - e^{125\beta Z_p^{-\frac{2}{3}}}\right) \tag{1.8}$$

to take into account the decrease of the projectile charge due to the recombination with the target electrons.

As seen in Equation 1.3, the LET depends on the squared charge of the projectile. Therefore the higher is the charge, the higher is the density of energy transferred to target electrons. This is one of the reasons of the higher RBE of Carbon ions compared to photons, electrons and even Protons. Another advantage of Carbon ions is that, because of their large mass, they have a little lateral scattering in the tissue which ensures that the beam does not broaden much and focuses on the tumour shape, delivering small dose side-effects to surrounding tissue.

1.3 Nuclear fragmentation

The stopping process of high-energy ions (between tens to hundreds of MeV) penetrating a thick medium is governed by electromagnetic interactions with electrons and nuclei. The probability of a nuclear interaction is much smaller, despite of that nuclear interactions lead to significant effects, causing the projectile to fragment into lighter ions. Fragmentation has many important consequences in hadrontherapy:

- it can cause a loss of primary beam particles,
- it can build up lighter, less charged fragments which are moving at about the same speed as the primary ions and have generally longer ranges. The longer range is due to dependence to the square of the charge of the particle (Z_p^2) in the Equation 1.3, and produce a dose tail behind the Bragg peak (Figure 1.3).
- Secondary fragments could also produce a broadening of the lateral distribution of the deposited dose.

The fragmentation is so important that, for instance, in a $400\,\mathrm{MeV\,u^{-1}}$ C ions beam on water 70% of the primary particles do not reach the Bragg peak, undergoing nuclear reactions [Hae06]. The importance of the nuclear reactions grows up with the depth in the medium.

At energies of several hundred $\mathrm{MeV\,u^{-1}}$, nuclear spallation reactions may result in complete disintegration of both projectile and target nuclei, or in partial fragmentations. For geometrical reasons, peripheral collisions, where the beam particle loses one or several nucleons, are the most frequent nuclear reactions. They can be described by the model proposed by R. Serber [Ser47] for the stripping of Proton from a deuterium projectile. The Serber approach describes nuclei abrasion in the overlapping zone between projectile and target, while outer nucleons, usually called "spectator", are only slightly affected. The remaining projectile and target fragments could de-excite by evaporation of nucleons or clusters of nucleons. A more detailed description of the models used to describe nuclear interaction in the energy range of interest for hadrontherapy will be given in section 1.5.

The breakup of ^{12}C and ^{16}O has been studied in many experiments from the 1960's (for example Britt and Quinton [BQ60] and Sikkeland et al. [SHV62]). These studies, along with other ones conducted with projectiles in the low mass regime ($6 \lessapprox A \lessapprox 20$) at incident energies of $\approx 10\,\mathrm{MeV\,u^{-1}}$, showed the production of a large number of α fragments. Most of them are emitted forward, with a broad peak at an energy corresponding roughly to the beam velocity [BQ61]. Further experiments (such as [SWVPSW79]) indicated that most of these α's originate from

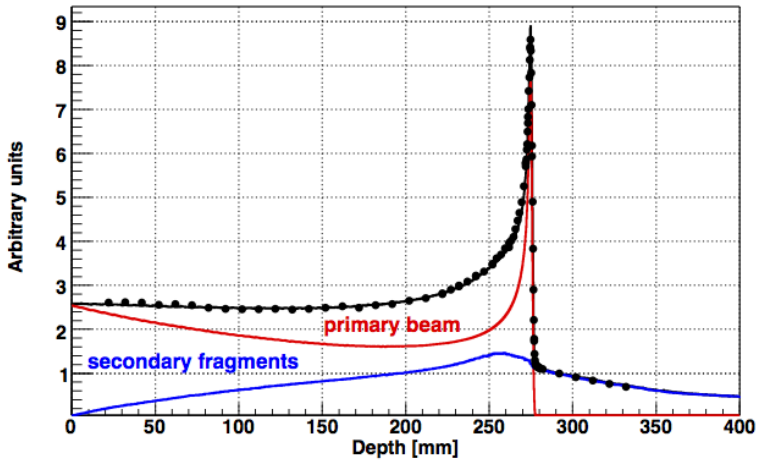

Figure 1.3. *Energy deposition of* 400 MeV *in water. The points are data, from [HIS06]. The black line is the* FLUKA *calculation. The red and blue lines show, respectively, the contribution from primary ions and secondary fragments. Plot from [Mai08].*

the projectile break-up into an α and a projectile like fragment (^{8}Be in case of ^{12}C projectiles). One of these fragments may fuse with the target nucleus, while the other one, the spectator, continues almost unperturbed. However, ^{8}Be is a weakly bound state of two α's, and decay almost immediately. Ergo the α's spectra from inclusive experiments contain both the α produced directly in the interaction of the projectile with the target and the α's coming from the subsequent decay of ^{8}Be. When the projectile breaks up via a peripheral interaction and all the fragments produced do not suffer any further interaction, their velocity is close to the original beam velocity: this kind of process is called "quasi-elastic". More recent experiments [BBC+96; GBC+97; GBCF98] studied the angular distributions of many residues produced in the interaction of ^{12}C on ^{103}Rh with energies from the Coulomb barrier up to 400 MeV showing that, in addition to the spectator fragment, a significant amount of α particles is coming from pre-equilibrium processes, evaporation and a large fraction from incomplete fusion processes. The emission of the majority of these ejectiles occurs in a time period much smaller than the time required for the composite nuclear system to reach statistical equilibrium. Thus they are re-emitted with only a slight reduction of their initial energy after a few interactions with target nucleons [GCF+99]. Gadioli et al. [GCF+99] measured the inclusive double-differential cross sections of α particles emitted in the interaction of ^{12}C ions with ^{59}Co and ^{93}Nb at incident energies of 300 and 400 MeV isolating the contributions of the different reaction mechanisms. They concluded that "it would be desirable to design experiments for exclusive measurements as a definitive check".

The experiment described in this work has been done exactly to study exclusively the quasi-elastic breakup of ^{12}C in ^{8}Be and ^{4}He. To insulate this channel, detecting the two fragments in correlation, two set of detectors have been used. The arm on which was mounted the detector made to measure the α fragments has been placed at different angles respect to the beam direction, in order to study the angular dependence of the interaction. This experiment is the only one that measured the

^{12}C fragmentation in an exclusive way in this energy range.

The energy of the beam used in this experiment, namely 33 MeV u^{-1}, is of particular importance, since it is the typical energy range of ^{12}C close to the Bragg peak, as it is possible to see in Figure 1.4.

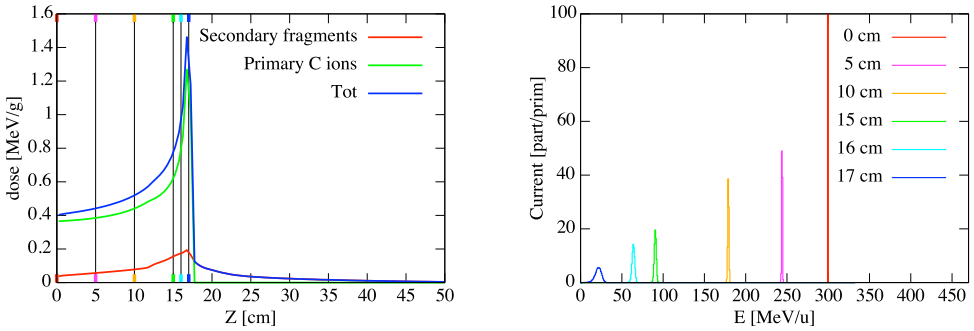

(a) (b)

Figure 1.4. *The left panel shows the dose deposited by* 300 MeV u^{-1} ^{12}C *ions as a function of their penetration in water. In blue the total dose deposited, the green line shows the fraction of the total dose deposited directly by the primary beam particles and the red line shows the dose fraction deposited by secondary fragments. The right panel shows the spectra of the primary* ^{12}C *at 5 different depths in the target, namely* 5, 10, 15, 16 *and* 17 cm. *These depths are indicated in the left panel by the coloured lines on the x axis.*

1.4 Monte Carlo codes for ion beam therapy

Full MC, considered the gold standard for dosimetric calculations, are used since long time in conventional radiotherapy [Rog06] and in hadrontherapy. However, as MC codes are currently too time-consuming to be used for routine treatment, clinical dose calculations are usually made with pencil beam algorithms, which are considered to offer a reasonable compromise between accuracy and computational speed for treatment planning. Pencil beam algorithms model the dose delivered to an heterogeneous tissue as dose deposition to a water-equivalent system in beam's eye view. These algorithms need some physical quantities that are computed with MC codes, such as the depth-dose distribution in water for different ions. For instance, FLUKA has been used to compute the input parameters of the treatment planning system that is in clinical use for both Protons and Carbon ions since the start of patient treatment in November 2009 in HIT [PMB+12].

In addition to basic parameter generation, MC codes are applied to validate dose calculations, especially in cases with great tissue heterogeneities [MMM+13], and are used to accurately analyse the dose delivered to patients. Eventually, they can also reduce the necessity of experimental dosimetric treatment verification currently performed for each individual clinical treatment prior to the first day of treatment [Par11]. Additional areas of MC applications for ion beam therapy are:

- beam line modelling [PJPSE08]

- support for dosimetric and biological experiments [PBE+08]
- risk-estimation for secondary cancer induction [YMN12]
- radioprotection

MC codes are also used for the estimation of the production of $\beta+$ emitters, such as ^{11}C and ^{15}O, since they can allow a non-invasive verification of the treatment via Positron Emission Tomography (PET) imaging during or shortly after the treatment itself. However, the density of activated isotopes is not directly proportional to the delivered dose and MC can be used to infer the dose as function of the measured density of annihilation photons [BBB+08].

1.5 FLUKA code capabilities

FLUktuierende KAskade or Fluctuating Cascade (FLUKA) [FSFR05; BCC+14] is a particle physics MC package. It is capable of handling transport and interactions of hadronic and electromagnetic particles in any material over a wide energy range, from thermal neutrons to cosmic rays. FLUKA is intrinsically an analogue code, but can be run in biased mode for a variety of deep penetration applications.

An original Multiple Coulomb scattering algorithm for the transport of charged particles, which includes an optional single scattering method, has been implemented in FLUKA [FSGP92]. The treatment of ionisation energy loss is based on a statistical approach [AFSR97]. This approach reproduces fairly well the average ionisation with inclusion of nuclear form factors to heavy ion transport. In addition uses up-to-date effective charge parametrisations and describes straggling of ion energy loss in normal first Born approximation with inclusion of charge exchange effects. FLUKA has been benchmarked [SPF+06] against experimental data concerning ion beams relevant for hadrontherapy.

The geometry of the problem is described using a combinatorial boolean approach [Emm75]. It is also possible to describe the geometry using voxels, possibility that allows detailed tridimensional representations of human beings using computed tomography scans. This feature is particularly useful for dosimetry or treatment planning purposes.

As other physics models in FLUKA, the hadronic models follow the modelling strategy "theory-driven and benchmarked with data at the single-interaction level". Predictions are obtained with a minimal set of free parameters which are fixed for all energies and target-projectile combinations [FS02]. Consequently, reaction channels and energies are sampled from physics models, except for low energy neutrons (less than 20 MeV), for which differential hadronic cross sections are explicitly tabulated with a fine energy mesh [CFP91].

Depending on the projectile energy, two kinds of model are used for the description of hadron-nucleon interactions: these based on individual resonance production and decays (up to 5 GeV), and these based on parton string models [FS98]. The Dual Parton Model and Jets (DPMJET), based on the Dual Parton Model (DPM) [RER00], is used at high energies, beyond few tens of TeV.

Two models are used also in hadron-nucleus interaction: Pre-Equilibrium Approach to NUclear Thermalization (PEANUT) and DPMJET for energies greater

than 20 TeV. PEANUT includes a very detailed Generalised Intra-Nuclear Cascade (GINC) and a pre-equilibrium stage and at higher energies, the Gribov-Glauber multiple collision mechanism is also included. A pre-equilibrium model is a transition between the first steps of the reaction and the final thermalisation.

Nucleus-nucleus interactions are treated by the following models:

- Boltzmann Master Equation (BME) [CBC06], in the low energy region below $0.15\,\mathrm{GeV\,u^{-1}}$
- Relativistic Quantum Molecular Dynamics (RQMD) [ABB+04], between $0.15\,\mathrm{GeV\,u^{-1}}$ and $5\,\mathrm{GeV\,u^{-1}}$
- DPMJET, above $5\,\mathrm{GeV\,u^{-1}}$

Alternatively, depending on the cross sections of the two processes, two nuclei can interact electromagnetically and one of them, or even both, can dissociate [BFF+14]. The electromagnetic dissociation is treated in section section 5.2.

All the models described can produce excited fragments. If the mass number of the fragment is smaller than 17, the deexcitation is described using an extended Fermi break-up model. If it is higher, the fragment can go in evaporation or fission, depending on the cross section, which in turn is function of the excitation energy. After this first step of deexcitation, all fragments can emit γ rays. A schematic flow chart of the nuclear interactions in FLUKA is depicted in Figure 1.5.

Hereinafter, the focus will be put on the lower energy nuclear interaction models, relevant for hadrontherapy (up to $100\,\mathrm{MeV\,u^{-1}}$) and for the simulations made for this work ($33\,\mathrm{MeV\,u^{-1}}$). At such low energies, pion production is energetically impossible in both nucleon-nucleon and nucleon-nuclei interactions. Hence nuclear interactions at those energies consist of elastic nucleon-nucleon scatterings, that can result in nucleon and light fragment emissions and can leave the remaining nuclei in an excited state.

1.6 Hadron-Nucleus interaction

In PEANUT the reaction mechanism is modelled by assuming a series of independent nucleon-nucleon collisions, i.e. an intra-nuclear cascade, smoothly joined to statical pre-equilibrium emission if the energies of the nucleons are smaller than 50 MeV. However, to ensure continuity, in the region between 50 MeV and 10 MeV the nucleons are still transported and, even though the interactions are not explicitly performed, the exciton number is increased and the pre-equilibrium stage will further develop the configuration. The statistical approach is used in the low-energy region, as the physical foundation of the intra-nuclear cascade approach becomes invalid and can be very time consuming as well.

In the intra-nuclear cascade, energy and momentum are conserved taking into account the recoil of the residual nucleus. All the particles are transported considering the Coulomb and nuclear potentials. Path length and interaction mechanisms are chosen depending on the particle nucleon cross section and local density. The latter is evaluated as a function of the radius.

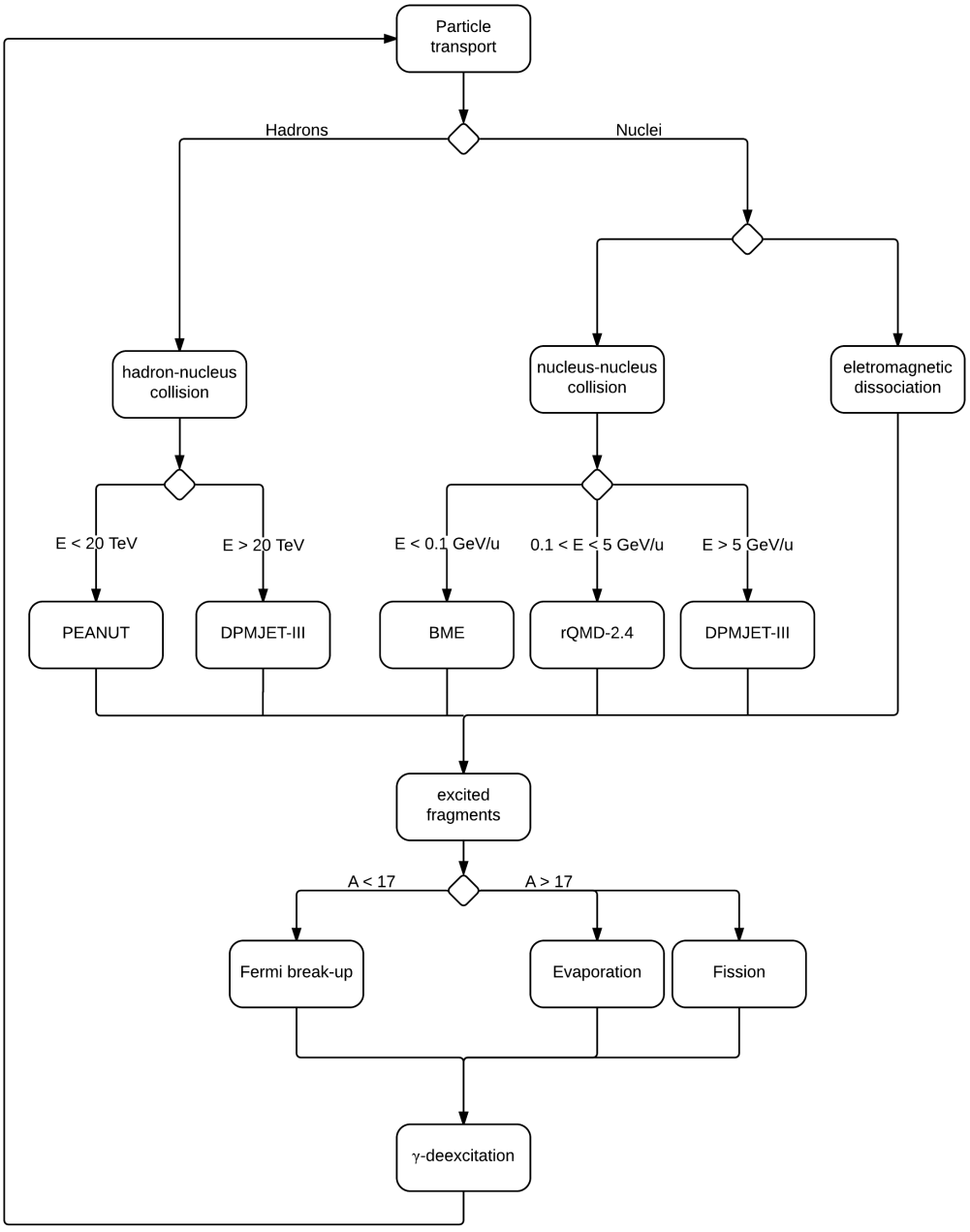

Figure 1.5. *Schematic flowchart of nuclear interactions and subsequent fragments production in* FLUKA.

A rejection method is applied to check, after each interaction, that the momenta of all secondary nucleons are above the Fermi level, to take into account Pauli's exclusion principle. This increases the mean free path in a nuclear medium. Others have the same influence. Among them, we can cite:

- nucleon anti-symmetrisation [BM69], which decreases the probability for secondary particles to re-interact with a nucleon of the same type very close to the production point
- nucleon-nucleon hard-core correlations [eal71], which also prevent secondary particles to collide again too close to the production point. Typical hard-core radii used are in the range $0.5 \div 1\,\mathrm{fm}$
- "*coherence*" length after elastic or charge exchange hadron-nucleon scatterings, because such interactions cannot be localised better than the position uncertainty connected with the four-momentum transfer of the collision.

Nucleon-nucleon total cross sections, both elastic and inelastic, are taken from available experimental data.

The pre-equilibrium statistical approach used in PEANUT is the exciton formalism, based on the so called Geometry Dependent Hybrid Model (GDH) [Bla71; Bla72; BV83; Bla83]. It consists in a recursive process where at each step a nucleon-nucleon collision can increase the number of excitons by two. An exciton can be either a particle above the Fermi level or a hole below it. At each step the probability of emitting a nucleon in the continuum is calculated. Indeed, at each step of the nucleon-nucleon interactions chain there is a probability $P(\epsilon)$ of emitting a nucleon in the continuum with energy ϵ. This probability can be factored in two parts: the first term gives the probability to have a particle with energy ϵ; the second one express the probability of the exciton cluster to escape from the nucleus.

$$P(\epsilon) = \frac{\rho(U,\epsilon) g d\epsilon}{\rho(E)} \frac{r_c(\epsilon)}{r_c(\epsilon) + r_+(\epsilon)} \tag{1.9}$$

where g is the exciton state density; U is the residual nucleus excitation energy, i.e. $U = E - \epsilon - B$; and $\rho(E)$ is the density of exciton states, and is given by:

$$\rho(E) = \frac{g \cdot (gE)^{n-1}}{n!(n-1)!} \tag{1.10}$$

$r_c(\epsilon)$ is the rate of emission in the continuum and $r_+(\epsilon)$ is the exciton re-interaction rate, and can be calculated from the nucleon mean free path in nuclear matter.

$$r_+ = f_{Pauli}(\epsilon, E_F) \left[\rho_{pro}\sigma_{xp} + \rho_{neu}\sigma_{xn}\right] \left[\frac{2(\epsilon + V)}{M}\right]^{1/2} \tag{1.11}$$

where $V = E_F + B$ and f_{Pauli} is the Pauli's blocking suppression factor; M is the α mass; ρ_{pro} and ρ_{neu} are the densities respectively of protons and neutrons in the nucleus, σ_{xp} and σ_{xn} their cross section with the particle of kind x.

This model grounds on the assumption that all the possible partitions of the excitation energy E among n excitons are equiprobable. The recursive process stops,

and equilibrium is reached, when either the exciton number n is sufficiently high ($n = \sqrt{2gE}$, where g is the single particle level density) or the excitation energy is below any emission threshold. The initial number of excitons depends on the reaction type and on the cascade history.

1.7 Low energy ion interaction

In the BME framework, the reaction cross section (σ_r) between two ions is calculated using a model developed [CCG05] on the basis of the "*soft-spheres*" model proposed by P. J. Karol [Kar75]. Two different main reaction paths have been adopted to simulate the interactions: complete fusion, and peripheral collision. The choice between the two is made according to the partial cross section for complete fusion. From there, the probability of complete fusion is given by:

$$P_{c.f.} = \frac{\sigma_{c.f.}}{\sigma_r} \tag{1.12}$$

and the one of peripheral collision is:

$$P = 1 - P_{c.f.} \tag{1.13}$$

In case of complete fusion, the new nucleus is the aggregate of the target and projectile nuclei and is in an excited state. The de-excitation is simulated using the BME model, described in subsection 1.7.1. If the collision is peripheral, the model predicts the formation of two or three fragments and extracts an impact parameter according to a distribution that takes into account the dependence of the nuclear density on the radius. The three bodies are the projectile-like fragment, the target-like fragment and a middle system, also called "fireball". The latter fragment is preferentially excited and its mass number is obtained integrating the projectile and target nuclei density distribution, which is assumed shaped as a Woods Saxon function, up to radii of the two nuclei that include 99% of the mass of the nuclei. The emission angle of the target and projectile-like fragment (θ) respects to the direction of flight of the projectile in the center of mass frame is sampled from an exponential decreasing distribution $\exp(-k\theta)$ whose parameter k is a function of the fragments masses and of their energies. Their momentum moduli are sampled from a phenomenological energy loss distribution. The emission angle and the momentum modulus of the fireball are defined by the momentum conservation. The excitation energy, subtracted from the kinetic energy as energy lost, is shared between the three fragments preferring the fireball. The excitation energy of the fireball is a quadratic function of the mass of the fireball itself.

The *fireball* de-excitation is simulated using the BME model, if the two fragments that composed it fit in the pre-computed database, or PEANUT [FSFR05].

1.7.1 Boltzmann Master Equations

Nucleus-nucleus interactions produce excited nuclei that can be the residual part of the projectile, of the target nucleus or of a composition, even partial, of the two. As said before, to describe the thermalisation of the latter, when produced

in a certain region of the projectile and target parameters space, the Boltzmann Master Equation (BME) theory [CFGER98] is used. This theory estimates the time variation of nucleons momenta distribution as a result of their mutual interactions. The theory predict also the nucleons emission into the continuum, as separate entities or as part of a cluster. For this aim, the phase space is divided in bins of volume $\Delta V = 2\pi m \Delta\epsilon \Delta p_z$, where m is the nucleon mass, ϵ its energy and p_z its momentum projection along the beam axis. The time evolution of the occupation probability $n_i(\epsilon, \theta, t)$ of the bin i is calculated using a set of coupled differential equations:

$$\begin{aligned}\frac{d(n_i g_i)^P}{dt} = &\sum_{j,l,m} \Big[\omega^{PP}_{lm\to ij} g^P_l n^P_l g^P_m n^P_m \left(1-n^P_i\right)\left(1-n^P_j\right) + \\ &- \omega^{PP}_{ij\to lm} g^P_i n^P_i g^P_j n^P_j \left(1-n^P_l\right)\left(1-n^P_m\right)\Big] + \\ &+ \sum_{j,l,m} \Big[\omega^{PN}_{lm\to ij} g^P_l n^P_l g^N_m n^N_m \left(1-n^P_i\right)\left(1-n^N_j\right) + \\ &- \omega^{PN}_{ij\to lm} g^P_i n^P_i g^N_j n^N_j \left(1-n^P_l\right)\left(1-n^N_m\right)\Big] + \\ &- n^P_i g^P_i \omega^P_{i\to i'} g^P_{i'} \delta\left(\epsilon^P_i - \epsilon^P_F - B^P - \epsilon^P_{i'}\right) - \frac{dD^P_i}{dt}\end{aligned} \tag{1.14}$$

where P and N indicate respectively Protons and neutrons; g_i is the total number of states in the ith bin; the terms such as $\omega_{ij\to lm}$ are the transition probability per unit time that, in a two-nucleon interaction, nucleons in bins i and j go to bins l and m; $\omega^P_{i\to i'}$ is the single Proton emission probability from the bin i to the continuum and finally dD^P_i/dt is the depletion term which accounts for the Proton emission from the bin i as part of a cluster. A set of equation analogous to Equation 1.14 holds for the neutron states as well.

A cluster is defined as the coalescence of nucleons with momenta closer each other than a given value ($p_{c,F}$). If it is not emitted immediately, it is not considered as a cluster in the subsequent time step. The cluster formation probability w_c at time t in the portion of the phase space E_c, θ_c with Z_c Protons and N_c neutrons is:

$$w_c(E_c, \theta_c, t) = \prod_i \left(n^P_i(\epsilon, \theta, t)\right)^{P_i(E_c,\theta_c)Z_c} \cdot \prod_i \left(n^N_i(\epsilon, \theta, t)\right)^{P_i(E_c,\theta_c)N_c} \tag{1.15}$$

where $P_i(E_c, \theta_c)$ is the volume fraction of the bin i within a sphere of radius $p_{c,F}$ centred in E_c, θ_c in the phase space. The probability of emitting a neutron, with energy E_c in one of the bin of the momentum space can be obtained as a special case of the Equation 1.15 setting N_c as one and Z_c as zero, $P_i(E_c, \theta_c)$ is zero for all the combination E_c and θ_c except for the chosen one where it is one.

From the probability of formation of a cluster (Equation 1.15) it is possible to calculate the multiplicity spectrum of this cluster:

$$\frac{d^2 M_c(E'_c, \theta_c)}{dE'_c d\Omega_c} = \frac{R_c}{2\pi sin(\theta_c)} \int N_c(E_c, \theta_c, t) \frac{\sigma_{inv} v_c}{V} \rho_c(E'_c, \theta_c) dt \tag{1.16}$$

where E'_c is the cluster energy once emitted outside of the nucleus; σ_{inv} is the cross section for the inverse process, that is the cluster absorption from the residual nucleus; V is the volume of the continuum and cancels with an equal term appearing

in $\rho_c(E'_c, \theta_c)$, the density of cluster states in the continuum; R_c is the probability that the cluster is emitted after being formed

By integrating the Equation 1.14, it is possible to obtain the time evolution of the nucleons in the phase space, i.e. the thermalisation of the nucleus. The integral of the differential multiplicity (Equation 1.16) is the total number of fragments c produced.

Anyway, this approach cannot be implemented in a transport code such as FLUKA because the run-time calculation of the multiplicity spectra for all the possible ejectiles is too long. Thus the implementation of the BME in FLUKA has been done by precomputing off-line and then fitting the predicted ejectiles multiplicity and double-differential spectra with analytical expressions described by a small set of parameters [CBC06].

1.7.2 Fermi Break-up

The cascade and pre-equilibrium stages can produce excited nuclei. These nuclei are supposed to be in an equilibrated state, i.e. the excitation energy U is statistically shared among all possible configurations. Each nucleus is characterised by its mass, charge and excitation energy. Since the excitation energy can be higher than the separation energy, the emission of nucleons and light fragments is still possible.

As seen in the flow chart 1.5, for light nuclei (with $A \leq 17$) the so-called Fermi Break-up model [Fer50; ÉG67] is used to describe the emission of one or more fragments from the excited nucleus. The emission is simulated in only one step. The branching ratios between the possible ejectiles are calculated from phase space considerations. More specifically, the probability W for disassembling a nucleus of N neutrons, Z Protons, with an excitation energy U into n fragments ($n \geq 2$) is given by:

$$W = \frac{S_n}{G}\left[\frac{V_{\mathrm{br}}}{(2\pi\hbar)^3}\right]^{n-1}\left(\frac{1}{M^*}\prod_{i=1}^{n} m_i\right)^{3/2}\frac{(2\pi)^{3(n-1)/2}}{\Gamma(\frac{3}{2}(n-1))}E_{\mathrm{kin}}^{\frac{3n-5}{2}} \tag{1.17}$$

where E_{kin} is the total kinetic energy of all the fragments at the moment of break-up, M^* is the total mass ($M^* = U + M_A + M_Z$), m_i the mass of the i fragment and V_{br} is a volume of the order of the initial residual nucleus volume. The spin S_n and the permutation G factors are given by:

$$S_n = \prod_{i=1}^{n}(2S_i + 1), \qquad G = \prod_{j=1}^{k} n_j! \tag{1.18}$$

in which n_j is the number of identical particles of the jth kind.

Therefore, evaluating the probability 1.17 for all energetically allowed combinations of fragments, it is possible to extract the final state. In the FLUKA extension of the Fermi break-up formalism, constraints on available configurations and the centrifugal barrier (if $L = 0$ is forbidden) are taken into account in cases where the spin and parity of the excited nucleus are known [BCC+14].

In FLUKA, all stable particles with $A \leq 16$ and a few unstable isotopes, like ^{8}Be, are possible ejectiles. If the produced nucleus is unstable, it is left to decay

according to the experimental branching. Once the final state configuration has been selected, the kinematical quantities of each fragment are chosen according to n-body phase space distribution. Such a selection is performed taking into account the Coulomb repulsion between all charged particles. In practice, E_{kin} at disassembling is given by:

$$E_{\text{kin}} = U - \left(\sum_{i=1}^{n} m_i c^2 - M_{A,Z} c^2 \right) - B_{\text{Coul}} \tag{1.19}$$

where also the emitted fragments can be in an excited state. The total Coulomb barrier B_{Coul} of the selected configuration is distributed to charged particles after disassembling, in their own center of mass system.

Chapter 2

Experiment

2.1 Experimental Facility

The experiment was realised at iThemba Laboratories, a multidisciplinary facility located near Somerset West in Cape Town, South Africa. This laboratory provides accelerator and ancillary facilities that are used for research and training in nuclear and accelerator physics, radiation biophysics, radiochemical and material sciences, radio nuclide production and radiotherapy. Patients are treated during the day, and between treatments the beam is switched to the radio nuclide production vault. Over the weekend, beams of light, heavy ions and polarised protons are used for nuclear physics experiments.

The cyclotron in use can accelerate proton beams up to 200 MeV. It can also accelerate heavier ions to energies up to 33.3 MeV u^{-1} depending on the beam species. In this experiment, a ^{12}C beam of 33.3 MeV u^{-1} has been used.

2.2 Experimental Setup

This experiment was carried out in the A-line scattering chamber, which consists of a vacuum chamber of about 1.5 m in diameter and has a target ladder in the centre and two rotating arms to host the detectors. The ladder is in aluminium and can host up to five different targets arranged vertically. Both the detector arms and the target ladder can be moved remotely in order to change the setup without having to break the vacuum every time. During the data taking, the pressure in the scattering chamber has been kept around 10^{-5}mbar. The vacuum was made using in sequence a rotary pump to reach a pressure of 1 mbar, a turbomolecular pump up to 10^{-3}mbar, and finally a cryogenic pump.

Four different kinds of target have been used for the experiment under consideration: Carbon (C), Gold (Au), Niobium (Nb) and lastly, to explore the possibility of Hydrogen contamination on the targets surfaces, Polyethylene $\left((CH_2)_n\right)$. The thickness and the density of the targets are reported in table 2.1.

The set of detectors placed on the right arm is referred to as the "α telescope", while the set on the other arm as the "Be telescope". A schematic diagram of the experimental setup is shown in figure 2.1.

Table 2.1. *Thickness and density of the targets used in the experiment.*

Target material	Density [g cm^{-3}]	Thickness [µm]
C	2.0	5.265
Nb	1.05	0.466
Au	19.32	1.22
$(CH_2)_n$	0.96	6 [1]

The α telescope is constituted by a collimator, two silicon detectors and a sodium-iodide scintillator (NaI). The collimator is in brass and its thickness is 3 cm with a 1.4 cm diameter opening. As the distance between the target and the back of the collimator is 29.1 cm, the solid angle subtended by the acceptance of this telescope is 1.82 msr. The thickness of the first ($\Delta E1$) and of the second ($\Delta E2$) silicon detector is respectively 21 µm and 541 µm.

The ^{8}Be telescope consists of a Silicon Strip Detector (SSD) followed by a NaI, alike to the one in the α telescope. The SSD is made of 16 vertical strips. Each strip

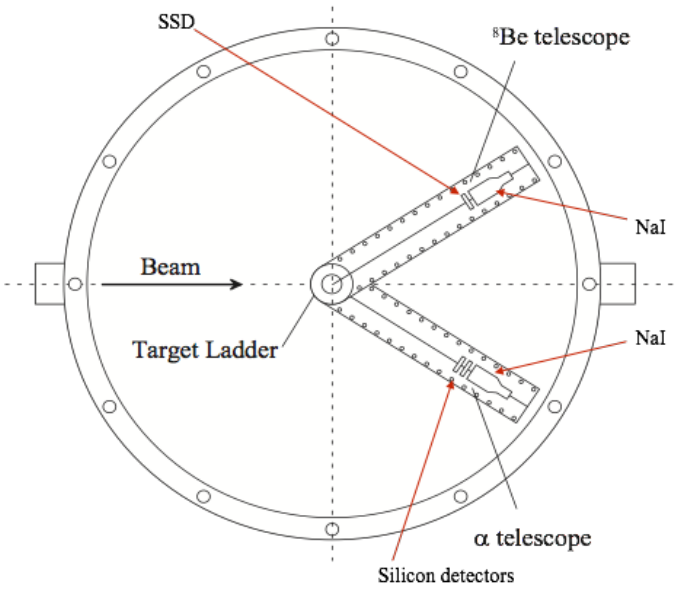

Figure 2.1. *Schematic diagram of the A-line scattering chamber showing the two rotating arms hosting the ^{8}Be telescope, composed by the SSD and a Sodium-iodide scintillator, and the α telescope, which consists of two silicon detectors and another Sodium-iodide scintillator. The distances between the target and the detectors are uninformative.*

is 3 mm wide with an inter-strip separation of 0.1 mm. The total active surface of the SSD is a square with a side of 5.0 cm and 251 µm thick. Between the SSD and the subsequent NaI there is a brass circular collimator with an inner diameter of 6.0 cm and the back side 56.89 cm far from the target (3.43 msr).

[1] This value is uncertain.

The two NaI's are identical: they are cylindrical with a diameter of 7.6 cm and thickness of 5.1 cm and both are coupled to a photomultiplier. A light pulser has been used to correct the instabilities in each of the photomultipliers. The NaI's have been protected from the atmospheric moisture in the scattering chamber before the vacuum with a 7 µm thick foil of Havar.

Two triggers have been defined, one for each telescope. The trigger relative to the ^{8}Be telescope fires when the SSD and the NaI measure an energy deposition; the α one fires when the $\Delta E1$ and the $\Delta E2$ or the $\Delta E2$ and the NaI go over the thresholds. The coincidence trigger fires when both the single telescope triggers fire. All the coincidence triggers and 5% of the single trigger events are acquired, the latter in order to be compared with the data already published in [GSB+01]. More details about the experiment setup can be found in [Mir11]. To measure also the angular dependence of the quasi-elastic ^{12}C break-up, different runs have been performed with the α telescope placed at 16°, 18°, 20°, 22° and 24° from the beam axis, while the ^{8}Be telescope is always placed at 9°.

2.2.1 Calibration

The energy calibration of the $\Delta E2$ and the SSD has been performed in vacuum placing a ^{208}Th source in the scattering chamber. A typical spectrum can be seen in figure 2.2. As the highest energy α emitted from the ^{208}Th has 8.78 MeV,

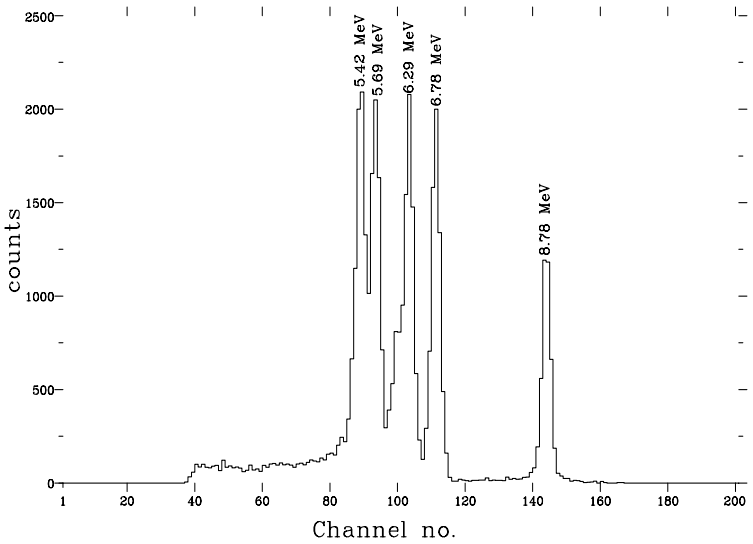

Figure 2.2. *Typical spectrum of ^{208}Th measured with the $\Delta E2$. Plot from [Mir11].*

the calibration points obtained from the ^{208}Th have been complemented with the measurement of the elastic peak of the ^{12}C scattered from a thin gold target. The elastic peak has been measured placing the detectors at different angles from 8° to 15°. The slope and the offset used to convert the acquired values in energy have been obtained with a linear fit of the two data sets.

Since the $\Delta E1$ silicon detector is not thick enough to stop the α particle emitted by the ^{208}Th, it has originally been calibrated fitting the measured energy loss of

α particle stopped in the $\Delta E2$ detector with the value predicted by the ELOSS program [Jip84]. This calibration is constrained to go through the origin and the fit has been used to calculate the value of the angular coefficient. During the analysis, a small discrepancy has been found between the data and the MC in the response of the $\Delta E1$ detector. It has been hypothesised that this discrepancy is ascribable to the calibration. For this reason, the calibration has been modified. The energy deposited in the $\Delta E1$ by α particles in the energy range $0 \div 35$ MeV, i.e. the α's stopped by the $\Delta E2$, has been recalculated making a dedicated simulation with FLUKA. These values are shown in Figure 2.3. The correction to the calibration

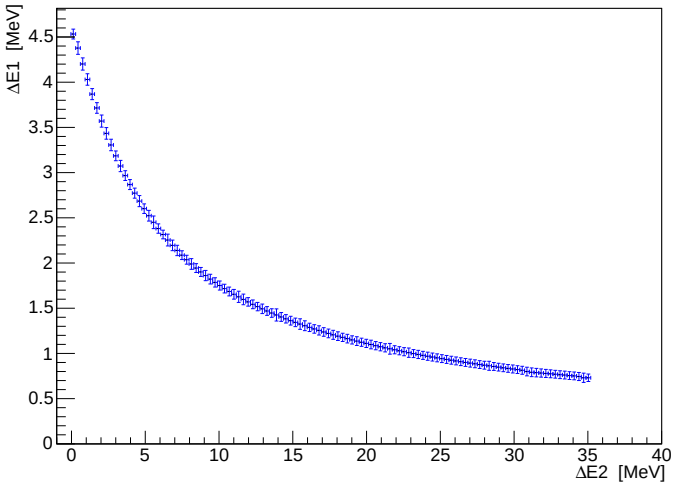

Figure 2.3. *Energy deposited in* $\Delta E1$ *as a function of the energy deposited in* $\Delta E2$ *by a particles calculated with a* FLUKA *simulation.*

has been done minimising the function:

$$\chi^2(m,q) = \sum_{i=1}^{Nbin} \frac{\Big[(m \cdot \langle Exp_i \rangle + q) - MC_i\Big]^2}{\sigma^2_{Exp_i} + \sigma^2_{MCi}} \tag{2.1}$$

where $\langle Exp_i \rangle$ is the average of the energy deposited in the $\Delta E1$ for each bin of the energy deposited by the α's in the $\Delta E2$ detector. The α's are selected in a similar way as described in 4.4, but the energy deposited in the NaI placed after the two silicon detectors of the α telescope must be zero in order to select only the α that stops in the $\Delta E2$. MC_i are the calculated energy deposition in $\Delta E1$ with the MC simulation. $\sigma^2_{Exp_i}$ and σ^2_{MCi} are respectively the variance of $\langle Exp_i \rangle$ and MC_i. m and q are the parameters of the calibration, m is a multiplicative factor to correct the calibration previously done, and q the offset left as a free parameter for the minimisation. The result of the minimisation, made with MINUIT2 [JR75], is shown in Table 2.2

The original calibration was made imposing the intercept to be zero. Conversely, letting the intercept as a free parameter, its best value is not compatible with zero

Table 2.2. *Correction parameters to the calibration of the $\Delta E1$ calibration.*

	Value	σ
m	0.9	0.1
q [MeV]	0.10	0.02

and is of the order of magnitude of the offset subtracted during the data taking. The best value for the angular coefficient is 10% smaller. The effect of this correction is shown in Figure 2.4 and is more evident in the region of high $\Delta E1$.

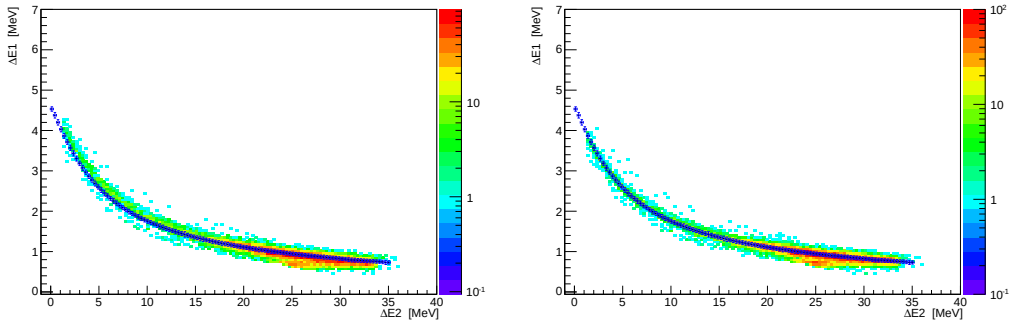

(a) (b)

Figure 2.4. *Energy measured by the $\Delta E1$ detector as a function of the energy measured by the $\Delta E2$ detector. The blue points are the value calculated with a MC simulation and seen in Figure 2.3. The left panel shows the data with the original $\Delta E1$ calibration while the right one shows the data with the new calibration, with the intercept as a free parameter. The difference between the two calibrations is more evident in the region of high $\Delta E1$.*

The two NaI's have been calibrated using only the ^{12}C elastic peak response as normalization parameter for the light output predicted by the model of Michaelian et al. [MMRBM93], more details about the calibration of the two NaI's can be found in [SFL+05].

2.2.2 Data preparation

The data were originally stored in a binary format for VAX servers. To perform the analysis using ROOT [BR97] the data have been converted in ROOT files. The conversion has been done in two steps: firstly a Fortran program has been developed to export the binary file from the VAX server into a CSV file, secondly these files have been converted in `TTree` ROOT files using a C++ program. For each run, a different file has been created to keep the size of each file small and easy to handle. Each file contains also the information about the pulser of the two NaI's and the calibration parameters of all the detectors.

Chapter 3

Monte Carlo simulation

A complete simulation of the full experiment has been set up. As a first step, the geometry of the experiment in the simulation was designed using the combinatorial

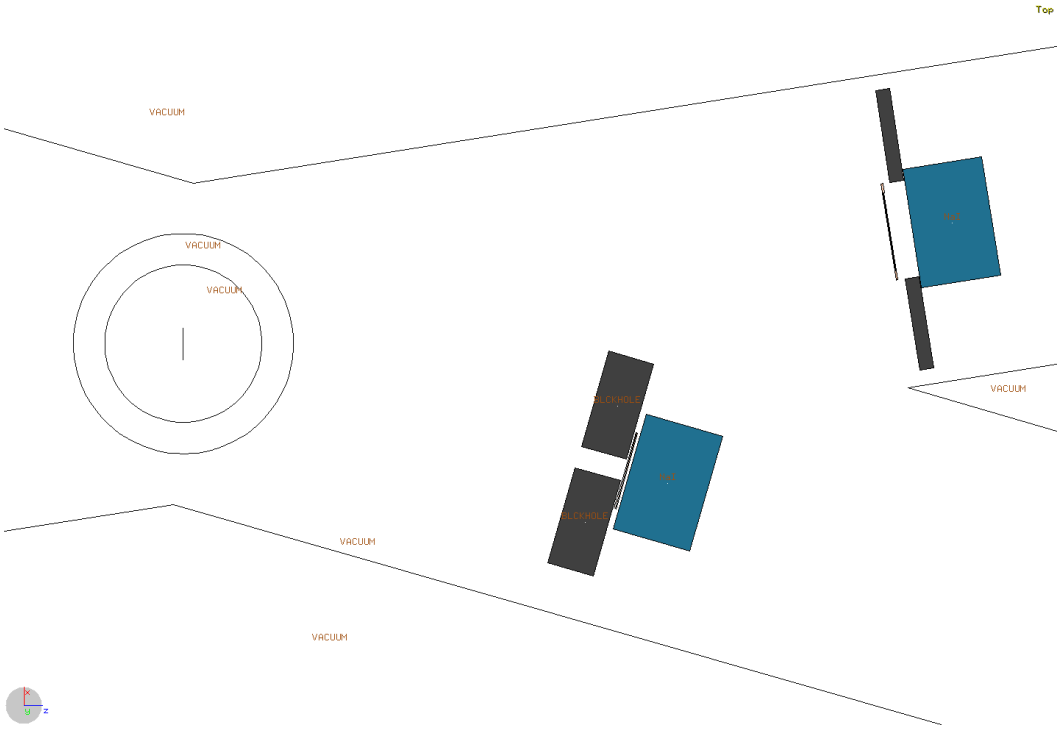

Figure 3.1. *The sketch of the experiment in the Monte Carlo simulation (MC). The target is the vertical line on the left, the spherical crown that surrounds the target is the one used to rotate each event. The SSD and the silicon detectors of the a telescope are not clearly visible because they are too thin. The lines that surrounds all the geometry are the limit for the transport of particles.*

approach of FLUKA. In this paragraph the geometry of the experiment is briefly described to explain how it is represented in the simulation (the complete description of the detectors is in chapter 2).

All the detectors were designed on the Z axis, the one parallel to the beam, and

then rotated by the proper angle, thus allowing to modify easily the angle of the α telescope for the different runs.

In the experiment there are two collimators. One is placed in front of the first silicon detector ($\Delta E1$) in the α telescope and the second one is placed between the SSD and the NaI in the ^{8}Be telescope; both are made of brass while in the simulation they are made of a special material called "*blackhole*". In FLUKA any particle that enters a region made of this material is not transported anymore. This approximation is validated by a dedicated simulation (plots 3.2 and 3.3) with the collimators in brass. This simulation showes that the current of charged particles out coming from the collimators is two order of magnitudes less than the current of charged particles passing through the collimators. Therefore, the secondary particles production in the two collimators can be neglected.

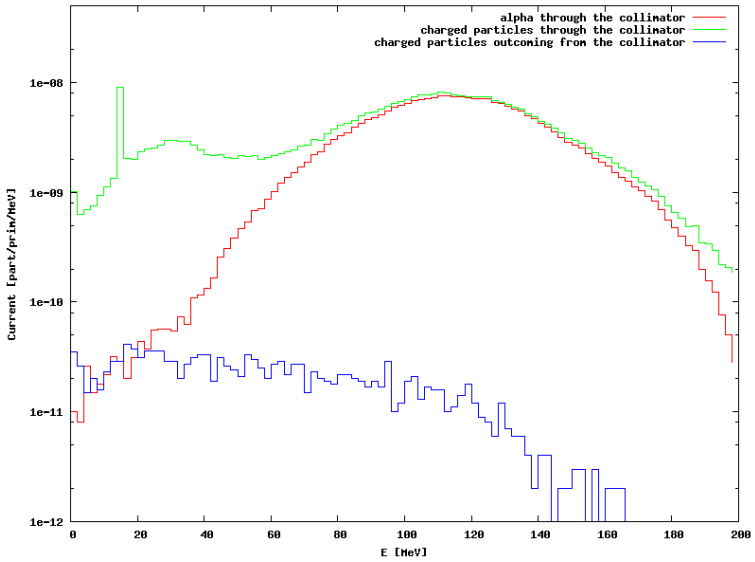

Figure 3.2. *Currents of charged particles (green) and α (red) passing through the ^{8}Be telescope collimator and current of charged particles produced in the collimator (blue).*

The description of the α telescope is quite simple: two cylindric silicon detectors which have a sensitive area larger than the collimator in front of them and a cylindrical NaI scintillator at the end.

The ^{8}Be telescope is more complex: the first element is the SSD. This detector is made of one silicon layer divided in 16 strips. As in MC each strip is a separate region, the energy deposition can be scored in each of them separately. After the SSD there is one of the collimators, followed by a NaI scintillator. The area subtended by this collimator is smaller than the SSD active surface. Indeed, as the active area of the SSD has the shape of a square with a side of 5 cm while the collimator is circular with a diameter of 6 cm, it is necessary to insert in the simulation also the frame of the SSD. The SSD frame is made of epoxy resin with an increased density ($1.85\,\mathrm{g\,cm^{-2}}$) because moulded epoxy has fillers of glass fiber. A layer of 50 µm in copper has been added to simulate the printed circuit board. Also the Havar window in front of the two NaI detectors has been inserted in the simulation. A sketch of

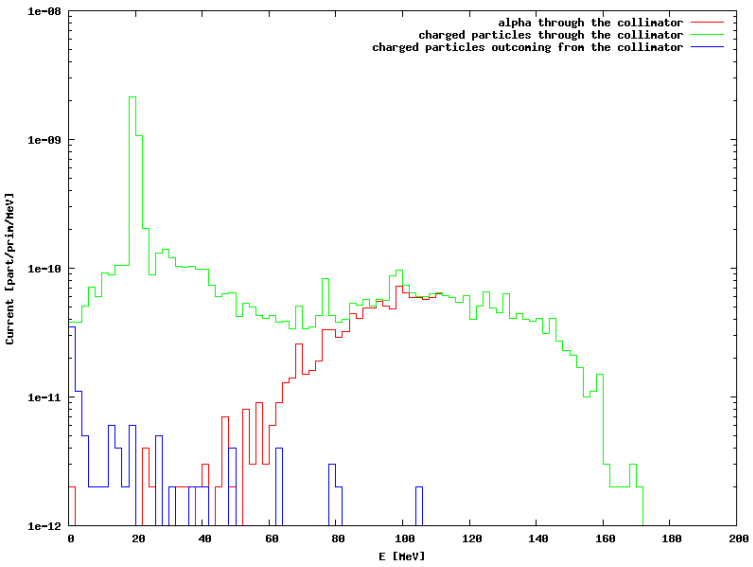

Figure 3.3. *Currents of charged particles (green) and a (red) passing through the a telescope collimator and current of charged particles produced in the collimator (blue).*

the modelled geometry is shown in figure 3.1.

Since the targets used in the experiment are all very thin, (see table 2.1 in Chapter 2) the MC starts directly with the simulation of the interaction between the projectile and the target nuclei without transporting a primary bream particle through the target. Afterwords, the output is weighted by the cross section of the process. To investigate the hypothesis of a H contamination in the targets and simulate the Polyethylene one, the MC has been run twice, once to simulate the H and once for the other element.

3.1 Implementation of the simulation

For analysis purpose, the data are scored event by event, making extensive use of `user routines` developed for this analysis. A `common`, to save the information for each event, has been defined. A flow chart of the code is presented in figure 3.4.

When a new secondary particle is placed in the stack, its data and data about the particle and the interaction that generated it are saved. Furthermore a variable that counts the number of secondaries in the event is incremented. This progressive number is used also as a flag to identify the particle in each of the subsequent steps.

For each detector an array has been defined. Each element in the array is used to score the energy deposition of one particle. The strips of the SSD are treated as separate detectors, indeed the energy deposition is saved separately for each of them. For the two NaI scintillators, the energy deposition and the light output simulating the quenching are saved. Details about the simulation of the quenching will be given in section 3.3. The energy deposition are saved also for some of the passive elements of the geometry, such as the Havar windows placed in front of the scintillators and the SSD frame.

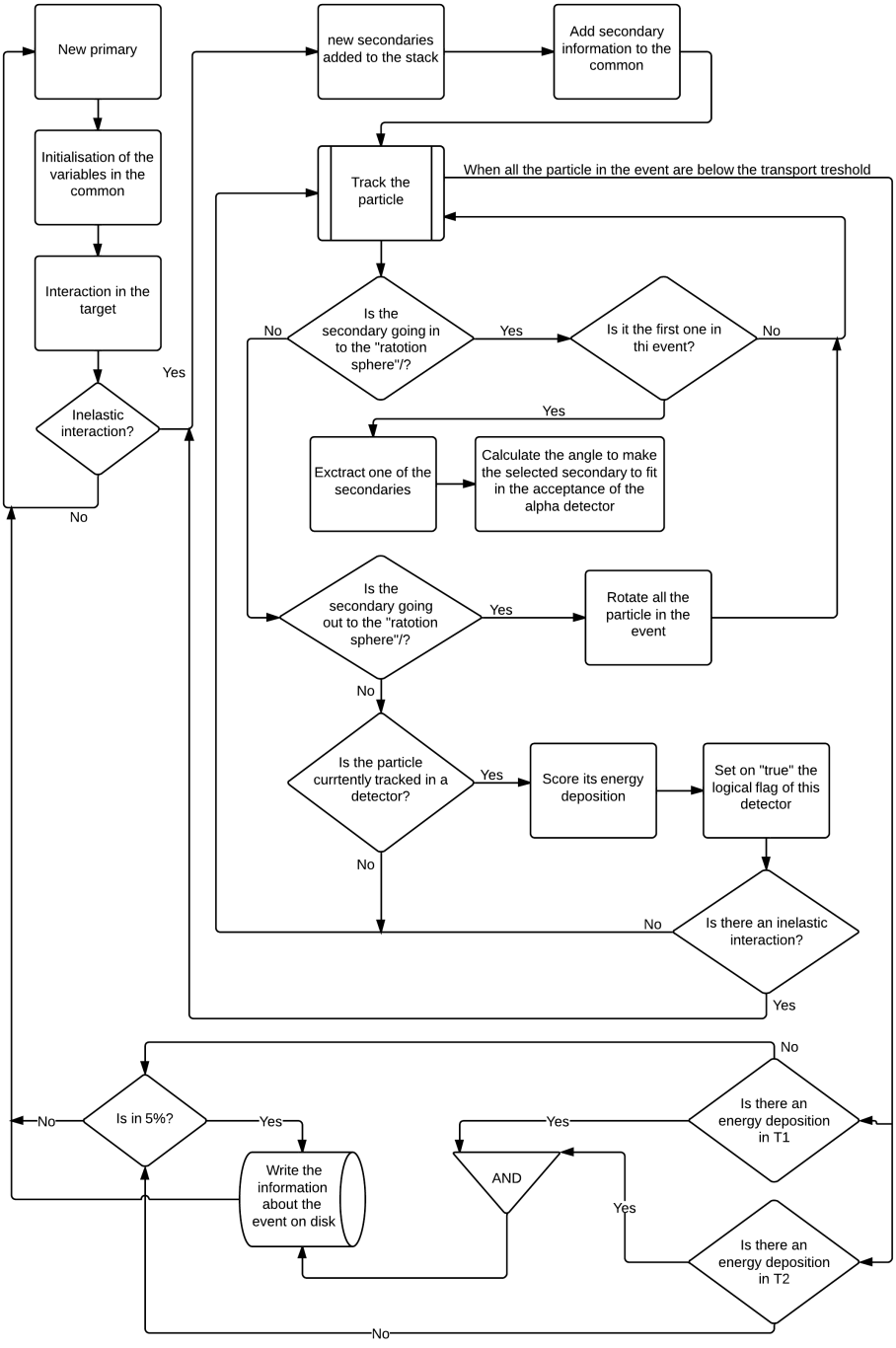

Figure 3.4. *Flow chart of the MC simulation, underling the relevant part of the* `user routines`.

As in the experiment, a single trigger for each telescope has been defined. In the ^{8}Be telescope, the trigger is the coincidence between one strip of the SSD and the NaI that is placed after it; in the α telescope, it is the coincidence of two of the three detectors. All the coincidences between the two telescopes triggers and 5% of the single trigger events are stored. To simulate the experimental output, also the information about the trigger that fired is saved.

3.2 Biasing

In order to speed up the simulation a biasing technique has been used: each event is rotated to recover events that otherwise go out of the small angular acceptance of the α telescope. Two spheres around the target have been defined, as seen in Figure 3.1. When the first particle crosses the inner sphere, one of the secondaries possibly produced in the target is randomly selected. If this one does not point in the red slice of 12° seen in Figure 3.5, the event will be rotated. The rotation is an integer multiple of 12°, this means that the probability that the event will go in the acceptance of the α telescope is increased by a factor of 30. The particle used

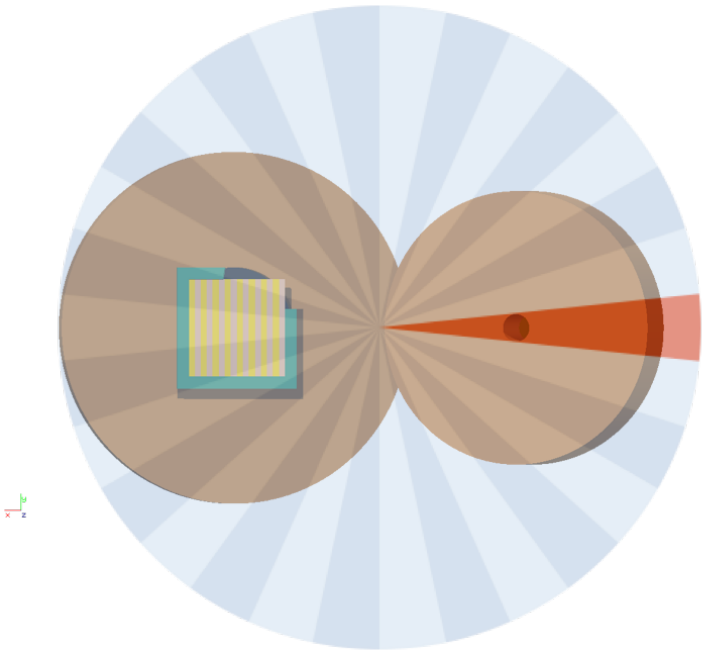

Figure 3.5. *Sketch of the experimental setup as seen from the target along the Z axis. On the left is represented the SSD and the Be telescope collimator, on the right the a telescope collimator. The blue circle shows the 30 slices of* 12° *each in which the azimuthal angles has been divided. If the selected secondary particle does not point in the red slice a rotation of the all event is performed by an integer multiple of* 12° *to make this secondary fit in the red slice.*

to calculate the rotation is chosen randomly since the order that the code use to emit, and then transport, the particles produced in each interaction is not random. In this way is avoided the biasing that could be, if the rotation angle is computed

using always the first secondary particle as reference. The angle of the rotation is calculated when the chosen secondary particle crosses the inner sphere. However, the rotation is applied to all particles belonging to this event when they cross the outer sphere. As seen in figure 3.6 the angular distribution is flat, as expected, within statistical fluctuations (only the first and the last bins are roughly 1/2 of the others, but both rotate by the same quantity).

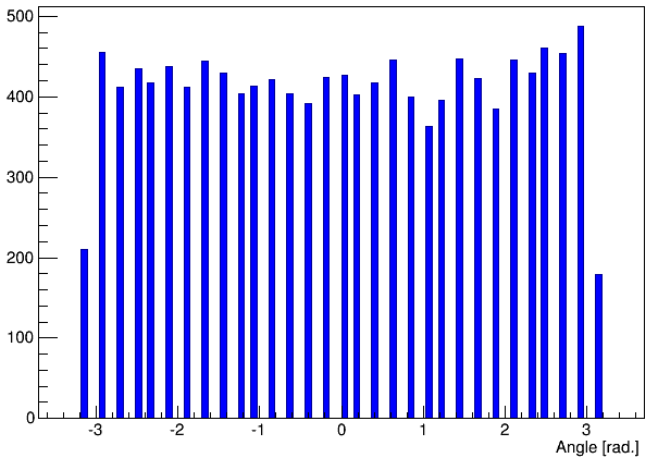

Figure 3.6. *Angles used to rotate each event to put at least one secondary particle in the direction of the a detector.*

3.3 Quenching in the NaI detectors

To simulate the quenching in the NaI detectors, a standard Birks law [Bir64] has been implemented in FLUKA as [FLU11]:

$$\frac{dL}{dE} = \frac{1}{1 + c_1 \cdot dE/dX + c_2 \cdot (dE/dX)^2} \cdot \tag{3.1}$$

The values for NaI scintillators published in [KIK11] were used: $c_1 = 9.1{\cdot}10^{-4}$g/MeVcm^2 and no c_2= term. These values are obtained from a fit to data taken using electrons, ^{4}He, ^{12}C, and ^{40}Ar.

As seen in figure 3.7 the agreement between the simulation and the experimental data published in [SFL+05] is not completely satisfactory: the difference in the response for α and ^{12}C is overestimated. The comparison with those data is very important since they are taken with the same detectors used for this experiment.

It also seems that the Birks' law does not reproduce very well the quenching in the region of the low energy loss [KIK11], better described by the Romero's [RNB91] formula:

$$\frac{dL}{dE} = \sum_{i=0}^{5} a_i \left[\ln \left(I \frac{dE}{dx} \right) \right]^i \tag{3.2}$$

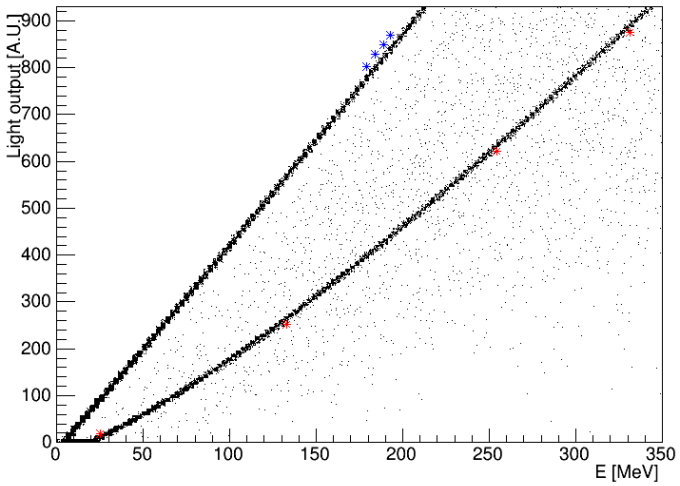

Figure 3.7. *Light output of the NaI, the black histogram is the simulation for ^{12}C and a using the Birks' law (eq. 3.1). The red and blue dots are experimental points from [SFL+05] for He and C respectively.*

where I is a constant that has the value of $1\,\mathrm{g\,cm^2\,MeV^{-1}}$. The coefficients a_i are a-dimensional and obtained with a fit from experimental data. The set of values that let the equation 3.2 better fit the data are reported in the table 3.1 and are obtained with experiments made using beams of electrons, protons, deuterons, α, ^{20}Ne and Na [RNB91].

Table 3.1. *Coefficients used in the equation 3.2. From [RNB91]*

a_0	0.68
a_1	0.12
a_2	0.045
a_3	-0.022
a_4	$2.3 \cdot 10^{-3}$
a_5	$-7.3 \cdot 10^{-5}$

As seen in figure 3.8 this implementation describes better the differences in light output of a NaI detector between α and ^{12}C. There is a small discrepancy, but it is in the high energy region of the ^{12}C ions and it should not affect the simulation. In fact, high energy ^{12}C ions will not reach the detector in the MC simulation and would not match the selection criteria anyway.

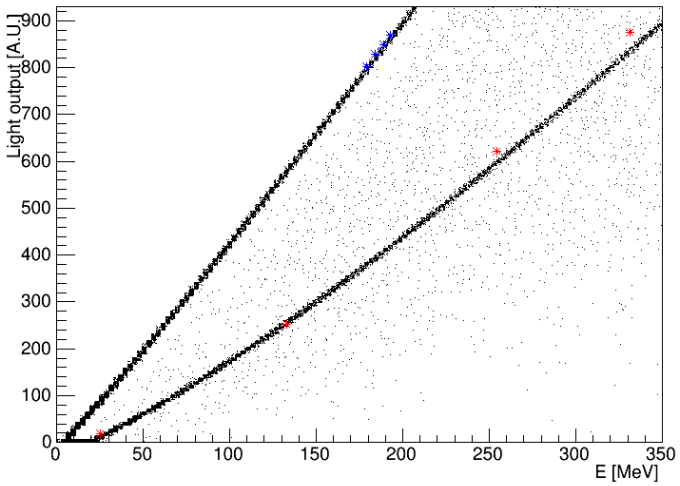

Figure 3.8. *Same as Figure 3.7 but the simulation is made using the Romero's description of the Birks law (eq. 3.2).*

3.4 Data preparation

When one of the possible triggers fires, the event is written on disk. For each event several lines are written, each of them starts with a string that identifies the line itself. The first line of each event contains information about the event in general, such as the number of the primary (it is a sequential counter for the primaries simulated), the number of secondaries in the event, the trigger that fired, the number of secondaries produced in the target and the flag of the secondary particle extracted to calculate the angle used to rotate the event.

Afterwards, for each secondary the program writes:

- the particle ID;
- the sequential flag assigned to recognise them;
- a flag to distinguish the interaction that produced this secondary;
- the particle id of the particle that generated it;
- the sequential flag of the particle that generated it;
- the number of the generation, i.e. 0 for the primary, 1 for the particle generated from the primary and so on;
- the energy deposition in each detector and relevant passive element, except the SSD;
- the statistical weight;
- the light output of the two NaI scintillators.

The strips of the SSD, but only those where there is an energy deposition, are written one by one. In other words, for each secondary there is a line if the secondary deposited some energy in one strip. The information saved includes the strip number, the particle flag (to check that there was no error in the identification) and the energy deposition.

After the data about the secondaries, information about the last Fermi breakup -such as the number of fragments produced, their atomic and mass number and their excitation energy- are stored.

As for the experimental data, a program in C++ to convert the output of FLUKA in ROOT data files has been developed.

Inside this program the variables and branch names for all the quantities that exist also in the experimental data have the same name, in order to allow the use of the same code for the analysis of the MC and experimental data.

For each simulation run, a ROOT file has been created in order to have files of small size. During the analysis all the data, relative to the same experimental conditions, are collected from the different files in a `TChain`.

To speed up the running of the code for each simulation, 50 different simulations are executed in parallel with different random seeds.

Chapter 4

Data Analysis

This chapter presents the description of the experimental data analysis starting from the MC simulation described in chapter 3. The FLUKA framework has been used to simulate the response of the detectors and the kinematic of the ^{8}Be decay to address the selection criteria.

4.1 Scintillator resolution

In order to reproduce the resolution of the two NaI's, a convolution with a Gaussian distribution centred in 0 has been applied to the simulated light output in the analysis code. Since the two NaI's have different resolutions they have been evaluated separately using their response to the elastic scattered beam particles.

The selection of the beam particles in the Be telescope has been performed taking only the single triggers of the ^{8}Be telescope, and using only one strip of the SSD, to reduce the angular acceptance. The C scattered ion are selected requiring an energy deposition in the chosen strip greater than 19 MeV. The events selected in this way are shown in Figure 4.1.

For the NaI in the α telescope it has been requested that the energy deposition in the $\Delta E1$ is in the range $2 \div 3$ MeV because the energy loss the C ion with this energy is 2.4 MeV. The event selected for the α telescope are shown in Figure 4.2. They are much less than in the Figure 4.1 because the Be telescope is at 9° respect to the beam axis, while the α one is at least at 16°, the configuration used for this evaluation. Moreover the angular acceptance of the α telescope is one order of magnitude smaller than the acceptance of the Be telescope.

In these plots the energy scale is arbitrary because the calibration has been done for the α particles and, as seen in section 3.3, the response of the scintillators is different for the different particle species. Since the counting statistic allows to use the Poisson distribution, the resolution of the NaI's scales as the square root of the measured energy (E). Therefore, the standard deviation of the smearing function can be expressed as:

$$\sigma_{smearing} = \sigma_C \frac{\sqrt{E}}{\sqrt{\mu_C}} \,. \tag{4.1}$$

Where σ_C and μ_C are respectively the standard deviation and the mean of the Gaussian at the elastic peak of C ions beam. This is an approximation, because it

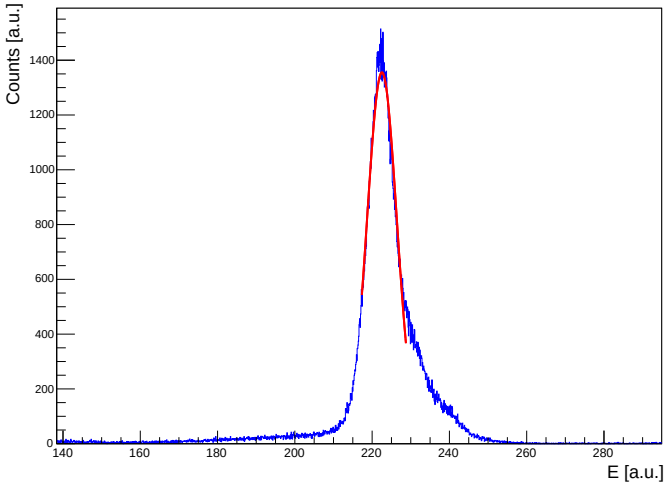

Figure 4.1. *Energy deposition in the NaI by the elastic scattered beam particles, in blue. The energy on the x axis is calibrated for the response of the NaI to a particles. In red the gaussian fit made to estimate the resolution of the detector.*

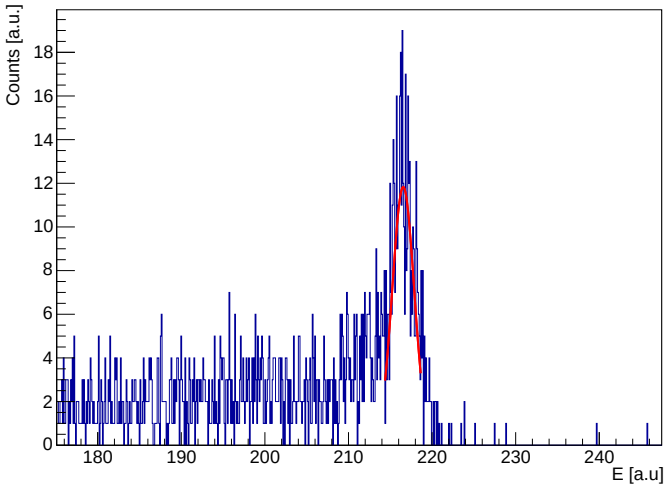

Figure 4.2. *Same as Figure 4.1 but for the NaI in the a telescope.*

does not take into account non linearities, but with only one experimental point per detector it is the best estimation we could do. To measure the parameters in the Equation 4.1, two fits have been done and the result are shown in Table 4.1.

Table 4.1. *Fit parameters of the two NaI's resolution.*

telescope	μ_C [MeV]	σ_C [MeV]
α	216.5 ± 0.8	1.3 ± 0.8
Be	222.5 ± 0.1	3.8 ± 0.1

The different resolution of the two NaI's is not surprising. In fact, the two crystals are identical but the two photomultipliers are different. Because of the limited space in the ^{8}Be telescope, the photomultiplier in it is custom made: it is shorter and has a poorer photostatistics than the other one.

4.2 Particle Identification

The two correlated α's in the ^{8}Be telescope and the α in the other telescope were identified through the $\Delta E/E$ method. It consists in binning the energy deposition in a thin detector (a *passing through* detector) as a function of the particle energy in bi-dimensional histograms, where the latter is measured with another detector thick enough to stop the particles. Hereinafter more details will be given describing separately the two telescopes. All the data presented in this section, both the MC and the experimental ones, relate to the carbon target with the α telescope placed at 16° because the selection criteria defined for the other targets and other orientation of the α telescope are the same.

4.3 Be telescope

As described in chapter 2, the ^{8}Be telescope is made of a thin silicon detector, the SSD, and a NaI. The signal is generated by two correlated α's resulting from the decay of ^{8}Be. The two correlated α's cross the SSD in two different strips and both reach the NaI. Let $\Delta E_\alpha(E)$ be the energy deposition of one α particle in the SSD as a function of the energy deposition (E) in the subsequent NaI. This function has been obtained using the FLUKA driver that simulates the energy loss. Since the binding energy of $^8\mathrm{Be}_{\mathrm{GS}}$ is just 92 keV, the phase space is small and the two α's coming from the $^8\mathrm{Be}_{\mathrm{GS}}$ decays have almost the same energy. In addition, the strips are read out separately, hence the signal energy deposition $\Delta E_{Be}(E)$ can be approximated as:

$$\Delta E_{Be}(E) \approx \Delta E_\alpha \left(\frac{E}{2} \right) . \tag{4.2}$$

Figure 4.3 shows the energy deposition in the SSD as a function of the one in the NaI, as provided by the MC simulation of the experiment. Conversely, figure 4.4 shows the energy deposition made only by the signal. In both figures the black line

is the expected energy deposition of the signal $\Delta E_{Be}(E)$. Considering their purpose, we will refer to these plots as *PID* plots.

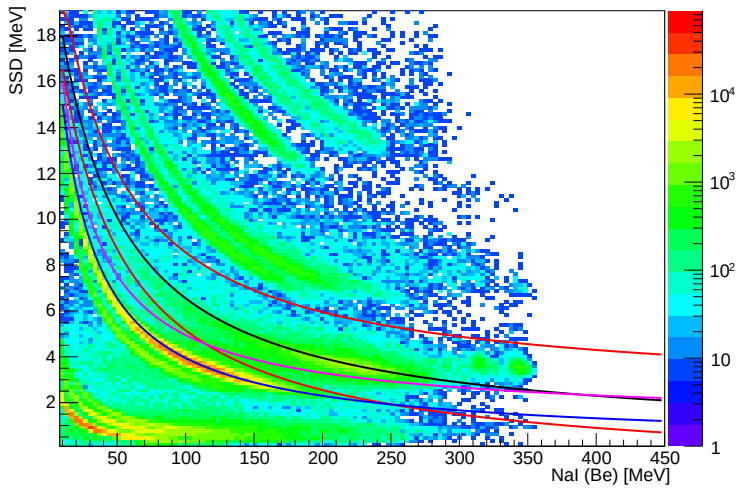

Figure 4.3. *Energy deposition in the SSD as a function of NaI. Data from the MC simulation. The black line is the expected energy deposition from two correlated α's, while the blue one is the expected energy deposition of a single α. The red lines delimit the selected region (for the low energy part, the lowest between the magenta and the red is chosen, where the magenta is the expected energy deposition of a single α +1 MeV).*

To isolate the signal in figure 4.3 a region has been defined to include all the signal. The lower cut is set at

$$E_{DSSSD} - \Delta E_{Be}(E = E_{NaI}) = -1.4\,\text{MeV}\ ,$$

while the higher one at

$$E_{DSSSD} - \Delta E_{Be}(E = E_{NaI}) = 2.0\,\text{MeV}$$

The selected region is represented in the plots 4.3 and 4.4 by the two red lines. To ensure the selection of all the signal, a less strict criterion has been chosen for the low energy region: the expected energy deposition of a single α increased by 1 MeV. The lower cut is then the smaller between $\Delta E_{Be}(E) - 1.4\,\text{MeV}$ and $\Delta E_{\alpha}(E) + 1.0\,\text{MeV}$. The value of 1 MeV has been chosen since the curve $\Delta E_{\alpha}(E) + 1.0$ delimits the region in figure 4.3 corresponding to the single α signal. It is represented by the magenta line in figures 4.3 and 4.4. The final selected region is shown in figure 4.5, on the top of the experimental data.

The histograms in the plots 4.3, 4.4 and 4.5 are filled with the data from all the strips since, after the calibration, the response of all of them is the same. The selection is applied on the data strip by strip and two strips matching the selection criteria are requested.

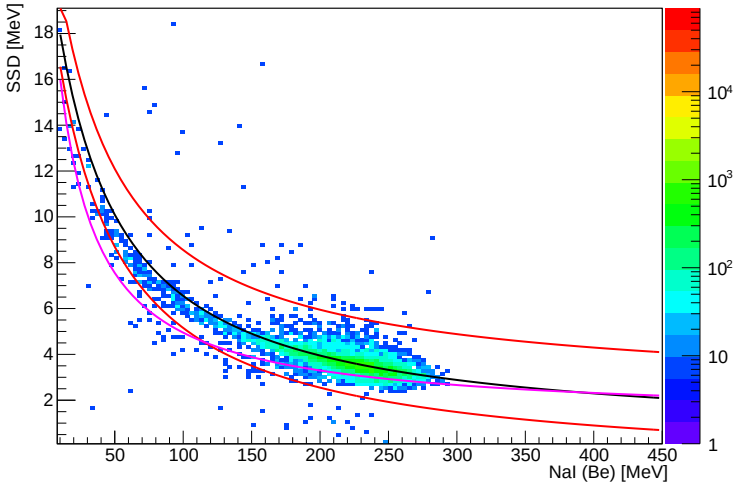

Figure 4.4. *As in figure 4.3, the plot shows the response of the SSD as a function of NaI, but here only the energy deposition due to the a's from ^{8}Be is taken into account. The color code is the same of figure 4.3.*

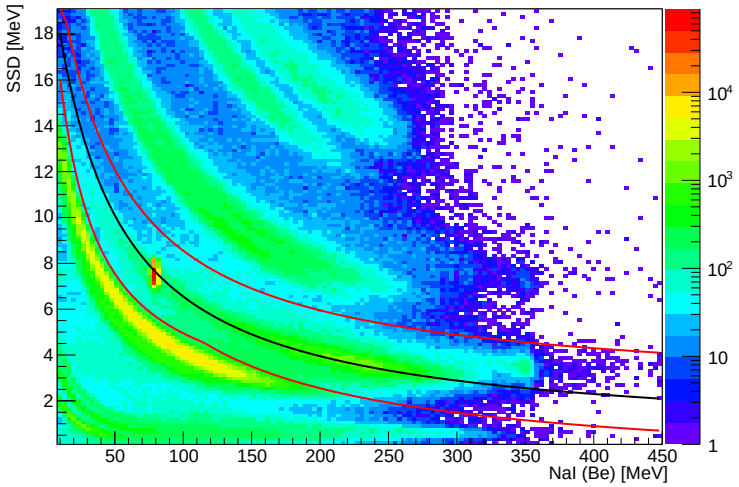

Figure 4.5. *This plot is the same of the figure 4.3 but obtained with experimental data. The black line is the expected energy deposition from two correlated a. The red line delimits the selected region.*

4.3.1 Selection of Be

The ^{8}Be can be interpreted as a resonance of the alpha-alpha system. It has a narrow (5.5 eV) ground state (0^{+}) with an half-life of $6.7 \cdot 10^{-17}$ sec and a very wide (1510 keV) excited state (2^{+}) with a nominal energy of 3.03 keV [Pro14]. The SSD detector was chosen to measure separately the energy of the two correlated α's produced in the decay of ^{8}Be, so the first selection criterion to identify the ^{8}Be requires that the outputs of two SSD strips fit in the region defined in the previous paragraph.

In order to reduce the background, a selection on the difference of energy deposited in the two selected strips has been added. In principle, using this variable the $^{8}\mathrm{Be}_{\mathrm{GS}}$ and the excited state of ^{8}Be could be partially discriminated. Figure 4.6 shows the distribution of the difference of energy deposition in the two strips obtained with experimental and MC data, the latter normalised by:

$$sf = \frac{C}{Z_C e}\sigma_{(C,C)}\frac{\rho_{\mathrm{C}} N_{Av}}{A_{\mathrm{C}} T}\frac{1}{N_{prim}30}10^{-27} \tag{4.3}$$

where C is the total beam current used in the experiment; Z_C is by the charge of the C ions; e the elementary charge; $\sigma_{(C,C)}$ is the cross section of Carbon-Carbon inelastic interaction; ρ_C the density of the Carbon target; A_C the atomic weight of Carbon; T the thickness of the target; N_{Av} the Avogadro's number; N_{prim} the number of primaries simulated and finally the factor 1/30 is coming from the biasing described in section 3.1. As seen in this plot, the distribution of the difference of energy deposition in the two strips is narrower for the ground state than for the excited state of the ^{8}Be.

It has been decided to keep all the states of the ^{8}Be, therefore the gate has been set to $\Delta E_{strips} = \pm 3$MeV.

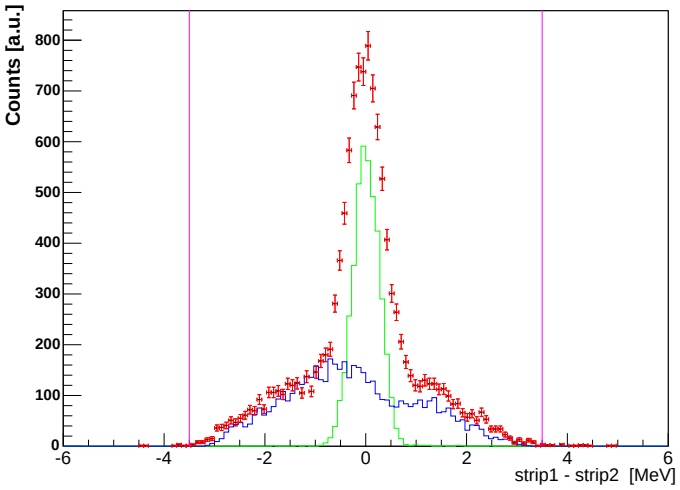

Figure 4.6. *Difference between the energy deposited in the two firing strips by the α coming from a $^{8}Be_{GS}$ (green) and the excited state of ^{8}Be (blue). In red the experimental data points and in magenta the cuts.*

4.4 α telescope

The same $\Delta E/E$ technique has been used for the α telescope. This telescope consists of three detectors. Therefore, the procedure is used twice. The first *PID* plot is made to identify the very low energy particles using $\Delta E1$ as a *passing through* and $\Delta E2$ as a *stopping* detector. While for higher energy α's, that pass also through the $\Delta E2$, the *PID* plot is made with the energy deposition in the $\Delta E2$ as a function of the response of the subsequent NaI.

Figure 4.7 shows the MC simulation of the first *PID* plot, while figure 4.8 shows the energy deposition in the two detectors from only the α's. In both figures, as for the ^{8}Be telescope, the black line is the average energy deposition.

Figure 4.9 depicts the cut superimposed to experimental data. Since the cut is kept loose enough to include all the signal in both, MC and experiment, another gate has been applied, and is described in the next section, to remove the contamination of the ^{3}He, that are in the region partially included by the lower cut.

Figure 4.10 shows the MC simulation for the second *PID* plot of the α telescope while figure 4.11 shows the signal. Also here the selection criterion includes the ^{3}He in addition to ^{4}He. Figure 4.11 shows the selected region on the experimental data. It seems that the quenching of the NaI in the experiment is higher than in the simulation. Indeed, to check the simulation of the stopping power of α particles in silicon, a comparison between FLUKA and the values published by the National Institute of Standards and Technology (NIST) [NIST] has been done (figure 4.13). As emerges from the figure, the stopping power calculated with FLUKA matches the data published by NIST, except for α's with a kinetic energy of about 0.5 MeV, an energy range which corresponds to the last 2 µm of the α range, and of no impact for the purpose of this simulation, as can also be appreciated from the agreement

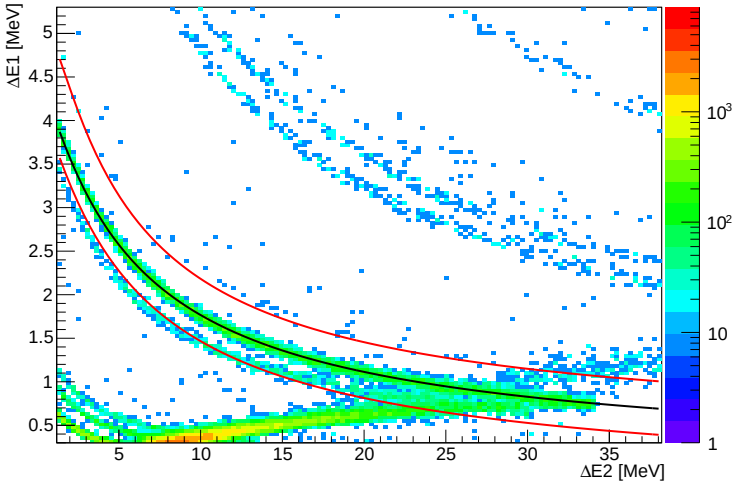

Figure 4.7. *Energy deposition in $\Delta E1$ as a function $\Delta E2$. Data from the MC simulation. The black line is the expected energy deposition from a. The red line delimits the selected region.*

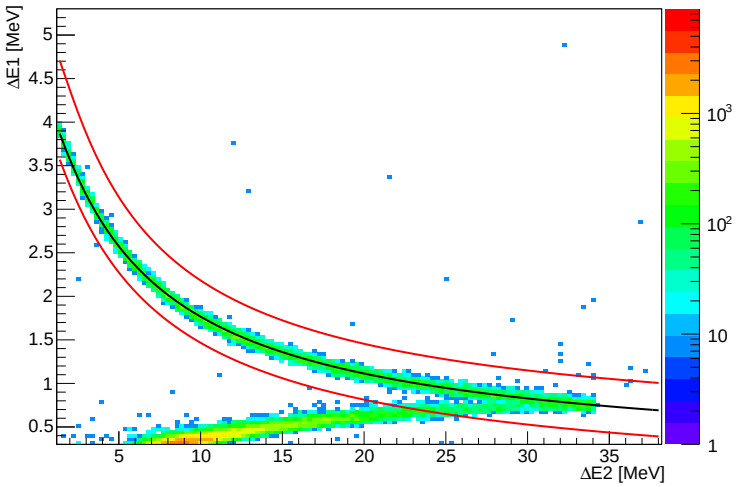

Figure 4.8. *As in figure 4.7 the plot shows the response of $\Delta E1$ as a function of $\Delta E2$ but here only the energy deposition due to the a's is taken into account. The color code is the same of figure 4.7.*

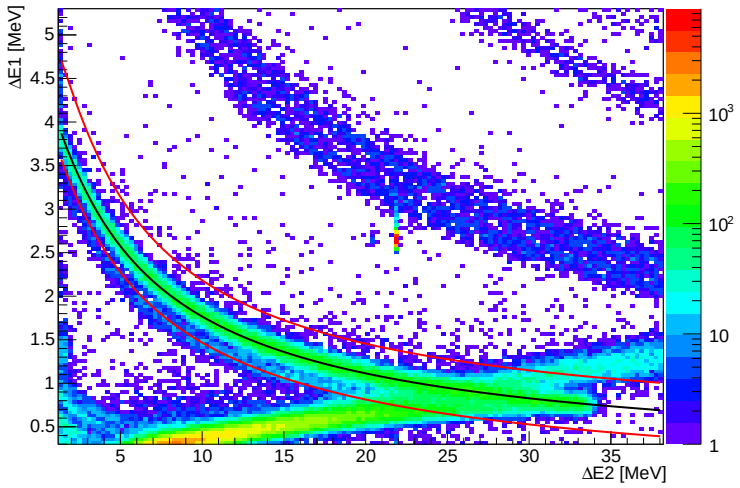

Figure 4.9. *This plot is the same of the figure 4.7 but obtained with experimental data. The color code is the same of figure 4.7.*

between Figure 4.7 and Figure 4.9.

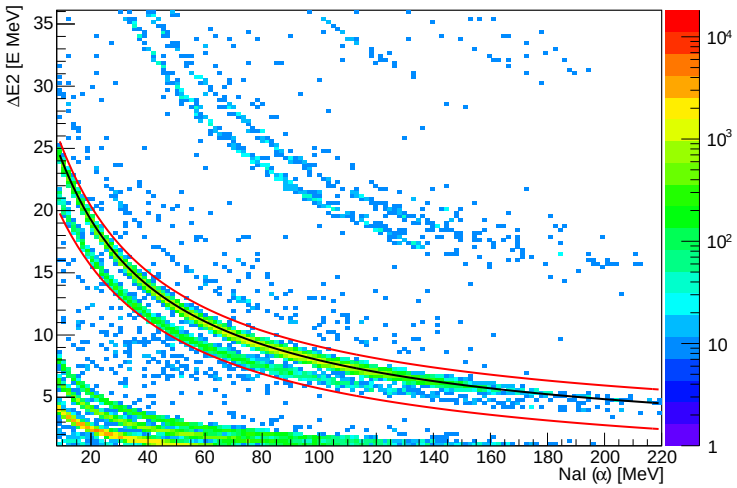

Figure 4.10. *Energy deposition in the the $\Delta E2$ as a function of the subsequent NaI. Data from the MC simulation. The black line is the expected energy deposition from a. The red line delimits the selected region.*

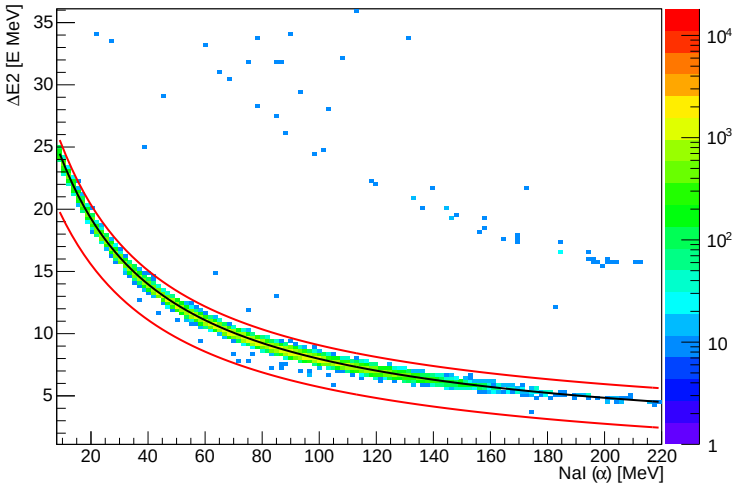

Figure 4.11. *As in figure 4.10 the plot shows the response of $\Delta E2$ as a function of the NaI but here only the energy deposition due to the a's is taken into account. The color code is the same of figure 4.10*

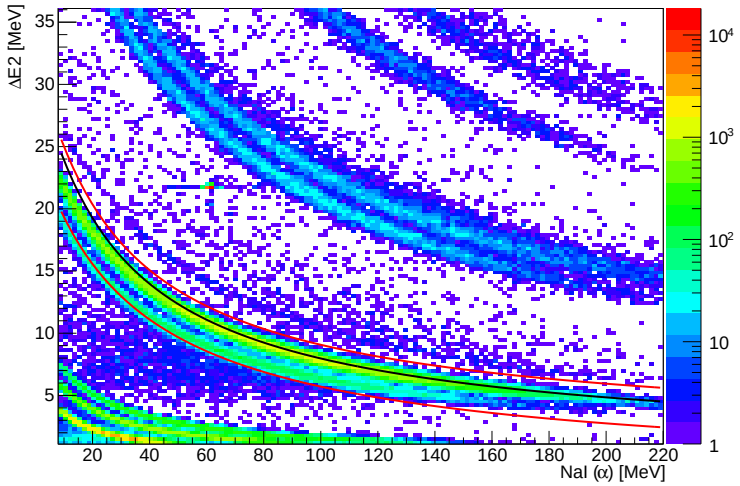

Figure 4.12. *This plot is the same of figure 4.10 but obtained with experimental data. The color code is the same of figure 4.10*

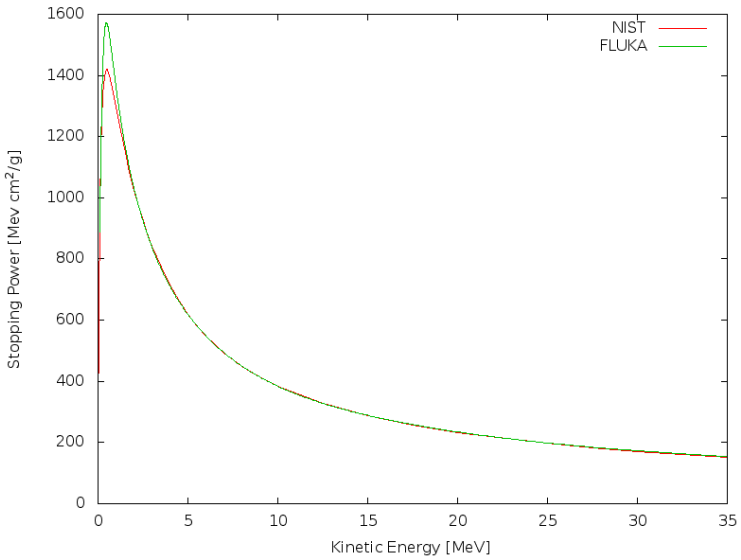

Figure 4.13. *Comparison of the stopping power for α in silicon between* FLUKA *and the data published by NIST [NIST].*

4.4.1 Selection of ^{4}He

As seen in the previous section, since the $\Delta E/E$ selection does not suffice to remove the contamination from ^{3}He in the α telescope, another selection criterion has been added and it is described in this section.

The range (R) in the continus slowing down approximation of a charged particle can be calculated integrating the total energy-loss (equation 1.3):

$$R = \int_{E_0}^{0} \left(\frac{dE}{dx}\right)^{-1} dE \tag{4.4}$$

where E_0 is the initial energy of the particle. The integral in Equation 4.4 can be split in to two terms:

$$\int_{E_0}^{0} \left(\frac{dE}{dx}\right)^{-1} dE = \int_{E_0}^{E'} \left(\frac{dE}{dx}\right)^{-1} dE + \int_{E'}^{0} \left(\frac{dE}{dx}\right)^{-1} dE \tag{4.5}$$

the first term on the right side is the thickness (ϵ) where the particle loses an energy $\Delta E = E_0 - E'$:

$$\epsilon = \int_{E_0}^{E'} \left(\frac{dE}{dx}\right)^{-1} dE\,, \tag{4.6}$$

i.e. it represents the *passing through* detector in the *PID* plot, while the second term in the equation 4.5 is the residual of the range of the particle in the stopping detector, where the particle loses the rest of its energy.

For a given particle and material the range R is function only of the energy:

$$R = f(E)\,, \tag{4.7}$$

therefore it is possible to write the equation 4.5 as [VGTC67]:

$$f(E_0) = \epsilon + f(E') \tag{4.8}$$

or:

$$\epsilon = f(\Delta E + E') - f(E')\,. \tag{4.9}$$

In a restricted domain of energies, up to about 1 GeV for α particles (figure 4.14), $f(E)$ can be approximated as:

$$f(E) \approx kE^n \tag{4.10}$$

where k is a parameter, function of the mass and the charge of the particle, and n is a constant. From equation 1.6 it is possible to see that dE/dx should be proportional to $1/\beta^2$, but as seen in figure 4.14, the energy-loss in the low energy region is better approximated by $1/\beta^{\frac{5}{3}}$ [PDG98]. The value $\frac{5}{3}$ is a phenomenological recipe and is due to the onset of the shell corrections. For velocities much smaller than the speed of light, the energy is proportional to β^2, so $dE/dx \propto 1/E^{\frac{5}{6}}$ from which $f(E) \propto E^{\frac{11}{6}}$, therefore $n \approx 1.8$. However, this value is obtained with many approximations and using the data of the range in silicon published on [NIST] it is possible to obtain a more accurate value from a fit (figure 4.15). The value obtained from the fit is: $n = 1.722 \pm 0.002$.

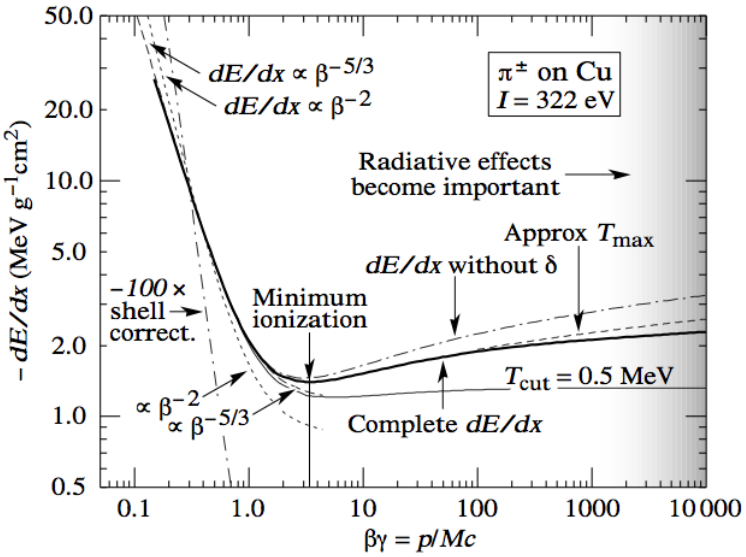

Figure 4.14. *Energy loss rate of pions in copper. In the low energy region the conventional approximation β^{-2} is compared with $\beta^{-\frac{5}{3}}$. Figure from [PDG98].*

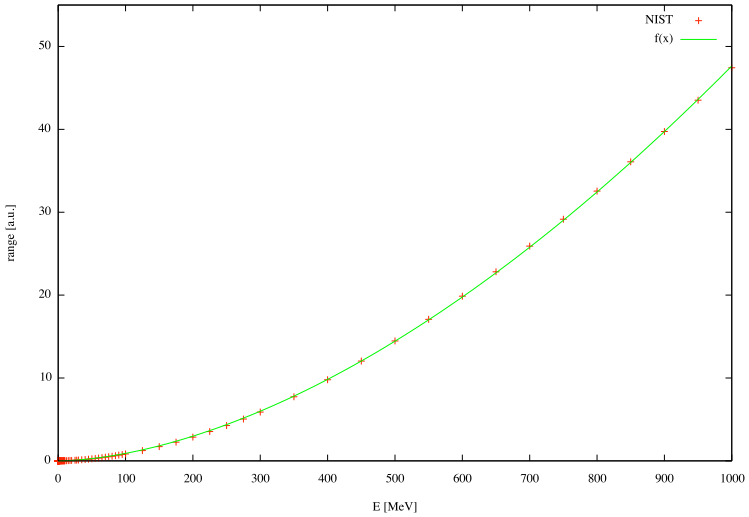

Figure 4.15. *Range in silicon of a particle in function of the initial energy. In red the data published on [NIST], in green the fit with a function E^n.*

Using the approximation 4.10, equation 4.9 can be rewritten as:

$$\frac{\epsilon}{k} = (\Delta E + E')^n - (E')^n \,. \tag{4.11}$$

Equation 4.11 is a function only of the characteristics of the particle and can be used to distinguish between different species. To do that it is convenient to define a "mass function" [LMG79] as:

$$m.f.(E', \Delta E) = \left[(E' + \Delta E)^n - (E')^n\right] \cdot M_s + M_0 \tag{4.12}$$

where M_s is a slope factor to increase the scale and M_0 an offset.

Plotting the *mass function* as a function of E', it is possible to distinguish between the different isotopes and particles. See as an example figure 4.16, where the mass function, obtained using $\Delta E2$ as a passing through and the subsequent NaI as stopping detector, as a function of the energy deposition in the latter is shown.

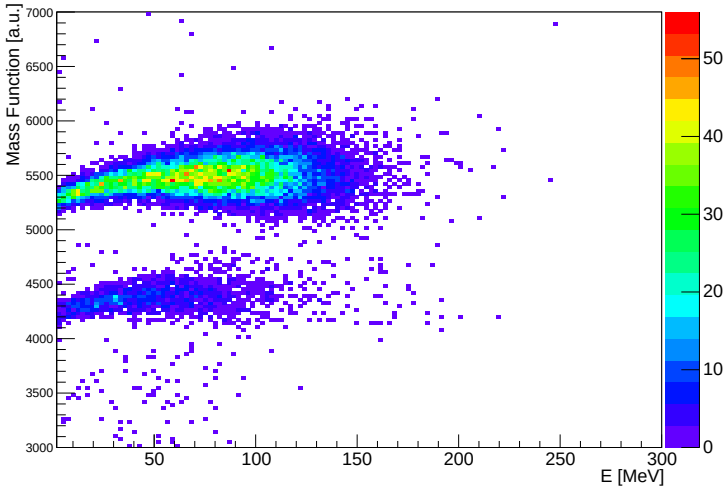

Figure 4.16. *Mass function as a function of E' obtained using $\Delta E2$ as passing through detector and the subsequent NaI as stopping detector. As is is possible to see in figure 4.16, the lower locus is due to the ^{3}He while the higher to ^{4}He. Plot made with MC data.*

To compare experimental and MC data and to set the gate, an histogram with the values of the *mass function* has been done and it is presented in figure 4.18, for the first couple of detectors, and in figure 4.17 for the second one. In other words these histograms are the projections on the y axes of the bi-dimensional plots similar to Figure 4.16

The MC fits well the trend of the data in the mass function made with $\Delta E2$ and the NaI (Figure 4.17). There is an asymmetry of the experimental data that is not matched by the MC. It could be due to the non perfect simulation of the quenching in the low energy region, as can be seen comparing Figure 4.16 and Figure 4.19. Indeed there are no experimental points in the low energy region that could let to refine the simulation of the nonlinearitiy of the response of the NaI to low energy α's.

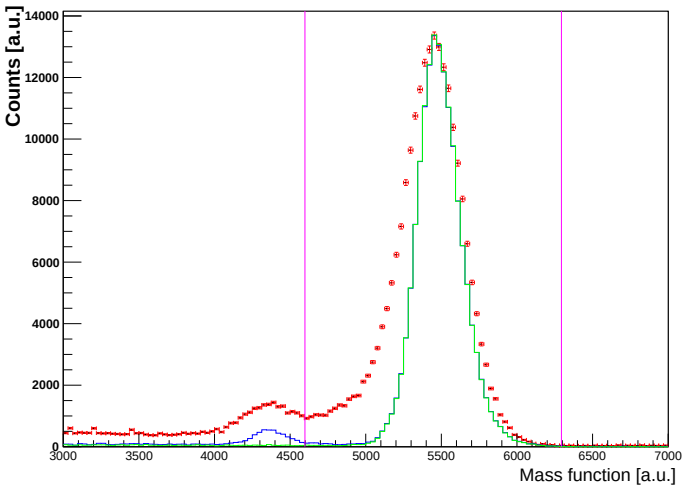

Figure 4.17. *Projection of the plot in figure 4.16. In red the experimental data points; in green the MC output for the a's; in blue the MC simulation of the ^{3}He; in magenta the cuts.*

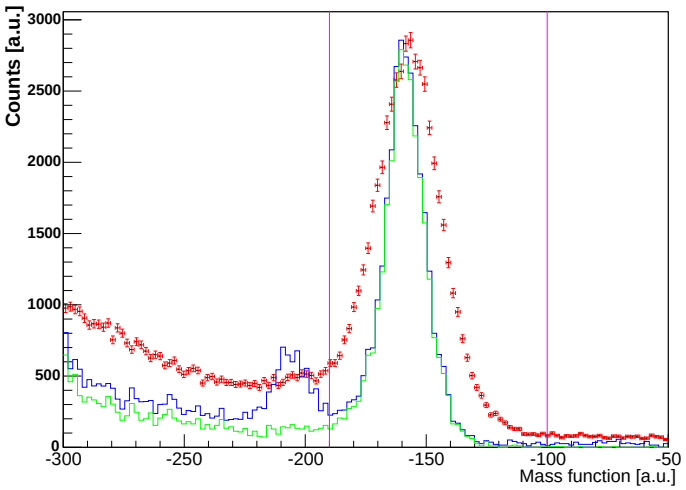

Figure 4.18. *Same as figure 4.17 but using $\Delta E1$ as passing through detector and $\Delta E2$ as stopping detector.*

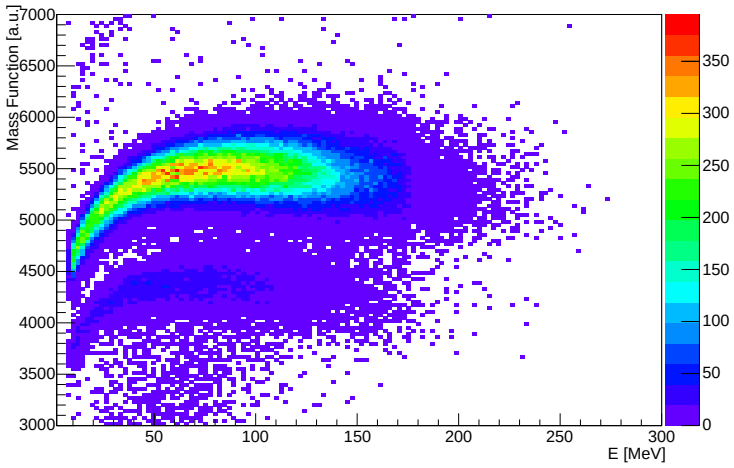

Figure 4.19. *Same as Figure 4.16 but made with experimental data.*

An example of the mass function computed with $\Delta E1$ as passing through detector and $\Delta E2$ as stopping detector is shown in Figure 4.18. The mass function calculated with experimental data has a larger distribution than the one calculated with MC data. This could be due to the poorer resolution of the $\Delta E1$. Unfortunately, it is not possible to select, in the available data, something with an energy deposition in the $\Delta E1$ narrow enough to estimate its resolution.

4.5 Identification of possible contamination in the target

In order to extract the cross-section of the quasi-elastic break up of ^{12}C to ^{8}Be and α, a two-dimensional energy spectra has been realised. Figure 4.20 shows the spectra with the kinetic energy measured in the ^{8}Be telescope as a function of the energy measured in the α telescope. This plot refers to experimental data on C target. The data exhibit a doubly peak structure in the high energy region. To better visualise this structure, and also to better identify the quasi-elastic peak, from now on the two-dimensional spectra will be displayed with the total energy as a function of the α energy. For instance, the same data of figure 4.20 are shown in figure 4.21, where the two peaks structure is even more evident. Those two peaks do not appear in the MC simulation, when only the C contribution is taken into account (figure 4.22). Another surprising feature shows up in the spectra of the α fragments, figure 4.27. Indeed the data show an excess in the high energy region, as if the α fragments speed were greater than the original speed of the ^{12}C projectile.

For these reasons, a contamination of Hydrogen has been supposed. To investigate this hypothesis and emphasise the contribution of H, a dedicated experimental run with a polyethylene $(CH_2)_n$ target has been done. The experimental spectrum is shown in figure 4.23.

Simulating selectively several intermediate states of the interaction between C

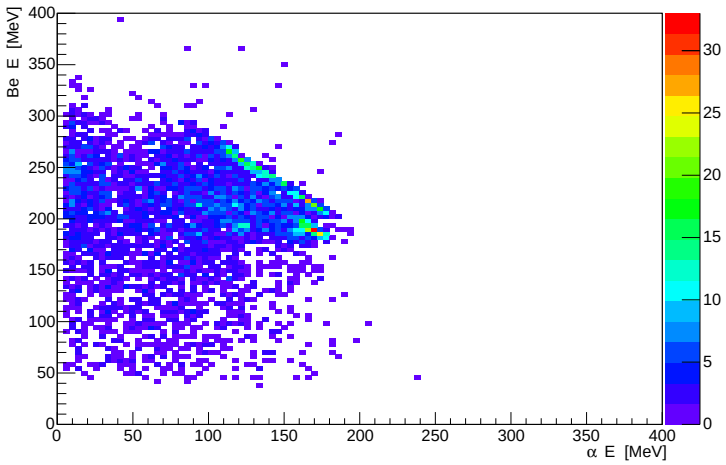

Figure 4.20. *Energy spectrum obtained from experimental data with the energy measured in the ^{8}Be telescope as a function of the energy measured in the a telescope. Target in C.*

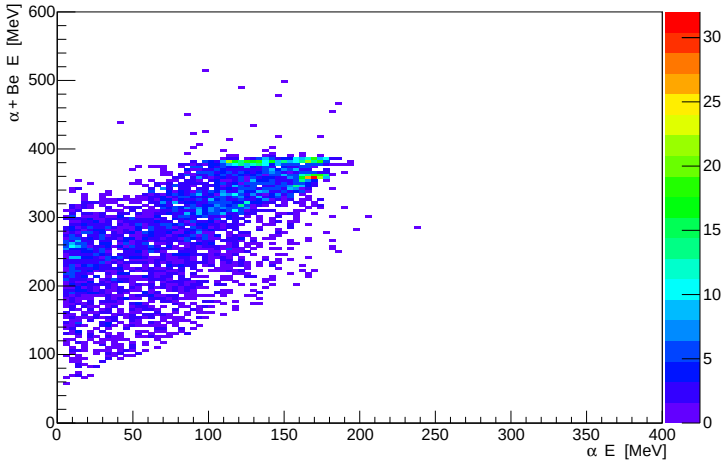

Figure 4.21. *Same as Figure 4.20 but with the sum of the energy measured in the two telescopes as a function of the energy measured in the a one.*

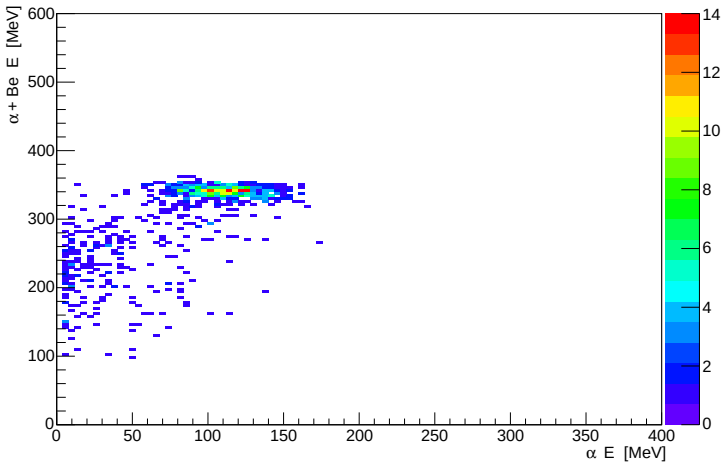

Figure 4.22. *Same plot as in figure 4.21 but obtained with MC data.*

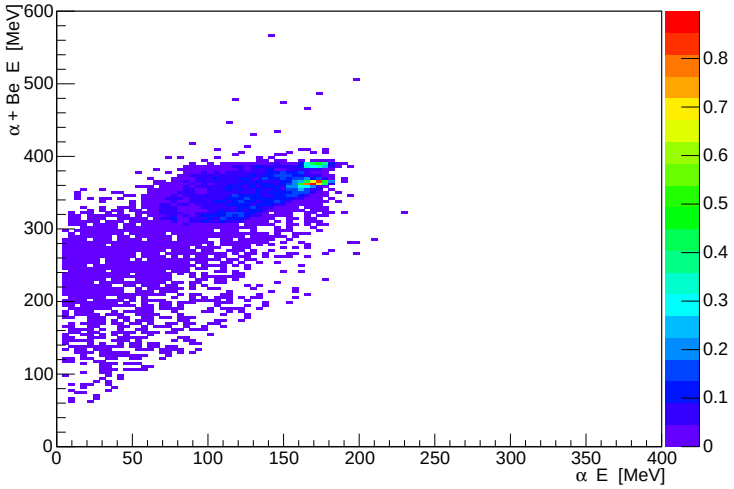

Figure 4.23. *Same plot as in figure 4.21 but obtained with experimental data with a $(CH_2)_n$ target.*

and H, it comes out that the experimental data can be explained by the reaction channel in witch the ^{12}C projectile, interacting with the H, produces a $^{9}B_{gs}$ and a correlated α. This reaction, in the frame where the C is at rest, is a (p,α) reaction, in which the proton is impinging on the C and an α particle is emitted. More details on this reaction will be given in section 5.1. The $^{9}B_{gs}$ subsequently decays in $^{8}Be_{GS}$ plus a proton. The double peak structure is due to the fact that sometimes the proton is detected and enters in the selection. The high energy peak is produced when the proton goes in and its energy is added to the energy of the two α's. The lower peak is produced when the proton is not detected. The events from this process that fit the geometry of the experiment and the selection criteria are the ones in which the α is emitted, in the projectile rest frame, at large angles and this explains also the increased energy of this fragment.

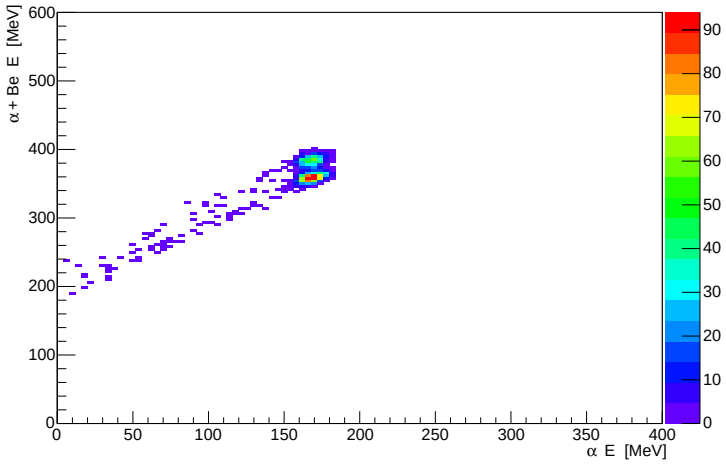

Figure 4.24. *Energy spectrum of the production of ^{9}B and α in the interaction of a C ion with H. Histogram made with the total energy measured as a function of the energy deposited in the a telescope. MC simulation.*

This reaction was already present in FLUKA, but just as one of the possible channels for the Fermi break-up and not as a pre-equilibrium reaction. A direct mechanism has be added (it is described in the section 5.1) and the results are shown in Figures 4.24, 4.25, 4.26 and 4.27. Figure 4.24 shows the contribution to the bi-dimensional spectrum of the events with a production of $^{9}B_{gs}$, it is possible to see the two sharp peaks structure. Figure 4.25 shows the FLUKA result for the $(CH_2)_n$ target after the implementation of the (p,α) reaction in the pre-equilibrium stage. The contribution of the $^{9}B_{gs}$ production is even more evident in Figures 4.26 and 4.27, that are the projections on the two axis of the bi-dimensional spectra in Figurs4.25 and 4.23.

As said in chapter 3, the MC simulate the direct interaction between the beam and the target atoms, therefore the simulation of the $(CH_2)_n$ target has been done separately for the H and C contribution and summed up, and confronted with

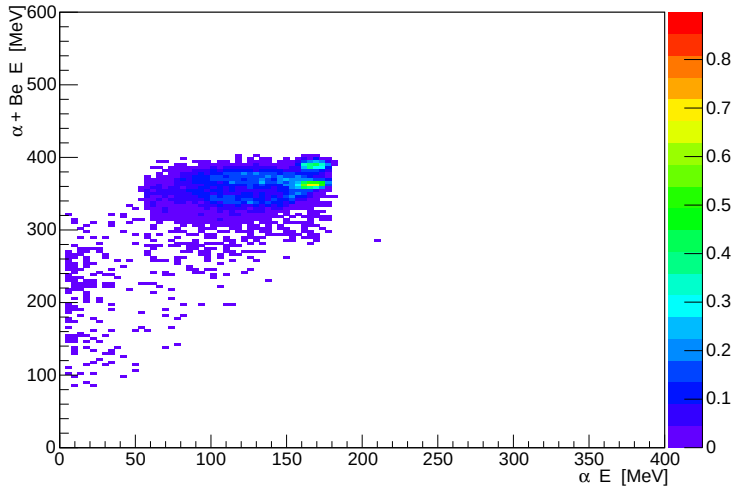

Figure 4.25. *Same as Figure 4.23 but with MC data.*

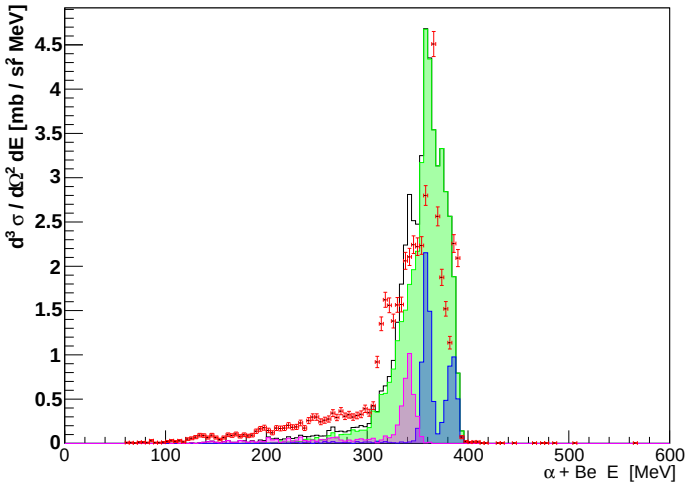

Figure 4.26. *Projection on the total energy axis of the plot in Figure 4.25. In red the experimental data; in black the total MC spectrum, in green the part due to the H and in blue its part that produced ^{9}B as intermediate state. In magenta the part due to C.*

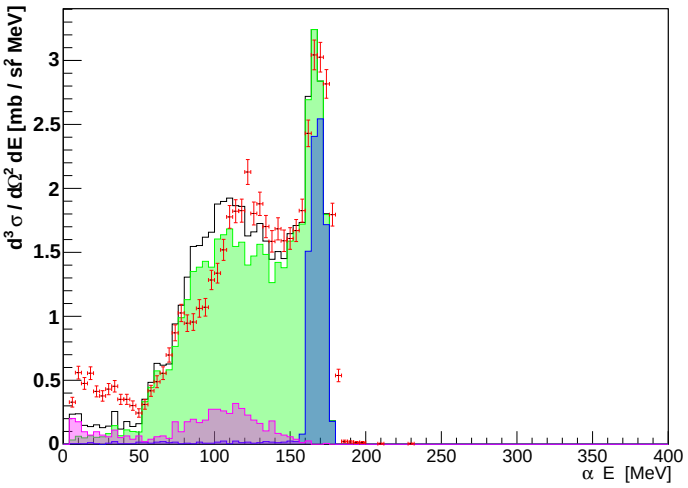

Figure 4.27. *Same as Figure 4.26 but for the a telescope axis.*

experimental data, multiplying each output by a scaling factor:

$$sf_{\mathrm{H}} = \frac{\sigma_{(\mathrm{C,H})}}{N_{prim}(\mathrm{H})}\frac{1}{30}2 \tag{4.13}$$

$$sf_{\mathrm{C}} = \frac{\sigma_{(\mathrm{C,H})}}{N_{prim}(\mathrm{C})}\frac{1}{30} \tag{4.14}$$

where N_{prim} is the number of primaries simulated in each simulation, σ_{H} and σ_{C} are the total inelastic cross sections of C on H and C atoms, the factor $\frac{1}{30}$ is due to the biasing introduced by the rotation of the events (cfr. section 3.1) and the factor 2 in Equation 4.13 is due to the stoichiometric ratio.

4.6 Evaluation of the Hydrogen contamination

As seen in the previous section, the hypothesis of a H contamination in the targets with the production of ^{9}B explains the double peak structure and the excess of high energy α's. However the amount of H in each target is unknown, with the exception of the $(CH_2)_n$ target. In order to evaluate this amount and to verify the angular distribution of the ^{9}B production, the selection criteria have been modified to insulate the events in which ^{9}B has been produced. Three firing strips have been requested. Two of these strips have to fit in the selection criteria described in section 4.3, to identify the two α's; the third one has to measure an energy deposition smaller than 1.5 MeV, the energy deposition expected from the Proton emitted in the ^{9}B decay in Proton and ^{8}Be. In this way only the events where the Proton and the two α's coming from the decay of a $^{9}B_{gs}$ hit the SSD in three different strips are selected.

4.6.1 Angular distribution of the Boron production

Figure 4.28 shows the cross section of the reaction $^{12}\mathrm{C} + \mathrm{p} \longrightarrow {}^{9}\mathrm{B} + \alpha$ in the laboratory frame when the ^{9}B is emitted in the angular acceptance of the Be telescope as a function of the angle of emission of the α fragment.

This cross section increases with the angle of emission of the α fragment and suddenly drops after 22°. This characteristic is due to the Lorentz transformation from the Carbon rest frame and the laboratory frame. The cross section drops after 22° because this is the limit angle, as will be discussed in subsection 5.1.1.

There is a good agreement between MC and experimental data, especially at 16° where the statistic is higher. For the other angles the MC seems overestimate the production and the resolution of the Be telescope seems narrower, reflecting in a narrower peak in the total energy. Figure 4.28 shows the cross section calculated with FLUKA of the $^{12}\mathrm{C} + \mathrm{p} \longrightarrow {}^{9}\mathrm{B} + \alpha$ reaction with the ^{9}B emitted in the range $9° \pm 3°$, the acceptance of the Be telescope, as a function of the emission angle of the α.

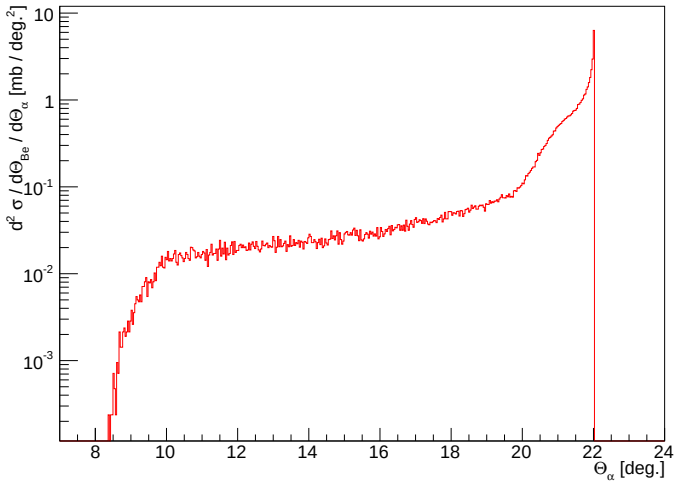

Figure 4.28. *Cross section of the $^{12}C + p \longrightarrow {}^{9}B + \alpha$ reaction with the ^{9}B emitted in the range $9° \pm 3°$ as a function of the emission angle of the α.*

Figures 4.29 to 4.33 show the total energy deposited and the energy measured in the α telescope for its different positions taken with the $(CH_2)_n$ target. As it is possible to see from the MC histograms in these plots, the contribution from the C in the target is almost completely rejected from the three firing strips requirement and practically only the events with a ^{9}B as intermediate state are selected.

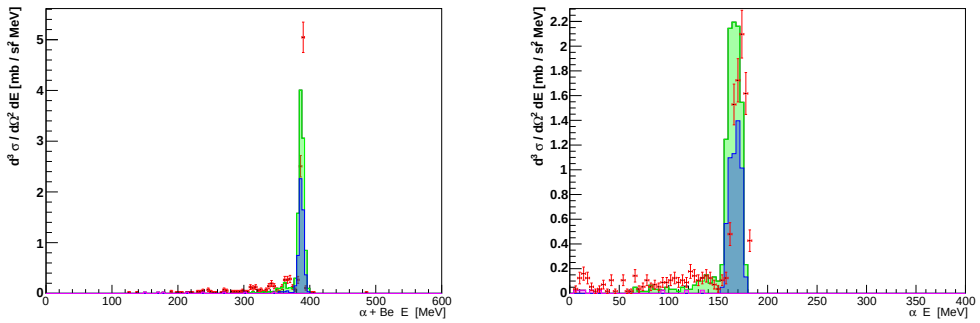

(a) (b)

Figure 4.29. *(a) Energy deposited in the two telescopes selecting events with 3 firing strips and using a $(CH_2)_n$ target and with the a telescope at 16°. In red the experimental data, in green the H contribution and in blue the events on H that produced a ^9B. (b) Same as (a) but for the a telescope. The contribution from the C is in magenta and it is visible only in the low energy region of this plot.*

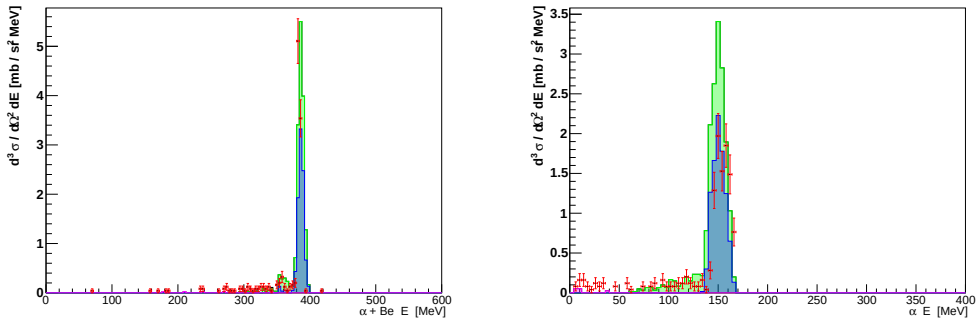

(a) (b)

Figure 4.30. *Same as 4.29 but with the a telescope placed at 18°.*

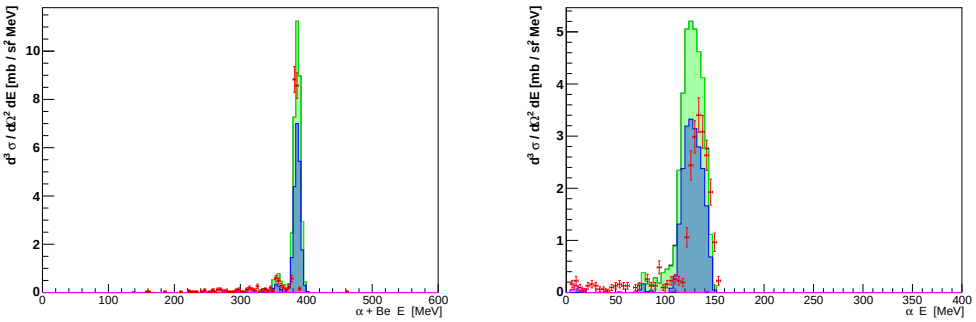

(a) (b)

Figure 4.31. *Same as 4.29 but with the a telescope placed at* 20°.

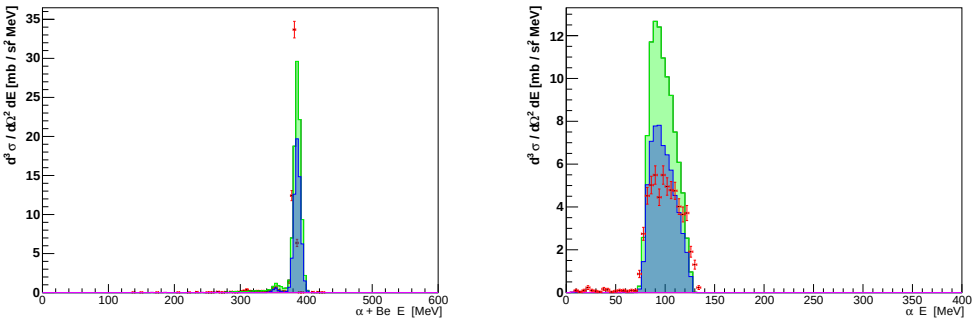

(a) (b)

Figure 4.32. *Same as 4.29 but with the a telescope placed at* 22°.

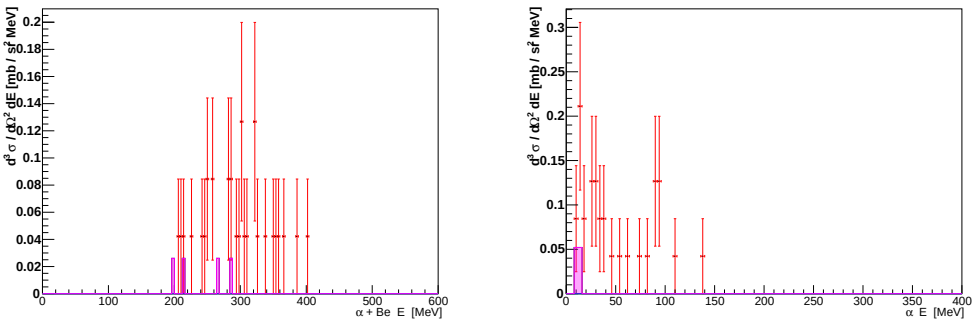

(a) (b)

Figure 4.33. *Same as 4.29 but with the a telescope placed at* 24°.

4.6.2 Evaluation of the H contamination in the targets

As seen in the previous section, the C contribution in the data related to the $(CH_2)_n$ target completely disappears with the selection criteria described in it. This means that it is possible to select only the H contribution in the data taken with the other targets. Comparing the $(CH_2)_n$ experimental data with the experimental data taken with each other targets, it is possible to estimate the amount of H that contaminates each target. Therefore, for every target and every position of the α telescope, the data have been compared with the data relative to $(CH_2)_n$ target. The contamination of H has been calculated imposing the same integral for the two histograms. Figures 4.34 show the data relative to the Au target. Figures 4.36 are the same for the Nb target and 4.35 for the C target. For Au, the data have not been acquired with the α telescope placed at 22°, while for Nb, unfortunately, the data relative to the α placed from 18° to 22° have been corrupted (probably during the first step of the conversion of the data files).

The contaminations calculated for each target with the α telescope placed in each position are summarised in Table 4.2 and shown in Figure 4.37. For Au and C targets, a weighted average has been calculated. They are indicated by the green line in Figure 4.37 and summarised in Table 4.3.

Table 4.2. *Estimated H contamination for each run matching the aerea of each histograms with the corresponding one taken with $(CH_2)_n$ target.*

Target	angle [deg.]	contamination [µg/cm^2]
Au	16	2.1 ± 0.2
Au	18	2.4 ± 0.3
Au	20	0.6 ± 0.1
Nb	16	3.8 ± 0.4
C	16	79 ± 5
C	18	170 ± 12
C	20	18 ± 2
C	22	17 ± 2

Table 4.3. *Average H contamination for Au and C targets.*

Target	contamination [µg/cm^2]
Au	1.1 ± 0.5
C	22 ± 1

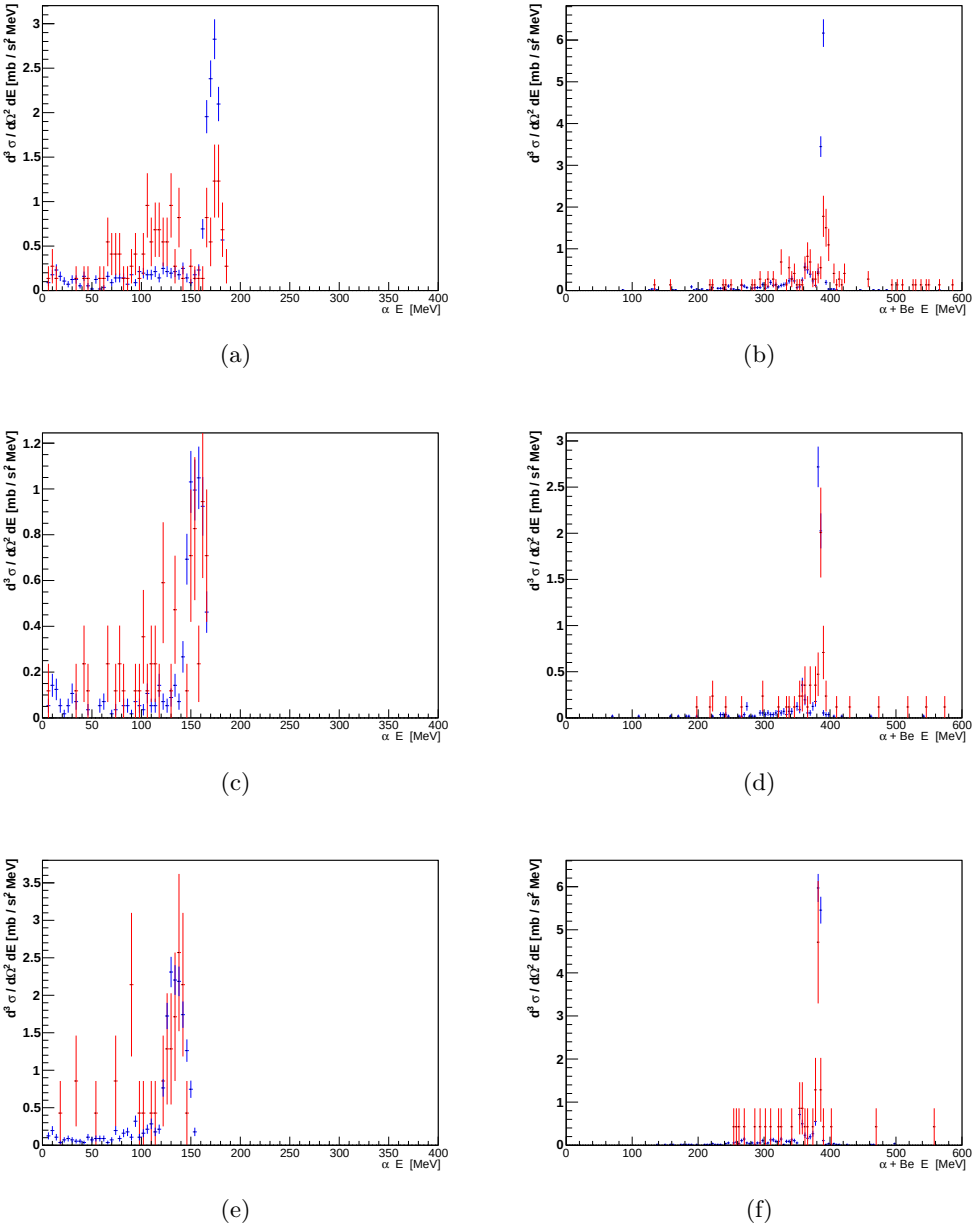

Figure 4.34. *Selection with three firing strips for Gold (in red) and $(CH_2)_n$ (in blue) targets. It is assumed that only the H in both the targets contributes to these histograms. The contaminations assumed for each angle are outlined in Table 4.2. The left panels show the energy deposition in the a telescope, while the right ones the total energy deposition. (a) and (b) relate to the data acquired with the a telescope placed at* 16°*; (c) and (d)* 18°*; (e) and (f)* 20°*.*

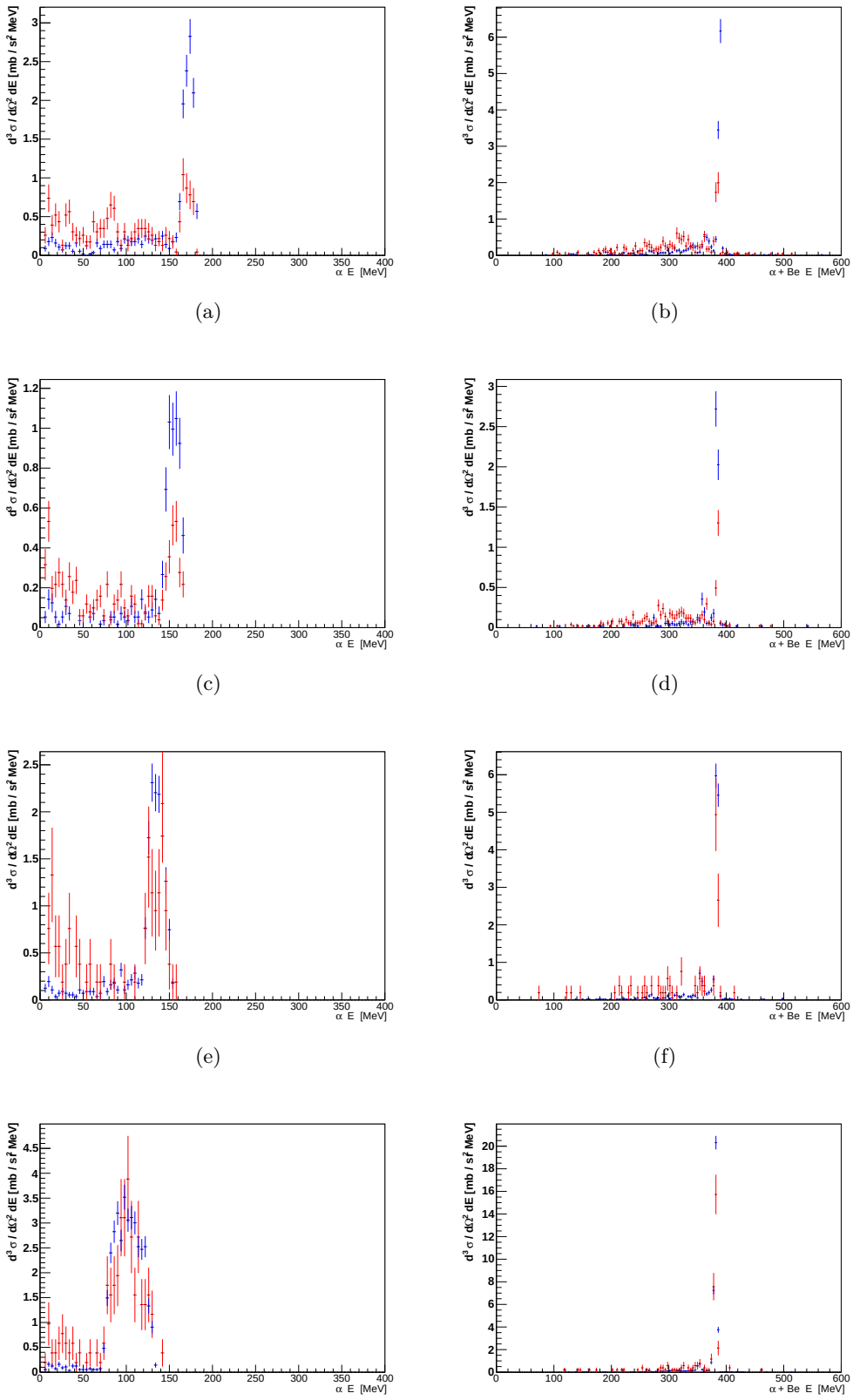

Figure 4.35. *Same as Figure 4.34 but the red is the data relative to C target. (a) and (b) relate to the data acquired with the a telescope placed at* 16°*; (c) and (d)* 18°*; (e) and (f)* 20°*; (g) and (h)* 22°

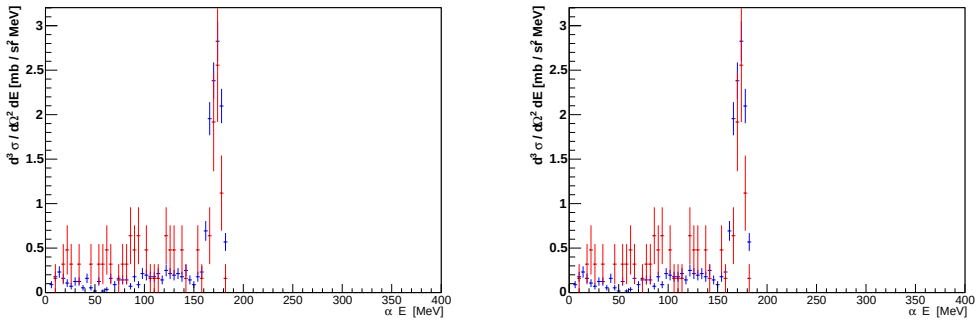

(a) (b)

Figure 4.36. *Same as Figure 4.34 but the red histogram relates to the data taken with Nb target. The only data set available for Nb are with the a telescope placed at* 16° *and* 24°*, here is shown only the first one because in the latter the contamination of H with* ^{9}B *does not appear, as shown in the previous section.*

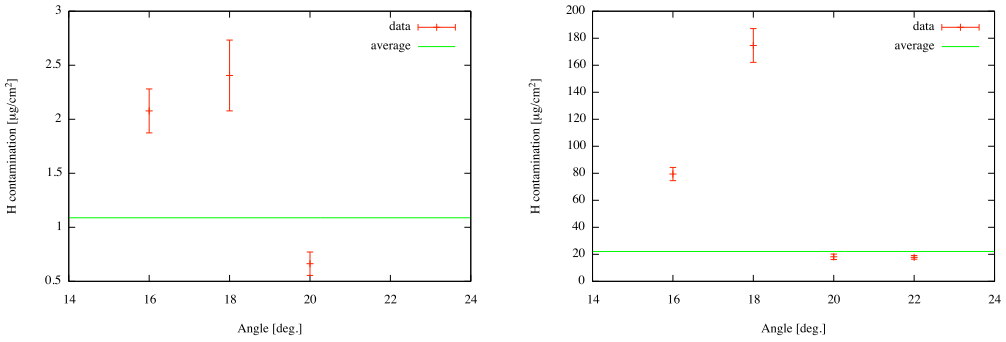

(a) (b)

Figure 4.37. *H contamination in Au target (left panel) and C target (right panel) as a function of the position of the a telescope, in red. In green the weighted average.*

Chapter 5

Monte Carlo implementation

This chapter describe of the models implemented in FLUKA to simulate the interactions relevant to simulate the experiment. We will firstly go in the detail of the (p,α) reaction hypothesised to understand the double peak structure described in section 4.5 and then we will describe the implementation of such interaction as a pre-equilibrium emission of the α, because this process was already implemented in FLUKA but only as one of the Fermi break-up possible channels. The second section describes the implementation of the quadrupole electromagnetic interaction, that has been done because it could simulate the quasi-elastic break-up of C ions.

5.1 Proton-alpha reactions in nuclei

A (p, α) reaction is an interaction where a proton collide with a nucleus and an α particle is emitted:

$$p + x \rightarrow a + x' \tag{5.1}$$

In the case in exam we have a ^{12}C ion impinging on a H target and an α particle emitted in the laboratory frame with an angle θ fixed, defined by the position of the α telescope.

$$^{12}\mathrm{C} + \mathrm{H} \rightarrow {}^{4}\mathrm{He} + {}^{9}\mathrm{B}_{\mathrm{GS}} \tag{5.2}$$

In the laboratory frame the invariant mass $\sqrt{s}$ is:

$$s = M_{\mathrm{C}}^2 + M_{\mathrm{H}}^2 + 2E_{\mathrm{C}}M_{\mathrm{H}} \tag{5.3}$$

while in the center of mass frame (CM) it is:

$$s = (E^{\star}_{\mathrm{He}} + E^{\star}_{\mathrm{B}})^2 \tag{5.4}$$

from which:

$$E^{\star}_{\mathrm{B}} = \sqrt{s} - E^{\star}_{\mathrm{He}}\,. \tag{5.5}$$

Equating the relation between energy, mass and momentum, namely:

$$E^{\star}_{\mathrm{B}} = \sqrt{{p^{\star}_{\mathrm{B}}}^2 + M_{\mathrm{B}}^2}\,, \tag{5.6}$$

to Equation 5.5, it is possible to obtain:

$${p^{\star}_{\mathrm{B}}}^2 + M_{\mathrm{B}}^2 = s + {E^{\star}_{\mathrm{He}}}^2 - 2\sqrt{s}E^{\star}_{\mathrm{He}} \tag{5.7}$$

and finally the energy of the α fragment in the CM frame:

$$E^{\star}_{\mathrm{He}} = \frac{s + M^2_{\mathrm{He}} - M^2_{\mathrm{B}}}{2\sqrt{s}}\,. \tag{5.8}$$

To calculate the energy of the other fragment, $E^{\star}_{\mathrm{B}}$, it is possible to use the relation 5.5.

To impose the angle of emission of one fragment in the laboratory frame it is simpler to calculate the transformation from this frame to the CM:

$$E^{\star}_{\mathrm{He}} = \gamma\left[E_{\mathrm{He}} - \beta p_{\mathrm{He}}\cos(\theta)\right] \tag{5.9}$$

which is equivalent to:

$$\gamma E_{\mathrm{He}} = E^{\star}_{\mathrm{He}} + \eta p_{\mathrm{He}}\cos(\theta) \tag{5.10}$$

where $\eta = \beta\gamma$. Substituting in 5.10 the energy of the α in the laboratory frame:

$$E_{\mathrm{He}} = \sqrt{{p_{\mathrm{He}}}^2 + M^2_{\mathrm{He}}} \tag{5.11}$$

it is possible to obtain:

$$\left[E^{\star}_{\mathrm{He}} + \eta p_{\mathrm{He}}\cos(\theta)\right]^2 = \gamma^2\left({p_{\mathrm{He}}}^2 + M^2_{\mathrm{He}}\right) \tag{5.12}$$

and carrying out the square:

$${E^{\star}_{\mathrm{He}}}^2 + \eta^2 p^2_{\mathrm{He}}\cos^2(\theta) + 2\eta E^{\star}_{\mathrm{He}} p_{\mathrm{He}}\cos(\theta) = \gamma^2 p^2_{\mathrm{He}} + \gamma^2 M^2_{\mathrm{He}} \tag{5.13}$$

from which, using the equivalence $\gamma^2 - \eta^2 = 1$ and rearranging the terms, it is possible to write:

$$\left[1 + \eta^2\sin^2(\theta)\right] p^2_{\mathrm{He}} - 2\left[\eta E^{\star}_{\mathrm{He}}\cos(\theta)\right] p_{\mathrm{He}} + \left[\eta^2 M^2_{\mathrm{He}} - {p^{\star}_{\mathrm{He}}}^2\right] = 0 \tag{5.14}$$

Solving the equation 5.14 for p_{He}:

$$p_{\mathrm{He}} = \frac{\eta E^{\star}_{\mathrm{He}}\cos(\theta) \pm \sqrt{\left[\eta E^{\star}_{\mathrm{He}}\cos(\theta)\right]^2 - \left[1 + \eta^2\sin^2(\theta)\right]\cdot\left[\eta^2 M^2_{\mathrm{He}} - {p^{\star}_{\mathrm{He}}}^2\right]}}{1 + \eta^2\sin^2(\theta)}\,. \tag{5.15}$$

Equation 5.15 has two possible solutions for the argument of the square root greater than zero, as appear also in Figure 5.1(a), where is shown the energy of the α in function of its emission angle, both in the laboratory frame. Nonetheless, only one of the two possible solutions matches the acceptance of the detector: in fact the angle of emission of the other fragment - the ^{9}B - has to be in the acceptance of the ^{8}Be telescope. As emerges in 5.1(d), where the angle of emission of ^{9}B as a function of the one of the α is shown, only one of the two solutions respects this requirement. Furthermore, the plot shows that for the α angle of emission between 16° and the largest kinematically possible one, the ^{9}B angle is always in the range $8^\circ \div 10^\circ$, the acceptance of the ^{8}Be telescope. When the argument of the square root in Equation 5.15 is zero, the two solutions coincides and this defines the maximum

emission angle. Going back to 5.1(c), this plot highlights also the energy dependence of the α as a function of the angle in the laboratory frame, reflecting the feature of the experiment. Figure 5.1(b) shows the energy of the ^{9}B fragment again as a function of the emission angle of the α, from a comparison of this plot and the one in Figure 5.1(a) it is possible to understand why in the experimental data the α seems to subtract energy to the other fragments. Finally, in Figure 5.1(c) is shown the α angle in the C rest frame as a function of the α angle in the laboratory frame, and from this plot emerges that the detected α's are the those emitted with at large angle in the C rest frame.

5.1.1 Angular kinematics

The angular kinematics of the α's emitted in the (p,α) reaction can be calculated from geometrical considerations: in the CM frame the spectrum of the possible moduli of the momenta of the α particles, $p^\star$, is in a diagram $p_x - p_z$ a circle of radius $p^\star$ where the angle in the plane it is the diffusion angle $\theta^\star$:

$$\frac{p_x^{\star 2}}{p^{\star 2}} + \frac{p_z^{\star 2}}{p^{\star 2}} = 1 \tag{5.16}$$

In a generic reference frame boosted along the Z axis, and then also in the laboratory frame, the components of the momentum of one of the two particles is:

$$p_x = p_x^\star \tag{5.17}$$
$$p_z = \gamma\,(p_z^\star + \beta E^\star) \tag{5.18}$$

where β is the speed of the CM frame in the other reference frame, and $\gamma = (1-\beta^2)^{-\frac{1}{2}}$. Using the equations 5.17 in the equation 5.16 it is possible to obtain:

$$\frac{{p_x}^2}{p^{\star 2}} + \frac{(p_z - \beta\gamma E^\star)^2}{\gamma^2 p^{\star 2}} = 1 \tag{5.19}$$

which is the equation of an ellipse centred in $p_z = \beta\gamma E^\star$. From this equation it is also possible to see the reason of the two possible solutions, indeed, for a given θ in the range $0 \div \theta_{max}$ there are two intersections between the ellipse and a straight line starting in the origin with an angle θ respect to the Z axis. If $\theta = \theta_{max}$ the line is tangent to the ellipse, and the two solutions coincide, while for θ above θ_{max} the line does not intersect the ellipse anymore and there are no possible solutions.

To find θ_{max} it is possible to write the relation between the angle in the laboratory frame and the angle of emission in the CM frame:

$$\tan(\theta) = \frac{p_x}{p_z} = \frac{p_x^\star}{\gamma(p_z^\star + \beta E^\star)} = \frac{\sin(\theta^\star)}{\gamma\left[\cos(\theta^\star) + \beta\frac{E^\star}{p^\star}\right]} \tag{5.20}$$

since $\tan(\theta)$ is a monotone function of θ, the maximum of the latter is also a maximum in the first one, hence taking derivative of the Equation 5.20:

$$\frac{d\tan(\theta)}{d\theta^\star} = \frac{\beta\frac{E^\star}{p^\star}\cos(\theta^\star) + 1}{\gamma[\cos(\theta^\star) + \beta\frac{E^\star}{p^\star}]^2} \tag{5.21}$$

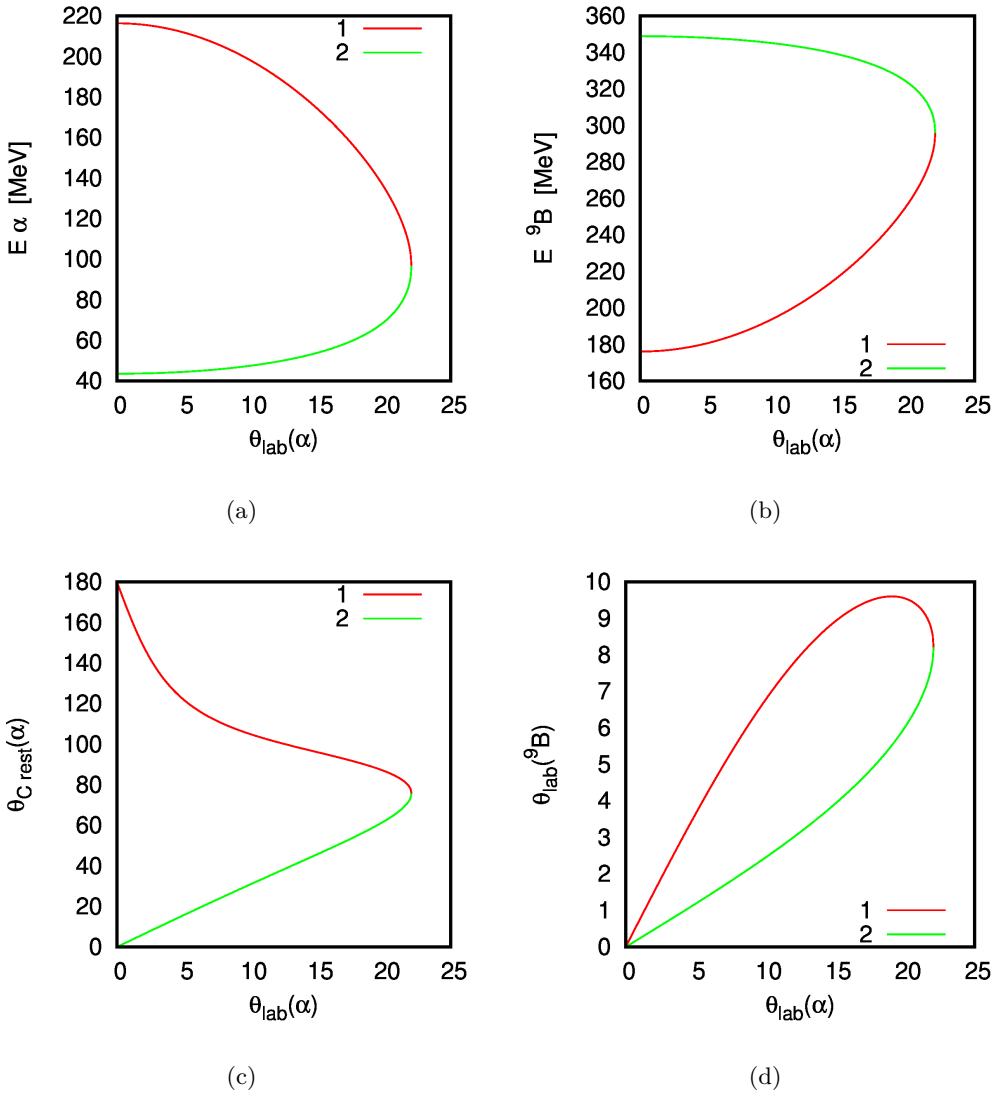

Figure 5.1. *Energy in the laboratory frame of the a (a) and of the ^9B (b) as a function of the a angle in the laboratory. (c) Angle of emission of the a fragment in the C rest frame as a function of its angle in the laboratory frame. (d) Angle of emission of the ^9B in the laboratory frame as a function of the a angle. In all these plots in red is shown the first solution and in green the second one.*

and imposing it equal to zero it is possible to find the cosine of the angle in the CM that correspond to the maximum angle in the laboratory frame:

$$\cos(\theta^\star) = -\frac{1}{\beta}\frac{p^\star}{E^\star}\,. \tag{5.22}$$

Finally to calculate θ_{max}, it is possible to use Equation 5.22 in Equation 5.20:

$$\tan(\theta_{max}) = \frac{\sqrt{1-(\frac{1}{\beta}\frac{p^\star}{E^\star})^2}}{\gamma\left[\beta\frac{E^\star}{p^\star} - \frac{1}{\beta}\frac{p^\star}{E^\star}\right]} \tag{5.23}$$

which gives $\theta_{max} = 22.0631°$ consistent with Figure 5.1(c).

5.1.2 Implementation in FLUKA

The collision of the C ion on the proton creates an excited state that could emit an α in the pre-equilibrium stage treated in the PEANUT model. This pre-equilibrium emission of an α due to a (p,α) reaction has been added to FLUKA. It works in a similar way of the pre-equilibrium emission in the continuum of nucleon (introduced in section 1.7). To the nucleon emission probability has been added a preformation factor for he α's, which is 0.2 in the low energy domain and tends to zero for higher energies, i.e. greater than the binding energy of the α particles. The initial number of excitons is three: two particle like and an hole, due to the interaction of the impinging p with the nucleus. To emit the α the nucleon-nucleon interaction chain has to produce at least four particle like excitons and two has to be neutrons and two protons, therefore at least three holes are produced. Finally, the energy of the emitted α is calculated subtracting to the total available energy the one taken by the three holes as sampled from the energy partition function.

5.2 The Electro-Magnetic dissociation

As already mentioned in Section 1.5, one of the possible kinds of interaction that leads to the break-up of the projectile nucleus is the electromagnetic dissociation. When the impact parameter is greater than the sum of the radii of the nuclei ($b > R_p + R_t$), there is no overlap between the two nuclear density. However, the electromagnetic field is so high that it provokes the excitation, and eventually the break-up of one or of even both of the nuclei.

The simplest way to describe this reaction mechanism is provided by the equivalent photon method, also commonly referred to as Weizsäcker-Williams method [Jac62]. It is based on the fact that an incident particle with charge $Z_p e$, mass M and energy E produces the same effect as a beam of photons with a spectrum $\rho(\omega)$ given, in the leading logarithmic approximation [BHTS02], by:

$$n_{app.}(\omega) = 2\frac{Z_p^2\alpha}{\pi\beta^2}\ln\left(\frac{\gamma}{\omega R_p}\right) \tag{5.24}$$

where ω is the photon energy, R_p the projectile nucleus radius, α is the fine structure constant, β is the speed of the particle and γ is the Lorentz factor.

Therefore, the cross section of electromagnetic dissociation (σ_{EMD}) can be written factoring it into the equivalent photon spectrum 5.24 and the photo-nuclear cross section for (quasi) real photons $\sigma_\gamma(\omega)$:

$$\sigma_{EMD} = \int_{\omega_{min}}^{\omega_{max}} \frac{d\omega}{\omega} n(\omega)\sigma_\gamma(\omega) \tag{5.25}$$

where ω_{min} is the threshold energy of the photon that can cause a single nucleon emission and $\omega_{max} \approx \gamma/R_p$.

The PEANUT event generator used in FLUKA (see Section 1.6) uses this model to describe the electromagnetic dissociation induced by the absorption of both real and virtual photons [BFF+14].

At relativistic energies, the field of quasireal photons contains all the multipolarities with the same weight. However, since the cross section of the electric dipole ($\sigma_{\gamma E1}$) is the dominant one, it was considered a good approximation to take into account only the contribution from $E1$ virtual photons [BFF+14]. On the contrary, at low speeds the calculation of the photonuclear cross section should be done summing the contributions from all the multipolarities. Nevertheless, only a few of them contribute in most processes [BB88]. Namely, the three dominant multipolarities are the electric dipole, the quadrupole ($E2$) and the magnetic dipole ($M1$). The electromagnetic dissociation cross section 5.25 can be rewritten as:

$$\sigma_{EMD} = \int_{\omega_{min}}^{\omega_{max}} \frac{d\omega}{\omega} [n_{E1}(\omega)\sigma_{\gamma E1}(\omega) + n_{E2}(\omega)\sigma_{\gamma E2}(\omega) + n_{M1}(\omega)\sigma_{\gamma M1}(\omega)] \tag{5.26}$$

At low energies, the $E2$ photon spectrum dominates and $\sigma_{\gamma E2}$ is its maximum in the low energy region (Figure 5.2), hence the quadrupole interaction plays an important role in low energy interactions. This contribution has been added to FLUKA to

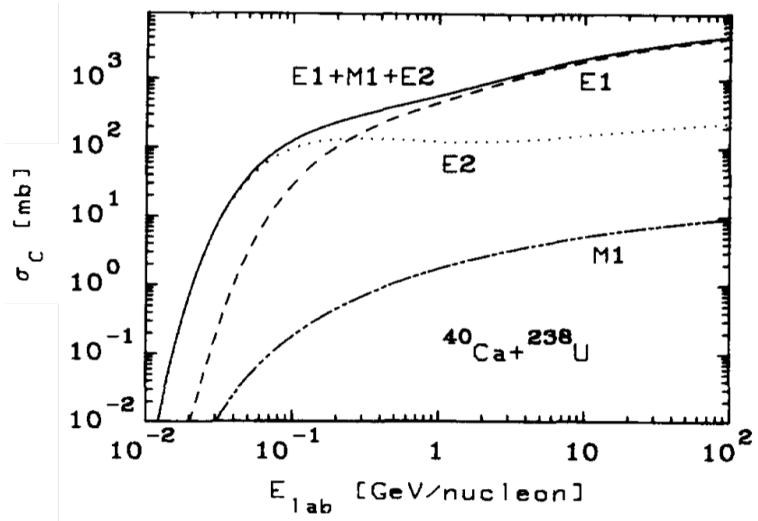

Figure 5.2. *$\sigma_{\gamma E1}(\omega)$, $\sigma_{\gamma E2}(\omega)$ and $\sigma_{\gamma M1}(\omega)$ in the interaction between ^{40}Ca with ^{238}U as a function of the laboratory energy per nucleon. Plot from [BB88].*

verify if it could add a significant contribution for the break-up of C ions in the energy region of interest.

The flux of virtual photons $n_{E1}(\omega)$ is:

$$n_{E1}(\omega) = \frac{2}{\pi} Z_p^2 \frac{\alpha}{\beta^2} \left[\zeta K_0 K_1 - \frac{\zeta^2 \beta^2}{2} \left(K_1^2 - K_0^2 \right) \right] \tag{5.27}$$

while, $n_{E2}(\omega)$ is:

$$n_{E2}(\omega) = \frac{2}{\pi} Z_p^2 \frac{\alpha}{\beta^4} \left[2 \left(1 - \beta^2 \right) K_1^2 + \zeta \left(2 - \beta^2 \right)^2 K_0 K_1 - \frac{\zeta^2 \beta^4}{2} \left(K_1^2 - K_0^2 \right) \right] \tag{5.28}$$

where K_0 and K_1 are the modified Bessel functions respectively of order zero and one, functions of the adiabaticity parameter $\zeta = \omega(R_p + R_t)c/\beta\gamma$. The increasing of the contribution of $n_{E2}(\omega)$ compared to $n_{E1}(\omega)$ in the small energy region respect to the high energy one is due to the its dependence to $1/\beta^4$, while $n_{E1}(\omega)$ depends to $1/\beta^2$.

The cross section $\sigma_{\gamma E2}(\omega)$ is calculated following Prestwich et al. [PIK84] with a Lorentzian:

$$\sigma_{\gamma E2}(\omega) = \sigma_0 \frac{\Gamma_T^2 \omega^2}{\left(\omega^2 - E_T^2 \right)^2 + \Gamma_T^2 \omega^2} \tag{5.29}$$

where σ_0 is the peak cross section of the quadrupole resonance centred at energy E_T and width Γ_T. σ_0 has been calculated [PIK84] as:

$$\sigma_0 = \frac{2}{5} \frac{\pi \alpha R_p^2 A_p^{\frac{1}{3}} Z_p^2 E_0^2}{M_p c^2 \Gamma_T} = 0.14 \frac{Z_p A_p^{\frac{2}{3}} E_0^2 \, [\mathrm{MeV}^2]}{\Gamma_T \, [\mathrm{MeV}]} \, [\mu\mathrm{b}] \tag{5.30}$$

Experimental data show the following dependency of E_T from A [Kapecky]:

$$E_T = A^{\frac{1}{3}} \cdot 63 \, \mathrm{MeV} \tag{5.31}$$

and for Γ_T [IAEA]

$$\Gamma_T = 6.11 \, \mathrm{MeV} - A \cdot 0.021 \, \mathrm{MeV} \tag{5.32}$$

Since the numerical integration of the $n_{E1}(\omega)\sigma_{\gamma E1}(\omega)$ and $n_{E2}(\omega)\sigma_{\gamma E2}(\omega)$ products is very time consuming, the program uses an approximation to initially evaluate the probability of an electromagnetic dissociation, and in case calculate exactly the cross sections and the photon equivalent fluxes. For the initial estimation the photon energy range is divided into intervals; $\sigma_\gamma(\omega)$ is approximated with Bezier curves, and the total equivalent photon spectrum is calculated in the leading order approximation as:

$$n_{app.}(\omega) = 2 \frac{Z^2 \alpha}{\pi} \ln \left(\frac{\gamma}{\omega R_p} \right) \tag{5.33}$$

the product of the fit made with the Bezier curves and $n_{app.}(\omega)$ is analytically integrable and allows an overestimation of the total cross section σ_{EMD}. If the electromagnetic interaction is selected, the program samples the photon energy ω and calculates the probability of the interaction to happen as the ratio of the cross section exactly calculated for the selected ω and the approximated one:

$$P(\omega) = \frac{n_{E1}(\omega)\sigma_{\gamma E1}(\omega) + n_{E2}(\omega)\sigma_{\gamma E2}(\omega)}{n_{app.}(\omega)\sigma_{Bezier}(\omega)} \tag{5.34}$$

this technique allows fast estimation of the cross section for hundreds of nuclides without introducing any approximations.

After being excited, the nucleus can emit protons and neutrons before the thermalisation. Afterwards, the deexcitation proceeds through evaporation, fission, or, for light nuclei, Fermi break-up (Section 1.7.2). Parity and angular momentum conservation is taken into account according to the multipolarity selected for the interaction.

Despite of the fact that for low energy the relevance of the $E2$ contribution is greater than the higher one, in the purpose of this work a preliminary analysis showed that it did not give any significant contribution.

Chapter 6

Results

The experiment described in this work has been performed in order to measure the cross section of the quasi-elastic break-up of Carbon ions into ^{8}Be and α on different materials. The doubly peak structure and the excess of α's in the high energy region have been attributed to a Hydrogen contamination in the targets and to the production of $^{9}B_{gs}$ out of the interactions of the Carbon ion beam with the contaminant. This interaction has been added as a possible channel of the pre-equilibrium stage in FLUKA.

This chapter highlights the comparison of the cross section calculated with FLUKA with experimental data of α production in the interaction of Proton beam with ^{16}O target as well as the cross section of quasi-elastic breakup of ^{12}C with the different targets, limiting the impact of the H contamination.

6.1 Benchmark of the (p,α) reaction

The Figures 6.1 show the cross sections calculated with FLUKA for the inclusive production of H, Deuterium and α particles in the interaction of a p beam with 61.4 MeV with an ^{16}O target. The experimental data are taken from [BP73]. The left panel shows the FLUKA output before the introduction of the α as a possible ejectile, as described in subsection 5.1.2, while the one on the right shows the same cross section calculated after the implementation of the (p,α) reaction. As it is possible to see comparing the two plots, FLUKA now reproduces accurately the high energy part of the α emission spectrum, the region where the pre-equilibrium emission of α particles is more significant. This benchmark shows that the α preformation factor gives a total cross section for the (p,α) reaction compatible with experimental data, independently from the $(CH_2)_n$ target data described in this work.

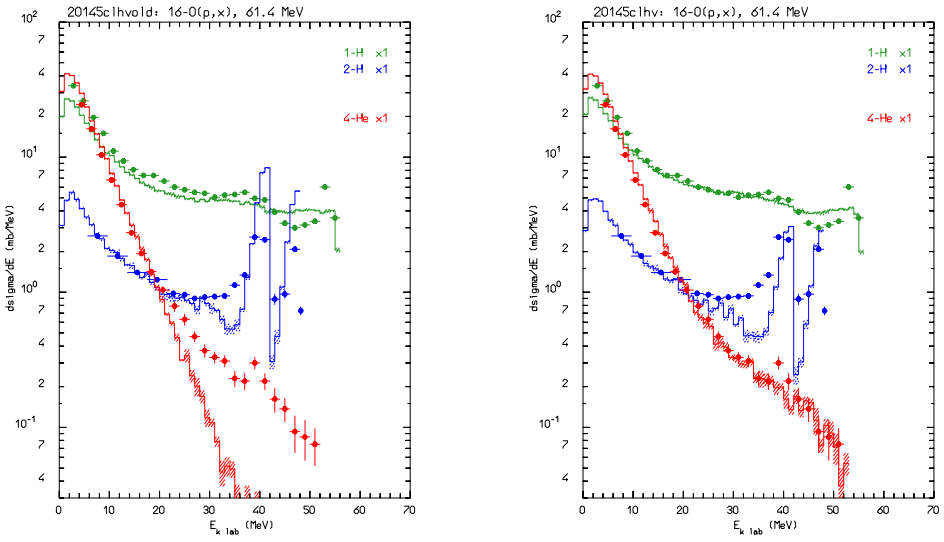

(a) (b)

Figure 6.1. *Comparison of the cross sections for (p,p) in green, (p,d) in blue and (p,a) in red before (left panel) and after (right panel) the implementation in* FLUKA *of the a as a possible ejectile of the pre-equilibrium stage. The histograms are the* FLUKA *calculations while the dots are the experimental data points. Data from [BP73].*

6.2 The ^{12}C quasi-elastic break-up cross section

To limit the impact of Hydrogen, it is possible to modify the selection criteria, requiring not only at least two strips in the cuts described in section 4.3, but also that no more than two SSD strips fire. In this way, at least the events where the proton (coming from the decay of the ^{9}B) is detected, are rejected. Figures 6.2 show the total and the α telescope energy distribution related to $(CH_2)_n$ target with the α telescope at 16°. The higher peak in the total energy, the one where also the proton is entering in the detectors, is significantly reduced. The residual fraction of the peak is due to the protons that pass through the SSD frame and reach the subsequent NaI.

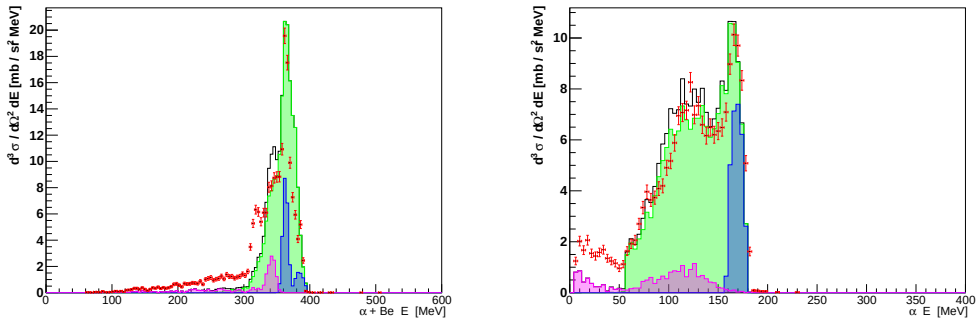

(a) (b)

Figure 6.2. *Total (a) and α telescope (b) energy distributions obtained with the $(CH_2)_n$ target and the α telescope at 16°. In red the experimental data, in black the total MC; in green the total contribution of the H contamination and in blue the part of these where a $^{9}B_{gs}$ has been produced. In magenta the C contribution.*

6.2.1 Niobium target

Figures 6.3 highlight the results for the data and MC related to Nb target and the α telescope placed at 16°. The contamination of H here is assumed to be 3.8 µg/cm^2, as found in subsection 4.6.2.

From the projection on the two axis (Figures 6.3(c) and 6.3(d)) it is possible to see that the contribution of the H contamination is considerable, nevertheless the events due to the interaction with Nb can still be identified. Moreover, the quasi-elastic break-up of ^{12}C in α and ^{8}Be on Nb target peak is visible in Figure 6.3(a) with total Energy in the range 367 ÷ 410 MeV. To better identify this peak it is possible to project on the α axis only the part of the bi-dimensional spectrum in the total Energy range 367 ÷ 410 MeV. The result is shown in Figure 6.4. In this plot the contribution of the H contamination is even more limited.

Unfortunately, the data relative to the Nb target, with the α telescope placed at 18°, 20° and 22° have been corrupted. Except the data set with the α telescope placed at 16°, the only one available relates to data acquired with the α telescope placed at 24°. Figure 6.5 shows the results for this configuration, with the same gate

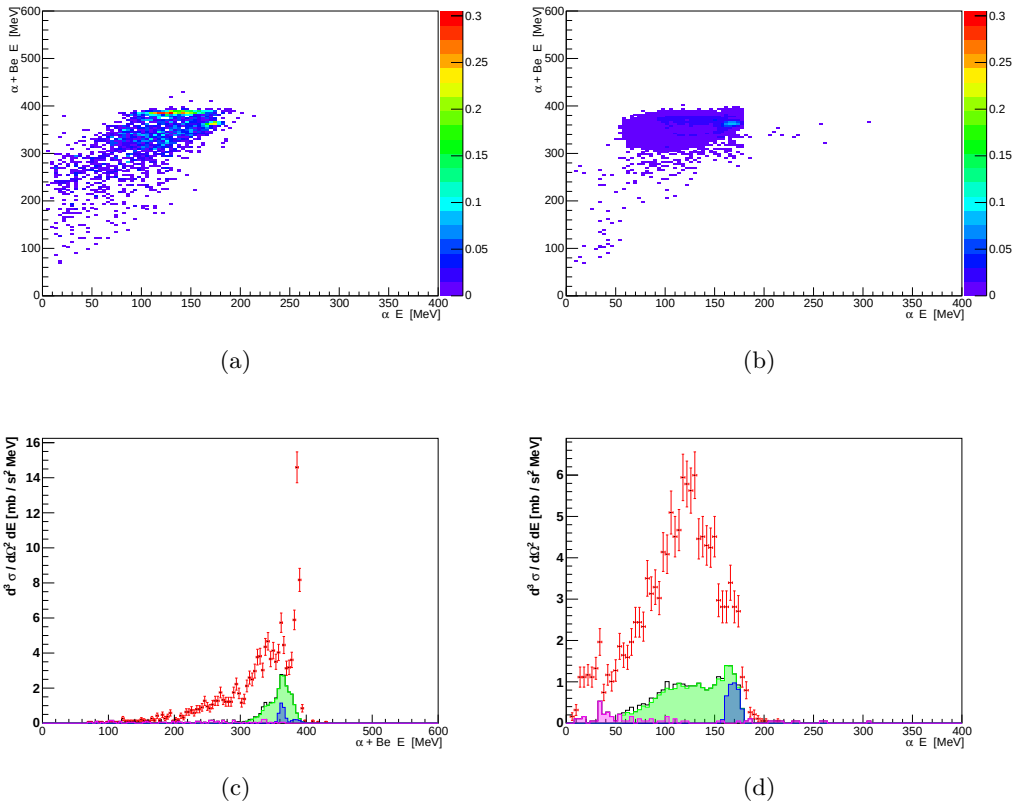

Figure 6.3. *Bi-dimensional cross section on Nb target, with the a telescope at* $16°$ *from experimental data (a) and MC (b). In (c) their projection on the Y axis and in (d) the projection on the X axis. In these two plots in red are shown the experimental data, in black the total MC; in green the total contribution of the H contamination and in blue the part of these where a* $^9B_{gs}$ *has been produced. In magenta the C contribution.*

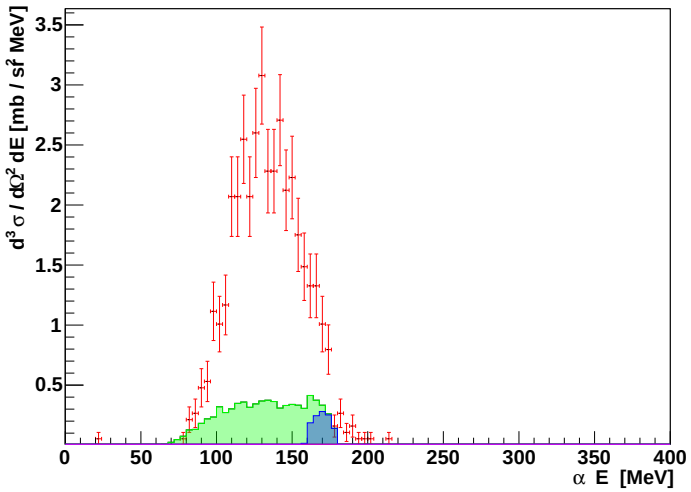

Figure 6.4. *Projection of the spectrum in Figure 6.3 on the a axis selecting only the events with total energy in the range* $367 \div 410\,\mathrm{MeV}$*. a telescope placed at* $16°$*.*

described before to insultate the quasi-elastic break-up in the data, since at such angle the H contamination does not appear, for the kinematic reasons described in subsection 5.1.1.

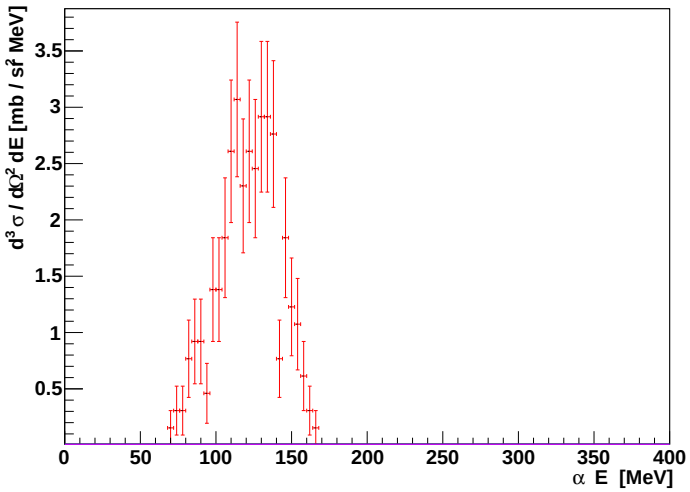

Figure 6.5. *Same as Figure 6.4 but with the a telescope placed at* 24°.

6.2.2 Gold target

The same analysis performed on the Nb related data has been applied on Au data. The results are shown in Figures 6.6, while the projection on the α axis in the gate set to insulate the quasi-elastic peak is shown in Figure 6.7. Also in this case, the quasi elastic peaks due to the interaction with the target material can be identified. For this target, the data are available with the α telescope placed at 16° (Figure 6.7), 18° (Figure 6.8), 20° (Figure 6.9) and 24° (Figure 6.10). A run with the a telescope placed at 22° was not done.

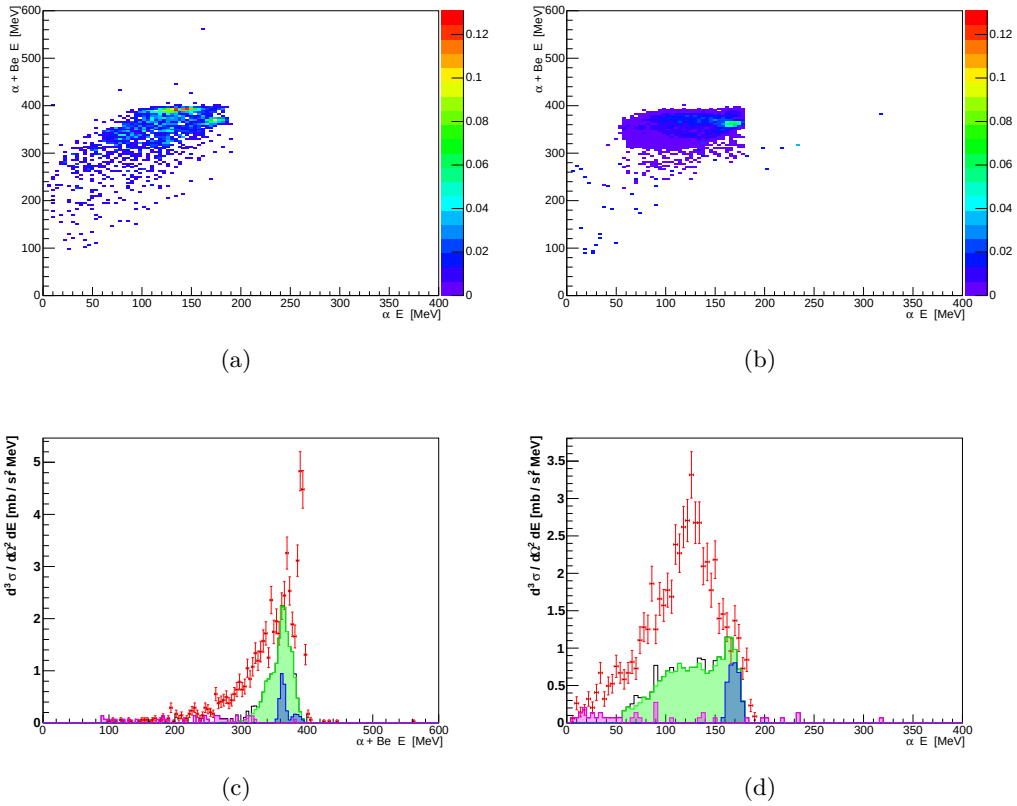

Figure 6.6. *Same as Figures 6.3 but for the Au target.*

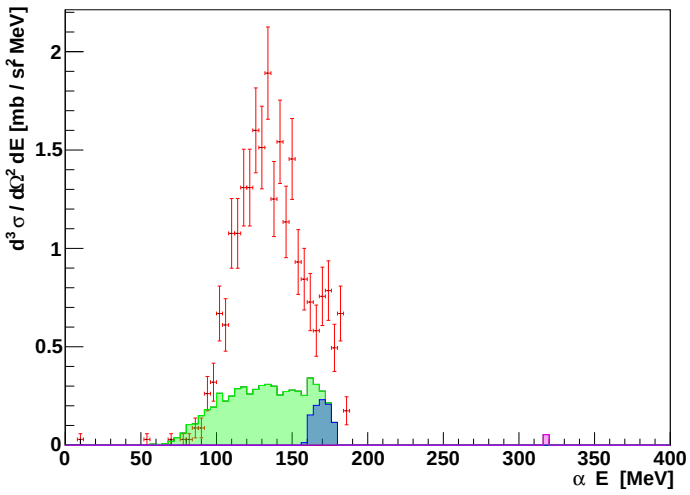

Figure 6.7. *Same as Figure 6.4 but for Au target. a telescope placed at* 16°.

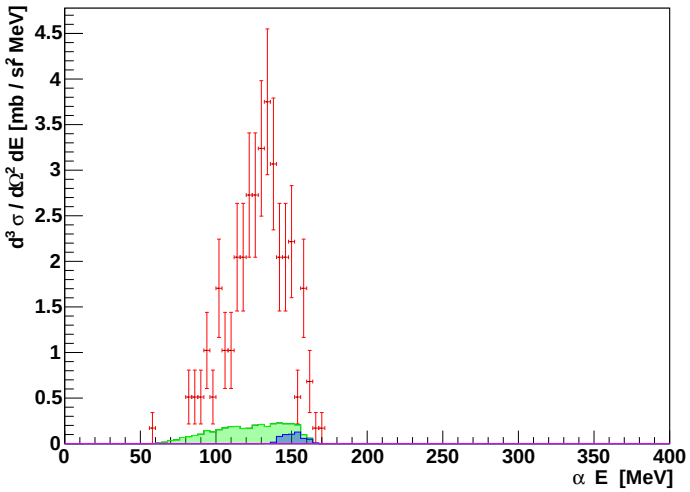

Figure 6.8. *Same as Figure 6.7 but with the a telescope placed at* 18°.

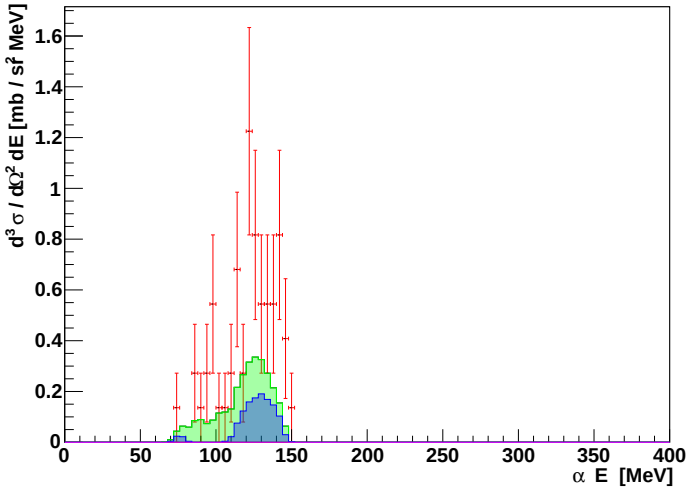

Figure 6.9. *Same as Figure 6.7 but with the a telescope placed at* 20°.

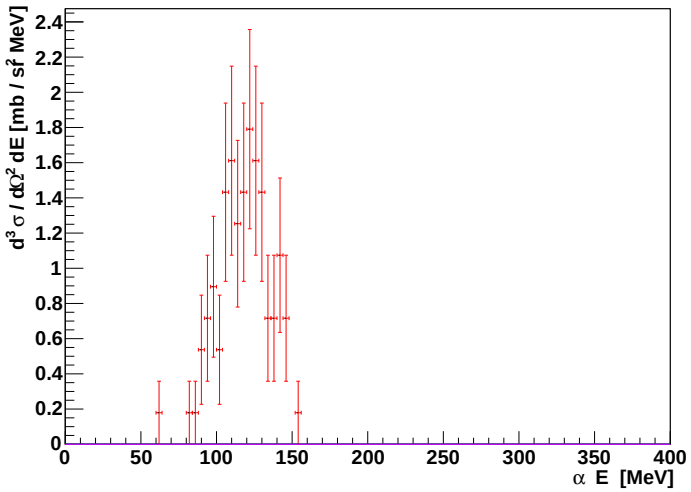

Figure 6.10. *Same as Figure 6.7 but with the a telescope placed at* 24°.

6.2.3 Carbon target

The results for the C target are presented in Figures 6.11, while the gated region in Figure 6.12. Although it seems that the contamination of H in the target has been overestimated, the quasi elastic peak can still be identified and the H contribution in the projection of the gated region appears limited.

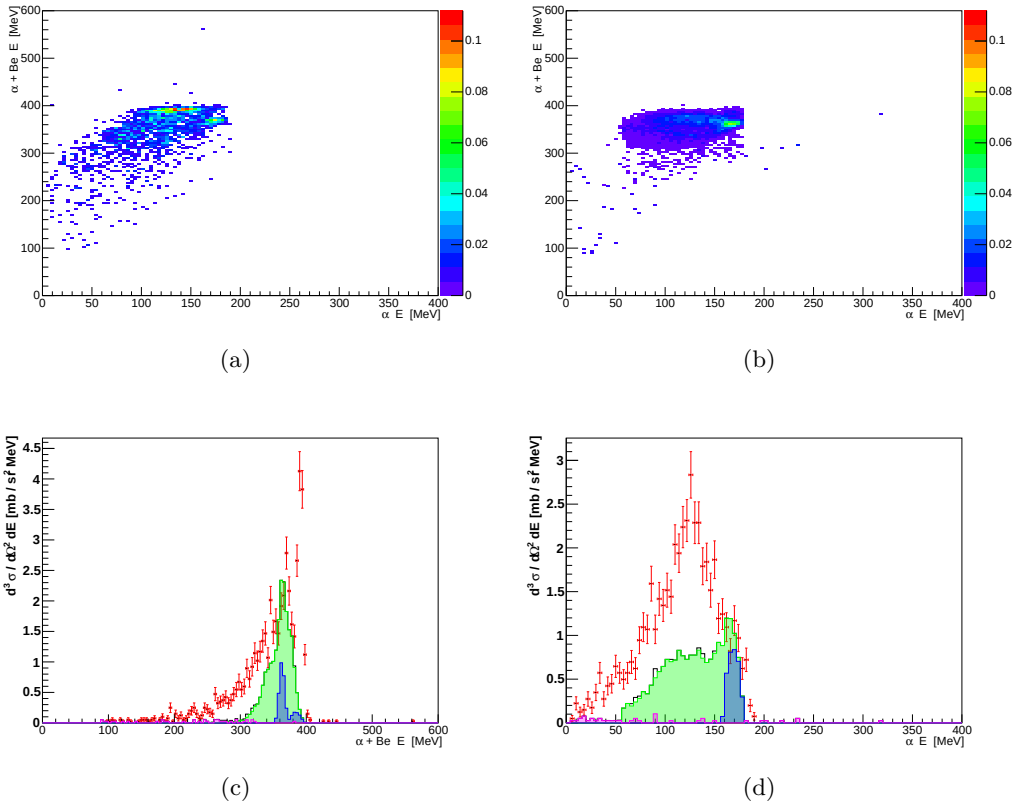

Figure 6.11. *Same as Figures 6.3 but for the C target.*

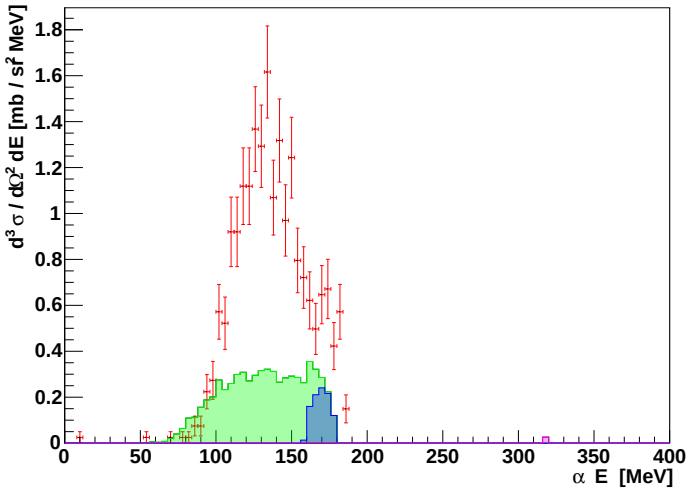

Figure 6.12. *Same as Figure 6.4 but for C target. a telescope placed at* 16°.

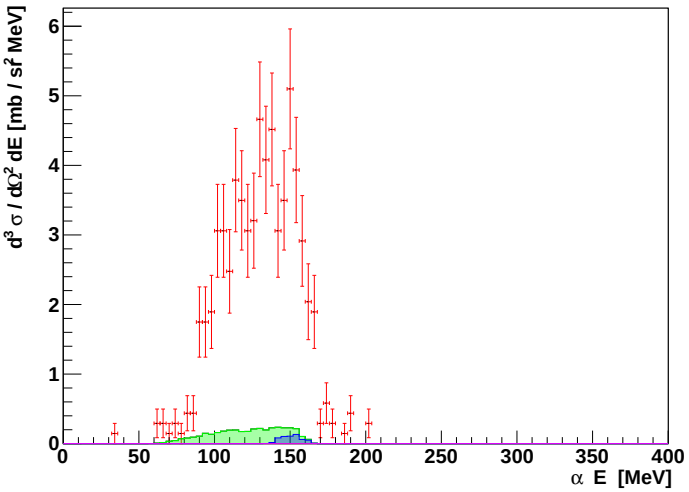

Figure 6.13. *Same as Figure 6.12 but with the a telescope placed at* 18°.

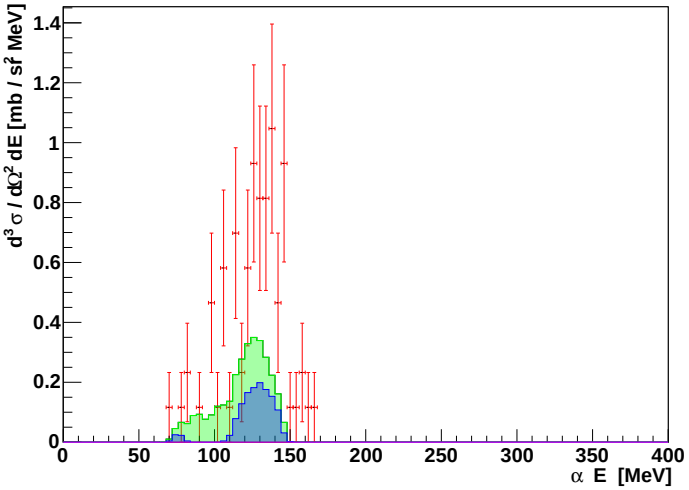

Figure 6.14. *Same as Figure 6.12 but with the a telescope placed at* 20°.

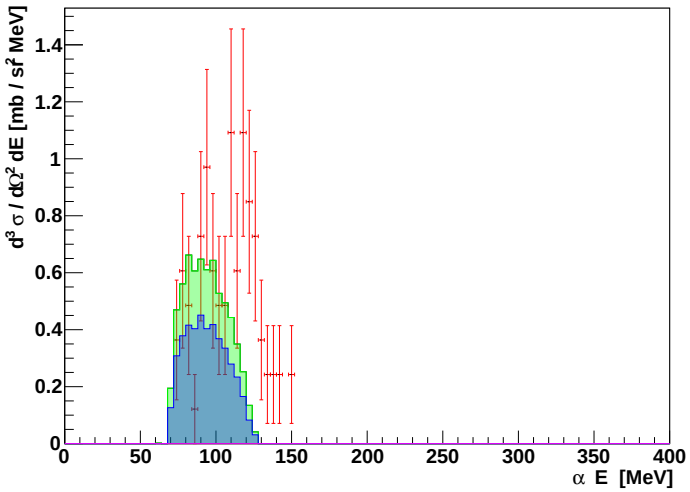

Figure 6.15. *Same as Figure 6.12 but with the a telescope placed at* 22°.

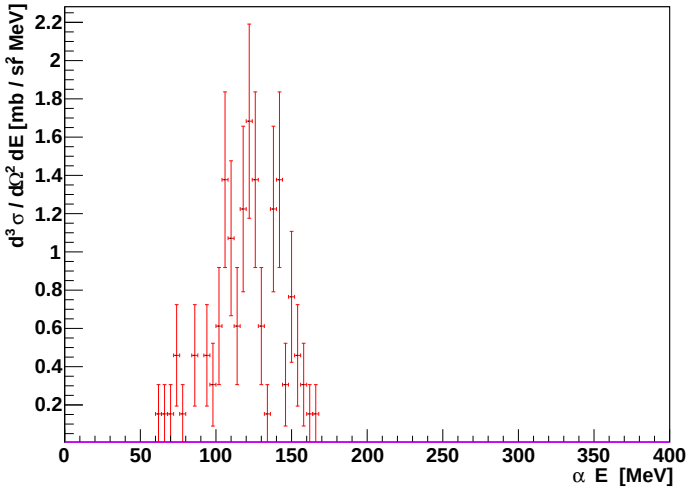

Figure 6.16. *Same as Figure 6.12 but with the a telescope placed at* 24°.

In the data relative to all targets at 20° it can be noticed to see that the second possible solution (already described in subsection 5.1.1) of a (p,α) reaction between ^{12}C and the H contaminant the target with the emission of ^{9}B in the acceptance of the Be telescope and the α in the acceptance of the other telescope is visible, even if the amount of such events is limited. The small peak with α at 75 MeV in the MC data is due to this second solution.

The plot with the α telescope placed at 22° shows an excess in the MC of ^{9}B production compared to the data, indeed it seems that this process suffices to reproduce all the data. However, this large impact of the H contamination in the MC data could be explained with the fact that this is the limit angle for the ^{9}B production in the Proton rest frame, and in this frame the cross section has a sharp peak, as already discussed in subsection 4.6.1, and even a small underestimation of the beam spot size or of its energy spread could significantly modify the amount of ^{9}B produced at this angle.

Chapter 7

Summary

This work presents the analysis of the data resulting from a correlation experiment that measured the quasi-elastic break-up of C ions with an energy of 33 MeV u^{-1} in α and Be on different targets, i.e. the reaction $^{12}C + x \rightarrow ^{8}$ Be + α. The ^{8}Be decays into two correlated α's, therefore the final state is constituted by three α's, two of them correlated to each other. The experiment has been carried out with target made in different materials, namely Gold, Carbon and Niobium. Two sets of detectors (telescopes) have been used, one to identify and measure the energy of the α produced in correlation with the ^{8}Be, and the other one to detect the two α's coming from the ^{8}Be decay. The α telescope is formed by two silicon detectors and one NaI scintillator crystal. The ^{8}Be telescope is made by a silicon detector and a NaI crystal. The silicon detector in this case is made by 16 vertical strips, in order to allow the identification of the two α's separately. The particles identification has been done in both the telescopes measuring the energy deposition in the first thin detector as a function of the remaining energy deposited in the subsequent thick detector. In the α telescope the second silicon detector has been used as a stopping detector for the low energy particles and as a passing through for the high energy particles. The α telescope has been placed at different angles in respect to the C flight direction to measure also the angular dependence of the cross section of the reaction under investigation.

To analyse the experimental data a complete MC simulation has been realised using the FLUKA framework. The MC simulation allows an event by event analysis.

It has been found a surprising doubly peak structure in the total energy spectra with and an excess of high energy α. These unexpected features have been attributed to a H contamination in the target and to the production of ^{9}B as intermediate state. The reaction is: $^{12}C + p \rightarrow ^{9}$ B + α, the ^{9}B subsequently decays in a p and a ^{8}Be miming the experimental signature of the process under investigation and underlying a source of background. To describe this process, the (p,α) reaction has been added as a channel of the pre-equilibrium stage of FLUKA. A dedicated analysis has been developed to insulate only the contribution of the contaminant. It is made to insulate the events in which all the particles produced in the ^{9}B are detected separately in three different strips of the silicon detector of the Be telescope. The application of such analysis to the MC data showed that it is efficient in selecting only the channel with the ^{9}B as intermediate state. The comparison of the application of this

analysis to the data acquired with each target and the ones taken with a $(CH_2)_n$ target allowed to estimate the amount of H in each of them. Using these values to scale the output of the MC, the contribution of H has been simulated and identified in the data relative to each target and each position of the α telescope.

Finally, the quasi-elastic break-up cross section of C ions as a function of the energies of the fragments and the angle of emission of the α fragment on C, Nb and Au targets has been insulated and presented.

The data analysed in this work will be fundamental to the implementation of the quasi elastic break-up of C ions in FLUKA. During this work the quadrupole interaction has been added to the electromagnetic dissociation cross section, because it was believed to have a role in the low energy interaction. However, the simulation shows that for this experiment the quadrupole contribution is negligible.

The implementation of the quasi-elastic break-up of C ions is of utmost importance for the use of FLUKA in hadrontherapy. Indeed the use of ^{12}C ions is at the frontier of development, and the considered energy is just in the range of values of the ion close to the point where there is the maximum energy deposition in the tissue, i.e. the Bragg peak, and close to the maximum of biological effect. Having a reliable MC simulation of the fragments produced permits a better estimation of the biological effects of the dose deposited during the treatment. Indeed, the biological effect is a function of the quality of the radiation and not only of the deposited dose. Moreover, the (p,α) reaction measured thanks to the contamination of H in the target could be important to reevaluate the recoil fragments production for the therapy with protons.

Bibliography

[AFSR97] H. Hirayama, Ed., *New developments in FLUKA modelling hadronic and EM interactions*, vol. 5, 97, KEK, Tsukuba (Japan): KEK Proceedings, 1997 (cit. on p. 8).

[Ahl80] S. P. Ahlen, "Theoretical and Experimental Aspects of the Energy Loss of Relativistic Heavily Ionizing Particles", English, *Reviews of Modern Physics*, vol. 52, no. 1, pp. 121–173, 1980. DOI: 10.1103/RevModPhys.52.121. [Online]. Available: http://link.aps.org/doi/10.1103/RevModPhys.52.121 (cit. on p. 4).

[ABB+04] V Andersen, F Ballarini, G Battistoni, M Campanella, M Carboni, F Cerutti, A Empl, A Fassò, A Ferrari, E Gadioli, M. V. Garzelli, K Lee, A Ottolenghi, M Pelliccioni, L. S. Pinsky, J Ranft, S Roesler, P. R. Sala, and T. L. Wilson, "The fluka code for space applications: recent developments", English, *Advances in Space Research*, vol. 34, no. 6, pp. 1302–1310, Jan. 2004. DOI: 10.1016/j.asr.2003.03.045. [Online]. Available: http://linkinghub.elsevier.com/retrieve/pii/S0273117704002054 (cit. on p. 9).

[BBB+08] G Battistoni, F Broggi, M Brugger, M Campanella, M Carboni, F Cerutti, P Colleoni, C D'Ambrosio, A Empl, A Fassò, A. Ferrari, A. Ferrari, E Gadioli, M Lantz, K Lee, G Lukasik, A Mairani, A Margiotta, M Mauri, M. C. Morone, A Mostacci, S Muraro, K Parodi, V Patera, M Pelliccioni, L Pinsky, J Ranft, S Roesler, S Rollet, P. R. Sala, L Sarchiapone, M Stoli, G Smirnov, F Sommerer, C Theis, S Trovati, R Villari, H Vinke, V Vlachoudis, T Wilson, and N Zapp, "The FLUKA code and its use in hadron therapy", *Nuovo Cimento Della Societa Italiana Di Fisica C-Colloquia on Physics*, vol. 31, no. 1, pp. 69–75, 2008. DOI: 10.1393/ncc/i2008-10281-9. [Online]. Available: http://gateway.webofknowledge.com/gateway/Gateway.cgi?GWVersion=2&SrcAuth=mekentosj&SrcApp=Papers&DestLinkType=FullRecord&DestApp=WOS&KeyUT=000260719100008 (cit. on p. 8).

[BHTS02] G Baur, K Hencken, D Trautmann, and S Sadovsky, "Coherent< i> $\gamma\gamma$</i> and< i> γA</i> interactions in very peripheral collisions at relativistic ion colliders", *Physics Reports*, vol. 364, no. 5, pp. 359–450, 2002. DOI: 10.1016/S0370-1573(01)00101-6. [Online]. Available: http://linkinghub.elsevier.com/retrieve/pii/S0370157301001016 (cit. on p. 65).

[NIST] M. Berger, J. Coursey, M. Zucker, and J. Chang, *Http://physics.nist.gov/star*, Gaithersburg, MD: National Institute of Standards and Technology. [Online]. Available: `http://physics.nist.gov/Star` (cit. on pp. 39, 43–45).

[BPS08] J. A. Bertout, S. A. Patel, and M. C. Simon, "The impact of O2 availability on human cancer", *Nature Reviews Cancer*, vol. 8, no. 12, pp. 967–975, Nov. 2008. DOI: `10.1038/nrc2540`. [Online]. Available: `http://www.nature.com/doifinder/10.1038/nrc2540` (cit. on p. 3).

[BP73] F. E. Bertrand and R. W. Peelle, "Complete Hydrogen and Helium Particle Spectra from 30- to 60-MeV Proton Bombardment of Nuclei with A=12to209 and Comparison with the Intranuclear Cascade Model", English, *Phys.Rev.*, vol. C8, no. 3, pp. 1045–1064, 1973. DOI: `10.1103/PhysRevC.8.1045`. [Online]. Available: `http://link.aps.org/doi/10.1103/PhysRevC.8.1045` (cit. on pp. 69, 70).

[BB88] C. A. Bertulani and G. Baur, "Electromagnetic Processes in Relativistic Heavy Ion Collisions", English, *Phys.Rept.*, vol. 163, no. 5-6, pp. 299–408, 1988. DOI: `10.1016/0370-1573(88)90142-1`. [Online]. Available: `http://linkinghub.elsevier.com/retrieve/pii/0370157388901421` (cit. on p. 66).

[Bet30] H. Bethe, "Zur theorie des durchgangs schneller korpuskularstrahlen durch materie", *Ann. Phys.*, vol. 397, pp. 325–400, 1930 (cit. on p. 4).

[BBC+96] C Birattari, M Bonardi, M Cavinato, E Fabrici, E Gadioli, E Gadioli-Erba, F Groppi, M Bello, C Bovati, A Di Filippo, T Stevens, S Connell, J Sellschop, S Mills, F Nortier, G Steyn, and C Marchetta, "Preequilibrium processes in the fusion of C12 with Rh103 up to 20 MeV/nucleon", English, *Physical Review C*, vol. 54, no. 6, pp. 3051–3055, Dec. 1996. DOI: `10.1103/PhysRevC.54.3051`. [Online]. Available: `http://link.aps.org/doi/10.1103/PhysRevC.54.3051` (cit. on p. 6).

[Bir64] J. B. Birks, *The Theory and practice of scintillation counting*. 1964 (cit. on p. 28).

[Bla71] M. Blann, *Phys. Rev. Lett.*, no. 27, p. 337, 1971 (cit. on p. 11).

[Bla72] ——, *Phys. Rev. Lett.*, no. 28, p. 757, 1972 (cit. on p. 11).

[Bla83] ——, *Phys. Rev.*, no. C28, p. 1648, 1983 (cit. on p. 11).

[BV83] M. Blann and H. Vonach, *Phys. Rev.*, no. C28, p. 1475, 1983 (cit. on p. 11).

[Blo33] F. Bloch, "Bremsvermögen von atomen mit mehreren elektronen", *Z. Phys. A: Hadrons Nucl.*, vol. 81, pp. 363–376, 1933 (cit. on p. 4).

[BCC+14] T. T. Böhlen, F Cerutti, M. P. W. Chin, A Fassò, A Ferrari, P. G. Ortega, A Mairani, P. R. Sala, G Smirnov, and V Vlachoudis, "The FLUKA Code: Developments and Challenges for High Energy and Medical Applications", *Nuclear Data Sheets*, vol. 120, no. C, pp. 211–214, Jun. 2014. DOI: 10.1016/j.nds.2014.07.049. [Online]. Available: http://dx.doi.org/10.1016/j.nds.2014.07.049 (cit. on pp. 8, 14).

[BM69] A. Bohr and B. Mottelson, *Nuclear Structure*. W.A. Benjamin, Inc., 1969, vol. 1 (cit. on p. 11).

[BK05] W. H. Bragg and R Kleeman, "XXXIX. On the α particles of radium, and their loss of range in passing through various atoms and molecules", English, *Philosophical Magazine Series 6*, vol. 10, no. 57, pp. 318–340, Sep. 1905. DOI: 10.1080/14786440509463378. [Online]. Available: http://www.tandfonline.com/doi/abs/10.1080/14786440509463378 (cit. on p. 2).

[BFF+14] H. H. Braun, A Fassò, A Ferrari, J. M. Jowett, P. R. Sala, and G. I. Smirnov, "Hadronic and electromagnetic fragmentation of ultrarelativistic heavy ions at LHC", English, *Physical Review Special Topics - Accelerators and Beams*, vol. 17, no. 2, p. 021 006, Feb. 2014. DOI: 10.1103/PhysRevSTAB.17.021006. [Online]. Available: http://link.aps.org/doi/10.1103/PhysRevSTAB.17.021006 (cit. on pp. 9, 66).

[BQ61] H. C. Britt and A. R. Quinton, "Alpha Particles and Protons Emitted in the Bombardment of Au 197 and Bi 209 by C 12, N 14, and O 16 Projectiles", English, *Physical Review*, vol. 124, no. 3, pp. 877–887, 1961. DOI: 10.1103/PhysRev.124.877. [Online]. Available: http://link.aps.org/doi/10.1103/PhysRev.124.877 (cit. on p. 5).

[BQ60] H. C. Britt and A. R. Quinton, "Fission of Au-197 and Bi-209 by C-12 and O-16 Projectiles", *Phys.Rev.*, vol. 120, pp. 1768–1777, 1960. DOI: 10.1103/PhysRev.120.1768 (cit. on p. 5).

[BR97] R. Brun and F. Rademakers, "ROOT — An object oriented data analysis framework", English, *Nuclear Instruments and Methods in Physics Research Section A: Accelerators, Spectrometers, Detectors and Associated Equipment*, vol. 389, no. 1-2, pp. 81–86, Apr. 1997. DOI: 10.1016/S0168-9002(97)00048-X. [Online]. Available: http://linkinghub.elsevier.com/retrieve/pii/S016890029700048X (cit. on p. 21).

[CFGER98] M Cavinato, E Fabrici, E Gadioli, E. G. Erba, and E Risi, "Boltzmann master equation theory of angular distributions in heavy-ion reactions", English, *Nuclear Physics A*, vol. 643, no. 1, pp. 15–29, 1998. DOI: 10.1016/S0375-9474(98)00545-4. [Online]. Available: http://linkinghub.elsevier.com/retrieve/pii/S0375947498005454 (cit. on p. 13).

[CBC06] F Cerutti, G Battistoni, and G Capezzali, "Low energy nucleus–nucleus reactions: the BME approach and its interface with FLUKA", *Proc 11th Int Conf ...*, 2006. [Online]. Available: http://lxmi.mi.infn.it/~gadioli/Varenna2006/Proceedings/Cerutti_F.pdf (cit. on pp. 9, 14).

[CCG05] F Cerutti, A Clivio, and E Gadioli, "A semiclassical formula for the reaction cross-section of heavy ions", English, *The European Physical Journal A - Hadrons and Nuclei*, vol. 25, no. 3, pp. 413–418, Sep. 2005. DOI: 10.1140/epja/i2005-10129-8. [Online]. Available: http://www.springerlink.com/index/10.1140/epja/i2005-10129-8 (cit. on p. 12).

[CFP91] E Cuccou, A Ferrari, and G. C. Panini, "A group library from JEF 1.1 for flux calculations in the LHC machine detectors", 1991. [Online]. Available: http://www.fluka.org/content/publications/1991_cuccoli.pdf (cit. on p. 8).

[Emm75] M. B. Emmett, "The MORSE Monte Carlo Radiation Transport Code System", 1975 (cit. on p. 8).

[ÉG67] M. Épherre and É. Gradsztajn, "Calcul de la spallation de 12C et 16O par des protons de 70 à 200 MeV", French, *Journal de Physique*, vol. 28, no. 10, pp. 745–751, 1967. DOI: 10.1051/jphys:019670028010074500. [Online]. Available: http://www.edpsciences.org/10.1051/jphys:019670028010074500 (cit. on p. 14).

[eal71] C. K. et al., *Phys. Rev. C*, vol. 4, no. 2234, 1971 (cit. on p. 11).

[Fan63] U Fano, "Penetration of protons, alpha particles, and mesons", English, *Ann.Rev.Nucl.Part.Sci.*, vol. 13, no. 1, pp. 1–66, 1963. DOI: 10.1146/annurev.ns.13.120163.000245. [Online]. Available: http://www.annualreviews.org/doi/abs/10.1146/annurev.ns.13.120163.000245 (cit. on p. 4).

[Fer50] E. Fermi, *Prog. Theor. Phys*, vol. 5, no. 1570, 1950 (cit. on p. 14).

[FSGP92] A Ferrari, P. R. Sala, R Guaraldi, and F Padoani, "An improved multiple scattering model for charged particle transport", English, *Nuclear Instruments and Methods in Physics Research Section B: Beam Interactions with Materials and Atoms*, vol. 71, no. 4, pp. 412–426, Sep. 1992. DOI: 10.1016/0168-583X(92)95359-Y. [Online]. Available: http://linkinghub.elsevier.com/retrieve/pii/0168583X9295359Y (cit. on p. 8).

[FS98] *The physics of high energy reactions.* Workshop on Nuclear Reaction Data, Nuclear Reactors Physics, Design, and Safety, 1998, p. 424. [Online]. Available: http://www.fluka.org/content/publications/1996_trieste.pdf (cit. on p. 8).

[FS02] A. Ferrari and P. R. Sala, "Nuclear reactions in Monte Carlo codes", *Radiat. Prot. Dosim.*, vol. 99, no. 1-4, pp. 29–38, 2002. [Online]. Available: http://www.fluka.org/content/publications/1996_trieste.pdf (cit. on p. 8).

[FSFR05] A. Ferrari, P. R. Sala, A. Fasso, and J. Ranft, "FLUKA: A multi-particle transport code (Program version 2005)", 2005 (cit. on pp. 8, 12).

[FLU11] FLUKA, "a multi-particle transport code", pp. 1–447, Mar. 2011 (cit. on p. 28).

[FM94] H Fuchs and K Mohring, "Heavy-ion break-up processes in the Fermi energy range", English, *Reports on Progress in Physics*, vol. 57, no. 3, pp. 231–324, Mar. 1994. DOI: 10.1088/0034-4885/57/3/001. [Online]. Available: http://stacks.iop.org/0034-4885/57/i=3/a=001?key=crossref.ba3d2aca24fd8e75106d1ad5ca408807 (cit. on p. i).

[GBCF98] E Gadioli, C Birattari, M Cavinato, and E Fabrici, "Angular distributions and forward recoil range distributions of residues created in the interaction of< sup> 12</sup> C and< sup> 16</sup> O ions with< sup> 103</ ...", English, *Nuclear Physics A*, vol. 641, no. 3, pp. 271–296, 1998. DOI: 10.1016/S0375-9474(98)00472-2. [Online]. Available: http://linkinghub.elsevier.com/retrieve/pii/S0375947498004722 (cit. on p. 6).

[GBC+97] E Gadioli, C Birattari, M Cavinato, E Fabrici, E Gadioli-Erba, V Allori, C Bovati, F Cerutti, A Di Filippo, E Galbiati, T. G. Stevens, S. H. Connell, J. P. F. Sellschop, S. J. Mills, F. M. Nortier, G. F. Steyn, and C Marchetta, "Comprehensive study of the reactions induced by 12C on 103Rh up to 33 MeV/nucleon", English, *Physics Letters B*, vol. 394, no. 1-2, pp. 29–36, Feb. 1997. DOI: 10.1016/S0370-2693(97)00003-8. [Online]. Available: http://linkinghub.elsevier.com/retrieve/pii/S0370269397000038 (cit. on p. 6).

[GCF+99] E Gadioli, M Cavinato, E Fabrici, E. G. Erba, C Birattari, I Mica, S Solia, G. F. Steyn, S. V. Förtsch, J. J. Lawrie, F. M. Nortier, T. G. Stevens, S. H. Connell, J. Sellschop, and A. A. Cowley, "Alpha particle emission in the interaction of C-12 with Co-59 and Nb-93 at incident energies of 300 and 400 MeV", *Nuclear Physics A*, vol. 654, no. 3-4, pp. 523–540, 1999. [Online]. Available: http://gateway.webofknowledge.com/gateway/Gateway.cgi?GWVersion=2&SrcAuth=mekentosj&SrcApp=Papers&DestLinkType=FullRecord&DestApp=WOS&KeyUT=000082694000002 (cit. on p. 6).

[GSB+01] E Gadioli, G. F. Steyn, C Birattari, M Cavinato, S. H. Connell, A. A. Cowley, E Fabrici, S. V. Förtsch, E. G. Erba, J. J. Lawrie, F. M. Nortier, J. P. F. Sellschop, and E. S. Haddad, "Emission of 8Begs in the interaction of 12C with nuclei at incident energies up to 33 MeV/amu", English, *The European Physical Journal A - Hadrons and Nuclei*, vol. 11, no. 2, pp. 161–173, Jul. 2001.

DOI: 10.1007/s100500170082. [Online]. Available: http://link.springer.com/article/10.1007/s100500170082 (cit. on p. 19).

[GCEHS53] L. H. Gray, A. D. Conger, M. Ebert, S. Hornsey, and O. C. A. Scott, "The concentration of oxygen dissolved in tissues at the time of irradiation as a factor in radiotherapy", *The British Journal of Radiology*, vol. 26, no. 312, pp. 638–648, 1953, PMID: 13106296. DOI: 10.1259/0007-1285-26-312-638. eprint: http://dx.doi.org/10.1259/0007-1285-26-312-638. [Online]. Available: http://dx.doi.org/10.1259/0007-1285-26-312-638 (cit. on p. 3).

[PDG] P. D. Group, *Passage of particles through matter*. European Physics Journal C, 1998. DOI: 10.1016/S0066-4103(10)70005-3. [Online]. Available: http://scholar.google.com/scholar?q=related:kEO4ZEUh9lgJ:scholar.google.com/&hl=en&num=20&as_sdt=0,5 (cit. on p. 4).

[Hae06] E. Haettner, PhD thesis, KTMvStockholm, 2006 (cit. on p. 5).

[HIS06] E Haettner, H Iwase, and D Schardt, "Experimental fragmentation studies with 12C therapy beams.", English, *Radiation Protection Dosimetry*, vol. 122, no. 1-4, pp. 485–487, 2006. DOI: 10.1093/rpd/ncl402. [Online]. Available: http://rpd.oxfordjournals.org/cgi/doi/10.1093/rpd/ncl402 (cit. on p. 6).

[Har02] L. B. Harrison, "Impact of Tumor Hypoxia and Anemia on Radiation Therapy Outcomes", English, vol. 7, no. 6, pp. 492–508, Dec. 2002. DOI: 10.1634/theoncologist.7-6-492. [Online]. Available: http://theoncologist.alphamedpress.org/cgi/doi/10.1634/theoncologist.7-6-492 (cit. on p. 3).

[Cna] *Http://www.cnao.it*, 2014. [Online]. Available: http://www.cnao.it (cit. on p. 1).

[Ptc] *Http://www.ptcog.ch*, 2014. [Online]. Available: http://www.ptcog.ch (cit. on pp. 1, 2).

[IAEA] IAEA, "Relative Biological Effectiveness in Ion Beam Therapy", pp. 1–165, Jul. 2014 (cit. on p. 3).

[Jac62] J. D. Jackson, *Classical electrodynamics*. Wiley, 1962 (cit. on p. 65).

[JR75] F. James and M. Roos, "Minuit: A System for Function Minimization and Analysis of the Parameter Errors and Correlations", *Comput. Phys. Commun.*, vol. 10, pp. 343–367, 1975. DOI: 10.1016/0010-4655(75)90039-9 (cit. on p. 20).

[Jer14] M. Jermann, "Particle therapy statistics in 2013", *International Journal of Particle Therapy*, vol. 1, no. 1, pp. 40–43, 2014. DOI: 10.14338/IJPT.14-editorial-2.1. [Online]. Available: http://dx.doi.org/10.14338/IJPT.14-editorial-2.1 (cit. on p. 2).

[Jip84] P. Jipsen, "Eloss, a program for calculating the ranges of ions in matter", National Accelerator Center, 1984 (cit. on p. 20).

[Kar75] P. J. Karol, "Nucleus-nucleus reaction cross sections at high energies: Soft-spheres model", English, *Phys.Rev.*, vol. C11, no. 4, pp. 1203–1209, 1975. DOI: 10.1103/PhysRevC.11.1203. [Online]. Available: http://link.aps.org/doi/10.1103/PhysRevC.11.1203 (cit. on p. 12).

[Kie08] J. Kiefer, "The physical basis for the biological action of heavy ions", English, *New Journal of Physics*, vol. 10, no. 7, p. 075 004, Jul. 2008. DOI: 10.1088/1367-2630/10/7/075004. [Online]. Available: http://iopscience.iop.org/1367-2630/10/7/075004/fulltext/ (cit. on p. 3).

[KIK11] Y Koba, H Iwamoto, and K Kiyohara, "Scintillation Efficiency of Inorganic Scintillators for Intermediate-Energy Charged Particles", *Progress in NUCLEAR ...*, 2011. [Online]. Available: http://www.aesj.or.jp/publication/pnst001/data/218.pdf (cit. on p. 28).

[Kra00] G Kraft, "Tumor therapy with heavy charged particles", English, *Progress in Particle and Nuclear Physics*, vol. 45, S473–S544, 2000. DOI: 10.1016/S0146-6410(00)00112-5. [Online]. Available: http://linkinghub.elsevier.com/retrieve/pii/S0146641000001125 (cit. on p. 3).

[LMG79] D. A. Landis, N. W. Madden, and F. S. Goulding, "Energy-dependent losses in pulsed-feedback preamplifiers", *Nuclear Science, IEEE Transactions on*, vol. 26, no. 1, pp. 428–432, 1979, ISSN: 0018-9499. DOI: 10.1109/TNS.1979.4329670 (cit. on p. 46).

[Las51a] N. O. Lassen, "The total charges of fission fragments in gaseous and solid stopping media", *Mat. Fys. Medd. Dan. Vid. Selsk.*, vol. 26, no. 5, pp. 1–28, 1951 (cit. on p. 4).

[Las51b] ——, "Total charges of fission fragments as functions of the pressure in the stopping gas", *Mat. Fys. Medd. Dan. Vid. Selsk.*, vol. 26, no. 12, pp. 1–19, 1951 (cit. on p. 4).

[Mai08] A. Mairani, "Nucleus-nucleus interaction modelling and applications in ion therapy treatment planning", *Scientifica Acta*, vol. 1, no. 1, p. 129, Mar. 2008. [Online]. Available: http://riviste.paviauniversitypress.it/index.php/sa/article/view/265 (cit. on p. 6).

[MMRBM93] K Michaelian, A Menchaca-Rocha, and E Belmont-Moreno, "Calibration of scintillation detectors using a specific luminescence model", English, *Nuclear Instruments and Methods in Physics Research Section A: Accelerators, Spectrometers, Detectors and Associated Equipment*, vol. 334, no. 2-3, pp. 457–460, Oct. 1993. DOI: 10.1016/0168-9002(93)90808-U. [Online]. Available: http://linkinghub.elsevier.com/retrieve/pii/016890029390808U (cit. on p. 21).

[Mir11] J. Mira, "The role played by quasi-elastic and inelastic break-up of the 12c and 16o projectiles in the the role played by quasi-elastic and inelastic break-up of the 12c and 16o projectiles in the production of intermediate mass fragments at 14-35 mev/u", PhD thesis, University of Stellenbosch, 2011 (cit. on p. 19).

[MMM+13] S Molinelli, A Mairani, A Mirandola, G Vilches Freixas, T Tessonnier, S Giordanengo, K Parodi, M Ciocca, and R Orecchia, "Dosimetric accuracy assessment of a treatment plan verification system for scanned proton beam radiotherapy: one-year experimental results and Monte Carlo analysis of the involved uncertainties", English, *Physics in Medicine and Biology*, vol. 58, no. 11, pp. 3837–3847, May 2013. DOI: 10.1088/0031-9155/58/11/3837. [Online]. Available: http://stacks.iop.org/0031-9155/58/i=11/a=3837?key=crossref.bcb7d6d706a08547338115de2defe809 (cit. on p. 7).

[PJPSE08] H. Paganetti, H. Jiang, K. Parodi, R. Slopsema, and M. Engelsman, "Clinical implementation of full Monte Carlo dose calculation in proton beam therapy", English, *Physics in Medicine and Biology*, vol. 53, no. 17, pp. 4825–4853, Aug. 2008. DOI: 10.1088/0031-9155/53/17/023. [Online]. Available: http://stacks.iop.org/0031-9155/53/i=17/a=023?key=crossref.46ea32862d53e9e7a3f4585991039f33 (cit. on p. 7).

[PMB+12] K Parodi, A Mairani, S Brons, B. G. Hasch, F Sommerer, J Naumann, O Jäkel, T Haberer, and J Debus, "Monte Carlo simulations to support start-up and treatment planning of scanned proton and carbon ion therapy at a synchrotron-based facility", English, vol. 57, no. 12, pp. 3759–3784, May 2012. DOI: 10.1088/0031-9155/57/12/3759. [Online]. Available: http://stacks.iop.org/0031-9155/57/i=12/a=3759?key=crossref.dc749c062fbbf26f8ec50421c3173478 (cit. on p. 7).

[Par11] K. Parodi, "**MONTE CARLO METHODS FOR DOSE CALCULATIONS**", in *Biological and Medical Physics, Biomedical Engineering*, U. Linz, Ed., Berlin, Heidelberg: Springer Berlin Heidelberg, Sep. 2011, pp. 97–116, ISBN: 978-3-642-21413-4. DOI: 10.1007/978-3-642-21414-1. [Online]. Available: http://link.springer.com/10.1007/978-3-642-21414-1 (cit. on p. 7).

[PBE+08] K. Parodi, T. Bortfeld, W. Enghardt, F. Fiedler, A. Knopf, H. Paganetti, J. Pawelke, G. Shakirin, and H. Shih, "PET imaging for treatment verification of ion therapy: Implementation and experience at GSI Darmstadt and MGH Boston", English, *Nuclear Instruments and Methods in Physics Research Section A: Accelerators, Spectrometers, Detectors and Associated Equipment*, vol. 591, no. 1, pp. 282–286, Jun. 2008. DOI: 10.1016/j.nima.2008.03.075. [Online]. Available: http://linkinghub.elsevier.com/retrieve/pii/S0168900208004580 (cit. on p. 8).

[PDG98] Particle Data Group, "Passage of particles through matter: in Review of Particle Physics (RPP 1998)", *Eur.Phys.J.*, vol. C3, pp. 144–151, 1998. [Online]. Available: http://pdg.lbl.gov/1998/contents_large_sports.html (cit. on pp. 44, 45).

[PIK84] W. V. Prestwich, M. A. Islam, and T. J. Kennett, "Primary E2 transitions observed following neutron capture for the mass region 144<A<180", English, vol. 315, no. 1, pp. 103–111, Feb. 1984. DOI: 10.1007/BF01436215. [Online]. Available: http://link.springer.com/10.1007/BF01436215 (cit. on p. 67).

[Pro14] N. D. E. Project, *Http://www.tunl.duke.edu/nucldata/index.shtml*, 2014. [Online]. Available: http://www.tunl.duke.edu/nucldata/index.shtml (cit. on p. 38).

[RER00] S. Roesler, R. Engel, and J. Ranft, "The Monte Carlo Event Generator DPMJET-III", *arXiv.org*, Dec. 2000. arXiv: hep-ph/0012252 [hep-ph]. [Online]. Available: http://arxiv.org/abs/hep-ph/0012252v1 (cit. on p. 8).

[Rog06] D. W. O. Rogers, "Fifty years of Monte Carlo simulations for medical physics", English, *Physics in Medicine and Biology*, vol. 51, no. 13, R287–R301, Jun. 2006. DOI: 10.1088/0031-9155/51/13/R17. [Online]. Available: http://stacks.iop.org/0031-9155/51/i=13/a=R17?key=crossref.1e38c9fad92a4b29f5cdbc122689551a (cit. on p. 7).

[RNB91] J. L. Romero, G. A. Needham, and F. P. Brady, "The response of NaI (T1) to 30− 60 MeV Z= 1 particles", English, *Nuclear Instruments and ...*, vol. 301, no. 2, pp. 241–245, 1991. DOI: 10.1016/0168-9002(91)90465-3. [Online]. Available: http://linkinghub.elsevier.com/retrieve/pii/0168900291904653 (cit. on pp. 28, 29).

[Ser47] R Serber, "The Production of High Energy Neutrons by Stripping", English, *Phys.Rev.*, vol. 72, no. 11, pp. 1008–1016, 1947. DOI: 10.1103/PhysRev.72.1008. [Online]. Available: http://link.aps.org/doi/10.1103/PhysRev.72.1008 (cit. on p. 5).

[SHV62] T. Sikkeland, E. Haines, and V. Viola, "Momentum Transfer in Heavy-Ion-Induced Fission", English, *Phys.Rev.*, vol. 125, no. 4, pp. 1350–1357, Feb. 1962. DOI: 10.1103/PhysRev.125.1350. [Online]. Available: http://link.aps.org/doi/10.1103/PhysRev.125.1350 (cit. on p. 5).

[SWVPSW79] K Siwek-Wilczynska, E. H. d. M. van Voorthuysen, J van Popta, R. H. Siemssen, and J Wilczynski, "Incomplete fusion in 12C+160Gd collisions", English, *Nuclear Physics A*, vol. 330, no. 1, pp. 150–172, Oct. 1979. DOI: 10.1016/0375-9474(79)90542-6. [Online]. Available: http://linkinghub.elsevier.com/retrieve/pii/0375947479905426 (cit. on p. 5).

[SPF+06] F. Sommerer, K. Parodi, A. Ferrari, K. Poljanc, W. Enghardt, and H. Aiginger, "Investigating the accuracy of the FLUKA code for transport of therapeutic ion beams in matter", English, *Physics in Medicine and Biology*, vol. 51, no. 17, pp. 4385–4398, Sep. 2006. DOI: 10.1088/0031-9155/51/17/017. [Online]. Available: http://stacks.iop.org/0031-9155/51/i=17/a=017?key=crossref.80f674ebcf75f637e4b1ee9817f4646c (cit. on p. 8).

[SFL+05] G. F. Steyn, S. V. Förtsch, J. J. Lawrie, R Bassini, E Gadioli, C Birattari, and S. H. Connell, "Detection of single and resonant projectile fragments in 12C-induced reactions to the continuum", English, vol. 538, no. 1-3, pp. 559–573, Feb. 2005. DOI: 10.1016/j.nima.2004.08.112. [Online]. Available: http://linkinghub.elsevier.com/retrieve/pii/S0168900204020108 (cit. on pp. 21, 28, 29).

[Icr] "Stopping Powers and Ranges for Protons and Alpha Particles", English, *ICRU*, vol. 49, no. 1, pp. 15–19, May 1993 (cit. on p. 4).

[VGTC67] J. P. Vautrin, J Graff, J. M. Thirion, and G Chouraqui, "Discrimination de particules d'energie inferieure a 10 MeV par generateur de fonction associe a un telescope< i> ΔE</i>,< i> E</i>", English, *Nuclear Instruments and ...*, vol. 55, pp. 358–364, 1967. DOI: 10.1016/0029-554X(67)90142-5. [Online]. Available: http://linkinghub.elsevier.com/retrieve/pii/0029554X67901425 (cit. on p. 44).

[Wil46] R. R. Wilson, "Radiological use of fast protons", *Radiology*, vol. 47, pp. 487–491, 1946 (cit. on p. 1).

[YMN12] S. Yonai, N. Matsufuji, and M. Namba, "Calculation of out-of-field dose distribution in carbon-ion radiotherapy by Monte Carlo simulation", English, *Medical Physics*, vol. 39, no. 8, p. 5028, 2012. DOI: 10.1118/1.4736823. [Online]. Available: http://scitation.aip.org/content/aapm/journal/medphys/39/8/10.1118/1.4736823 (cit. on p. 8).

Acronyms

FLUKA FLUktuierende KAskade or Fluctuating Cascade. 8

BME Boltzmann Master Equation. 9, 12–14

CNAO Centro Nazionale di Adroterapia Oncologica. 1

DNA Deoxyribonucleic acid. 2–4

DPM Dual Parton Model. 8

DPMJET Dual Parton Model and Jets. 8, 9

GDH Geometry Dependent Hybrid Model. 11

GINC Generalised Intra-Nuclear Cascade. 9

HIT Heidelberg Ion Beam Therapy Center. 1, 7

LET Linear Energy Transfer. 3, 5

MC Monte Carlo simulation. i–iii, 7, 8, 20, 21, 23–25, 29, 31, 35, 38–40, 46–48, 50–52, 54, 71, 72, 81, 83, 99–103

NIST National Institute of Standards and Technology. 39, 43, 101

PEANUT Pre-Equilibrium Approach to NUclear Thermalization. 8, 9, 11, 12, 65, 66

PET Positron Emission Tomography. 8

PTC Particle Therapy Center. 2

RBE Relative Biological Effectiveness. 3–5

RQMD Relativistic Quantum Molecular Dynamics. 9

SSD Silicon Strip Detector. 18, 19, 23–25, 27, 30, 31, 33, 35–38, 53, 71, 99, 100

List of Figures

List of Tables